Evaluation of Thai Long-Tail Boat Propeller Performance and Its Improvement

ゲオキャウ, プラチャコン

https://doi.org/10.15017/1560381

Evaluation of Thai Long-Tail Boat Propeller Performance and Its Improvement

August 2015

Prachakon Kaewkhiaw

Contents

Nomenclature

$\vec{A}$:	Surface area vector
C_P :	Pressure coefficient
$C_{p,1}$:	First hamonic amplitude of pressure coefficient
$C_{p,m}$:	Mean value of pressure coefficient
$\vec{C}_1, \vec{C}_2$:	Vector of offspring
d_1 :	Distance between $\vec{P}_1$ and $\vec{P}_2$
d_2 :	Distance between $\vec{P}_3$ and the line $\overrightarrow{P_1P_2}$
$\vec{e}_i$:	Orthogonal basis vectors
G :	Acceleration of gravity
D_ω :	Cross diffusion term
D_ω^+ :	Positive portion of the cross diffusion term
g_i :	Component of the gravitational vector in the *i* direction
G_b :	Production of turbulence kinetic energy due to buoyancy
G_k :	A manner consistent with the Boussinesq hypothesis
G_ω :	Production of ω
$\tilde{G}_k$:	Production of turbulence kinetic energy
J :	Advance coefficient
k :	Turbulence kinetic energy
K_Q :	Torque coefficient
K_T :	Thrust coefficient
n :	Propeller rotational speed per second
$N(0, \sigma^2)$:	Normal random number whose average and standard deviation is 0 and σ

n_D :	Number of design variables
Pr_t :	Turbulent Prandtl number for energy
$\vec{P}_1, \vec{P}_2, \vec{P}_3$:	Vectors of parent
Q :	Propeller torque
Re_K :	Reynolds number by Kempf
$\vec{r}_0$:	Position vector
S :	Strain rate magnitude
$S_\emptyset$:	Source of $\emptyset$ per unit volume
T :	Propeller thrust
T_{ij} :	Stress tensor
μ :	Dynamic viscosity
μ_{eff} :	Effective viscosity
μ_t :	Turbulence viscosity
$\vec{u}_\gamma$:	Velocity of the moving frame relative to the inertial reference frame
$\overrightarrow{V}$:	Velocity vector
V_A :	The velocity of uniform flow
$\vec{v}$:	Absolute velocity
v_L :	Kinematic viscosity of water
$\vec{v}_t$:	Translational frame velocity
$\vec{v}_\gamma$:	Relative velocity
y_v:	Viscous sub-layer thickness
Y_M :	Contribution of the fluctuating dilatation
y^+ :	Non-dimensional wall distance

Y_k :	Dissipation of k
Y_ω :	Dissipation of ω
z_i:	Normal random number used in UNDX
α, β :	Constants to determine standard deviations σ_1 and σ_2 in UNDX
ρ :	Density of water
θ :	Blade angle position
$\emptyset_1$:	Cosine phase angle, corresponding to the angle of maximum pressure
β :	The coefficient of thermal expansion
Ψ :	Propeller shaft inclination
$\emptyset$:	Scalar quantity
ε :	Dissipation rate of turbulent kinetic energy
ω :	Specific dissipation rate of turbulent kinetic energy
$\overrightarrow{\omega}$:	Angular velocity
γ :	Effective exchange coefficient
η_o :	Propeller efficiency
σ_k :	Turbulent Prandtl number of turbulent kinetic energy
σ_ε :	Turbulent Prandtl number of dissipation rate of turbulent kinetic energy
σ_ω :	Turbulent Prandtl numbers of specific dissipation rate
σ_1, σ_2:	Standard deviations
$\Gamma_\emptyset$:	Diffusion coefficient for $\emptyset$
$\nabla_\emptyset$:	Dradiant of $\emptyset$
Γ_k :	Effective diffusivity of k

Γ_ω : Effective diffusivity of ω

x_i, x_j : Coordinate components

u_i, u_j : Velocity component

$\overline{u_i' u_j'}$: Reynolds stress

δ_{ij} : Kronecker delta

ε_{ijk} : Alternating tensor

Chapter 1
Introduction

1.1 Background

Long-Tail Boats have been used in many areas of southeast asia countries especially in Thailand. It is a type of watercraft native in Thailand. In this study, Long-Tail Boat in the Chao Phraya River in Bangkok is only focused to study. The Chao Phraya River is a main river in Thailand. Long-Tail Boat has known as Ruea Hang Yao in the Thai language. It is classified in genus high speed vessel because operating velocity is much high. Fig. 1.1 shows a photograph of Long-Tail Boat used to investigate in this study.

Long-Tail Boats are often used to transport passengers and tourists. It is designed to contain approximately 8-15 passengers depending on size of boat. In south areas of Thailand, it is employed to sightseeing boats in coastal area. Moreover, it is applied to small fishing boats. There are also competitions involving Long-Tail boat in some provinces of Thailand.

Fig. 1.1 Long-Tail Boat in Thailand

The principal particulars of Long-Tail Boat adopted in this study are shown in Table 1.1. Fig. 1.2 shows hull shape of Long-Tail Boat, which is made from local hardwood. The bottom is designed into flat as shown in Fig. 1.3. The hull of Long-Tail Boat has a step at the bottom in the middle of longitudinal direction as shown in Fig. 1.4. The objective of step is to reduce wetted surface area which influences to resistance. The aft part is flat which has been raised perpendicular to the front part. The front part is more slender curve. The fore part immerses lower than aft part. The draft is approximately 27 cm in aft.

Fig. 1.5 shows a typical photograph of engine of Long-Tail Boat. Long-Tail Boat uses ordinary automotive engine as easily available and maintainable. This engine is unalterably mounted on boat stern. Long driveshaft is connected to the engine and the shaft can rotate through semicircle in order to move. Actually, propeller is installed directly to the tip of shaft which is covered by hollow metal rod without gearbox as shown in Fig. 1.6. One of the reasons for without reduction gear is that the engine speed is low. The actual inclined shaft angle of Long-Tail Boat is operated about 12° from horizontal axis. The shaft length is 4.5 m. The inclined shaft propeller seems suitable for Long-Tail Boat because it has shallow water draft.

Table 1.1 Principal particulars of Long-Tail Boat

L_{OA} (m)	8.88
L_{WL} (m)	4.98
Max.Breadth (m)	1.60
Max.Depth (m)	0.72
Max.Draft (m)	0.27

Fig. 1.2 Overview of Long-Tail Boat

Fig. 1.3 Bottom of Long-Tail Boat

Fig. 1.4 Step at bottom of Long-Tail Boat

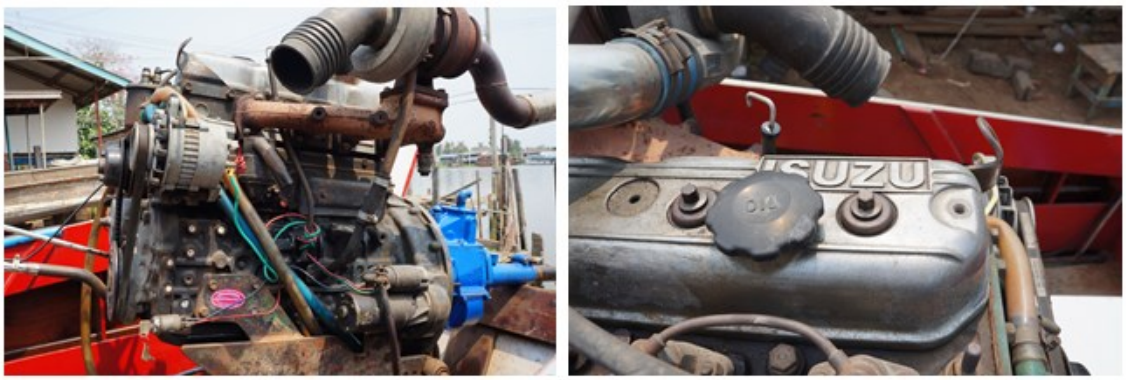

Fig. 1.5 Engine of Long-Tail Boat

Fig. 1.6 Engine, shaft and propeller of Long-Tail Boat

The first Long-Tail Boat was discovered in middle area of Thailand in Sing Buri province. It was established by Sanong Thitibura who worked in position as helmsman of Royal since 1932. The first boat was created by using cost about 150 Bath in that time. The boat specifications were length and breadth of 5 and 1.2 meters respectively. The first model has evolved from a rowing boat with an engine mounted. The engine was machined to long shaft and the ending installed two blades propeller then this is one of his wisdom. After that time, Long-Tail Boats have been created and developed using mounted engine by Sucheep Ratsarn, Chanchai Phairatkhun, Sukhum Chirawanit and Samai Kittikhun in 1933, 1939, 1941 and 1950 respectively [1].

The National Research Council of Thailand has announced the award to people who have been mentioned upward as the inventor of Long Tail Boat in 1984. Although, they have not been known yet in previous time but each person has an idea of himself. The principle is similar such as using engines with boats for increasing speed thus this is particularly useful for transportation.

The information of Marine Department, Ministry of Transport [2], Thailand demonstrated the amounts of Long Tail Boats (Inland waterway) in Thailand as shown in Table 1.2. It is found that the boat is being increased every year. If focusing only Long-Tail Boat in Chao Phraya River in Bangkok approximately 300 vessels are in present.

Table 1.2 Amount of Long-Tail Boat in Thailand

Year	2008	2009	2010	2011	2012	2013
No. of Boats	3,459	3,821	4,083	4,311	4,424	4,578

The history of Long-Tail Boat propeller is not found clearly: it is even unknown who designed or developed in the first time. Moreover, the persons mentioned above probably did not investigate whether the propeller has been used suitably to engines or not. Actually, propeller of Long-Tail Boat was developed by owner at each areas using local wisdom. It was tested in water way or river after manufacturing.

For the reasons, the evaluation of propeller performances and improvement for increasing efficiency by using numerical methods are very effective, and are carried out in this study.

1.2 Literature Review

This section reviews the related study of work on straight shaft propeller, inclined shaft propeller and propeller optimization. The brief summary of the major experiment and computation work including numerical method for optimized blade shape are illustrated. The scope of predicting propeller performances such as propeller thrust, torque and efficiency including pressure distribution on the blade for straight shaft and inclined shaft conditions are also discussed for computation and experiment.

1.2.1 Experimental and Numerical Study of Propeller Performance

(1) Straight Shaft Condition

The measurement of propeller performances for open-water have been carried out in many previous experiments by using Laser Doppler Velocimetry (LDV) and Particle Image Velocimetry (PIV) such as Boswell [3], who designed cavitation performance and open-water performance of a series of research skewed propeller. Ukon et al. [4-6] measured the pressure distribution of a conventional and highly skewed propeller model under non-cavitating condition. After that they measured pressure distribution in full scale for conventional and highly skewed propeller respectively. Stella et al. [7] measured the axial velocity component of a propeller wake. Chesnaks and Jessup [8] investigated the tip vortex flow by using LDV. Calcangno et al. [9] investigated the complicated 3D flow behind a marine propeller in the transverse and longitudinal planes by using a stereoscopic PIV technique. Lee et al. [10] compared the flow structures of the same marine propeller for the conditions of open free surface and closed surface flows at the rather low Reynolds number. Bertetta et al. [11] carried out experiment to measure thrust, torque and cavitation for different propeller working points of unconventional CLT (Contracted and Loaded Tip) propeller by using LDV.

The panel methods have long been applied for the analysis of propeller problems such as Hess and Valarezo [12] made the first attempt to analyze steady flow around a marine propeller by using 3D boundary element method. Kerwin et al. [13] applied the panel method to investigate the marine propeller performance. Ando et al. [14] predicted steady performances for marine propeller by using a simple surface panel method.

Recently, The computer performances have been improved therefore RANS method are becoming the practical tool to solve the propeller problems such as Abdel-Maksoud et al. [15] investigated viscous flow simulation for conventional and high skew marine propeller. Chen and Stern [16] evaluated computational fluid dynamics of four quadrant marine proposer flow. Watanabe et al. [17] examined simulation of steady and unsteady cavitation on a marine propeller using a RANS. Rhee and Joshi [18] estimated computational validation for flow around marine propeller using unstructured mesh based Navier-Stokes. Kawamura et al. [19] investigated simulation of unsteady cavitating flow around marine propeller by using a RANS CFD code. Morgut and Nobile [20] evaluated comparison of Hexa-Structured and Hybrid-Unstructured meshing approaches for numerical prediction of the flow around marine propeller. Kaewkhiaw et al. [21] studied application of turbulence modeling for cavitation simulation on marine propeller by using CFD. Bertetta et al. [22] analyzed the potential panel method and an RANS analysis of an unconventional CLT propeller. Baek et al. [23] investigated effects of the advance ratio on the evolution of propeller wake.

(2) Inclined Shaft Condition

Many high speed propellers are mounted on inclined shaft and the propeller is operating at incidence to the inflow as shown in Fig. 1.7 [24]. Two flow components indicated at the propeller plane are $V_a cos\psi$ and $V_a sin\psi$ where ψ is the propeller shaft inclination to the horizontal axis. The component of flow $V_a sin\psi$ perpendicular to the propeller shaft gives rise to an eccentricity of the propeller thrust. On one side, as the propeller blade is upward going, there is a decrease in relative velocity and blade load. On the other side, the propeller blade is downward going and there is an increase in relative velocity and blade load. The net effect is to move the center of thrust off the centerline. This leads also a significant fluctuation in blade loading as the blade rotates.

The thrust T can be resolved into a horizontal thrust $Tcos\psi$ and a vertical force $Tsin\psi$ which may make a significant contribution to the balance of masses and forces in the condition of planning craft. Then, trim angle should be added to the shaft inclination when resolving for horizontal thrust.

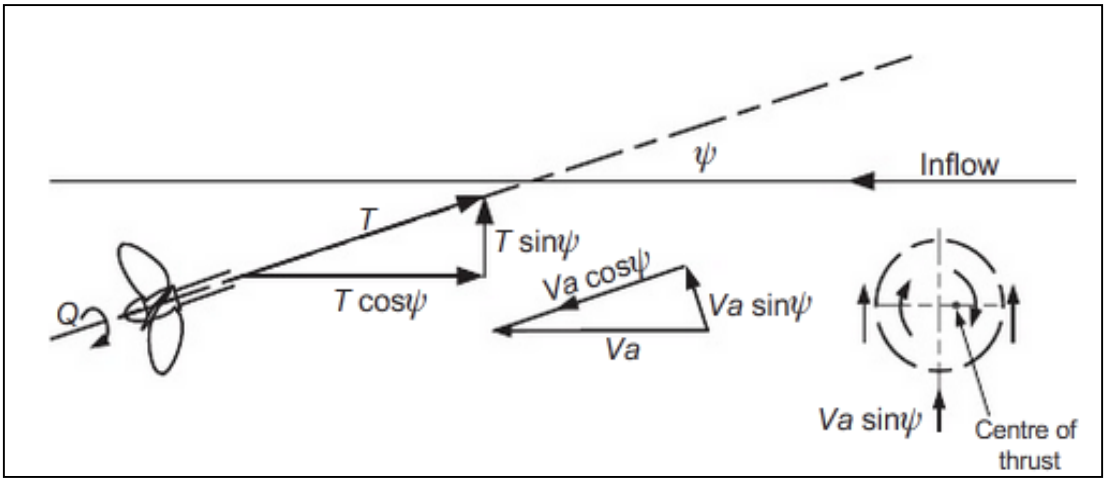

Fig. 1.7 Flow and force components with inclined shaft propeller

The forces measurements for inclined shaft propeller have been conducted more over four decades such as Taniguchi et al. [25] who observed cavitation on the supercavitating propeller in oblique flow. Boswell et al. [26,27] measured single blade load on a moderate skewed propeller (DTMB 4661) in oblique flows of 10°, 20° and 30° of which experimental data have been used for the validation of potential propeller analysis codes by many researchers. Jessup [28,29] measured unsteady blade loads for pressure distribution on two model scales propeller (DTMB 4679 and 4718). In 1990, the symmetric 3 blades model scale propeller (DTMB 4119) was tested in the 24 inch water tunnel behind harmonic wake screens with 3, 6, 9 and 12 cycles per revolution and one blade thrust and torque were measured. Both conditions were used for comparative validation of potential propeller analysis at The ITTC propeller workshop in 1998 and the results were summarized in ITTC in 1998 [30]. Ukon et al. [31] measured pressure distribution on full scale propeller for Seiun-Maru HSP behind ship wake. Raestad [32] measured blade forces at Marine Laboratory, Kristinehamn, Sweden for DNV included measurements of one blade thrust, torque, transverse force, bending moment and spindle moment on 4 blades low skewed propeller operating in oblique flow of 10° and behind wake screens providing V-shape axial wakes.

Numerical methods are applied to analysis of unsteady by many researchers such as Kerwin and Lee [33] who predicted steady and unsteady marine propeller performance by numerical lifting surface theory. Liu and Bose [34] implemented inflow

wake and hyperboloid panel algorithm to deal with the oblique flow for highly skewed propellers. Hoshino [35] analyzed propeller performance in unsteady flow by using a surface panel method. Hsin [36] and Gaggero et al. [37] solved the unsteady cavitating flow by a potential boundary element method. Politis [38] applied the boundary element method to predict unsteady trailing vortex sheets emanating from each blade. However, the panel methods mentioned above are limited in inviscid flow only but viscous flow are important for realization such as tip vortex and hub vortex predictions, the panel methods are unable to predict them in high accuracy.

Some researchers have solved unsteady propeller blade forces in oblique flows by using RANS methods such as Krasilnikov et al. [39] who analyzed unsteady propeller blade forces by RANS. Gaggero et.al [37] simulated unsteady flow propeller with oblique flow by using RANS. Schroeder and Dai [40-41] solved marine propeller problem in a cross flow using RANS. Simultaneously, they proposed the numerical calculation of propeller performance for thrust and torque coefficients for straight shaft in steady condition and applied to unsteady flows using inclined shaft propeller arrangement with inclined flow angles of 4.8° and 8.8° for N4990 propeller model and compared the experimental data of Naval Surface Warfare Center Carderock Division, (NSWCCD). Dubbioso et al. [42] proposed CFD analysis of propeller performance in oblique flow and the propeller loading has been analyzed at different incidence angles 10° to 30° for oblique flow using E779A propeller model. Kaewkhiaw and Ando [43] simulated unsteady propeller performance with inclined shaft propeller arrangement by using CFD. They predicted thrust and torque loads in oblique flow for N4990 propeller. In addition, they predicted fully unsteady force on propeller blade for mean pressure, first harmonic amplitude and first harmonic phase angle of P4679 propeller with inclined shaft angle 7.5°.

1.2.2 Blade Shape Optimization to Improve Propeller Performance

As for the method of propeller design, the traditional method by using the propeller design chart obtained from the systematic model experiments is still common. Lifting-surface method and panel method are also used for propeller design in a trial and error manner.

Moreover, propeller design methods by using optimizing techniques have been presented. Dai, et al. [44] optimized the chord length and blade thickness distribution in order to minimize the propeller mass under the constraint of constant propeller efficiency. Mishima and Kinnas [45] optimized the camber, pitch and chord distribution under the constraint of a constant mean torque or constraint mean power subject to a given maximum allowed cavity area or a maximum cavity volume in non-uniform flow. Jang et al. [46] optimized the pitch distribution in order to maximize the propeller efficiency. Takekoshi et al. [47] studied the design of propeller blade sections by using optimization algorithm the SQP (Sequential Quadratic Programming) method.

Recently, propeller design methods by using genetic algorithm have been presented. Karim et al. [48] offered a micro genetic algorithm based optimization technique for the design marine propeller. Ando et al. [49] proposed a method to improve propeller performance by using real-coded genetic algorithm.

1.3 Purpose

The Improving propulsive efficiency is a perpetual goal for naval architects and engineers. It is good established helping for reduction of the CO_2 emissions which impacted to environment. Therefore, propeller performances have great influence on propulsive performances of the boat. Then, propeller improvement is significant for energy saving in vessel.

The propulsion systems of Long-Tail Boat propeller have never been studied with theoretical methods. Therefore, the evaluation of propeller performance of standard propeller of Long-Tail Boat in Thailand by model test and optimization of propeller blade shapes are considered to the objective of this study. By this objective, the following works are done.

- CFD analysis system to evaluate the propeller performance in straight and inclined shaft conditions is built.
- Model test of the standard propeller of Long-Tail Boat in Thailand is conducted in straight shaft condition and the accuracy of the present CFD analysis system is confirmed.
- Blade shapes of the Long-Tail Boat propeller are optimized in straight shaft condition and the model test of improved propeller is conducted. The propeller performances of original and improved propellers in experiments are compared with each other.
- The performances of original and improved propellers in inclined shaft condition are evaluated by the present CFD analysis system.

1.4 Outline

This paper is divided into five chapters.

Chapter 1, “Introduction”, the background, literature reviews, purpose and outline are presented.

Chapter 2, “CFD Analysis for Propeller Performance in Straight and Inclined Shaft Conditions”, Introduction of RANS for computational methods are defined in this simulation such as governing equation, conservation of mass and momentum equation, turbulence modeling, fluid flow modeling and discretization. After that, description of simulation propeller performance with straight shaft and inclined shaft are presented using N4990 and P4679 propeller including grid independence and computational domain are explained. Lastly, the calculated results comparing with the measured data for verification of numerical method are presented.

Chapter 3, “Characteristics of Long-Tail Boat Propeller”, the Long-Tail Boat propeller is introduced in full scale and model scale. The measured data of propeller performance for thrust, torque coefficient and propeller efficiency are presented. The experiments are carried out in uniform inflow by using the high speed circulating water channel at Kyushu University. The grid independence study and computational domain of simulation are explained. The numerical results compared the experimental data are analyzed.

Chapter 4, “Optimization of Long-Tail Boat Propeller”, the improved Long-Tail Boat propeller with straight shaft is clarified to optimization process. Next, the grid independence and computational domain including the calculated results of improved propeller performances comparing with measured data are described. After that, the simulations of inclined shaft for original and improved propeller are presented such as computational grid including results of calculations with compared straight shaft.

Chapter 5, “Conclusion”, the summarized results and conclusions of these studies are present.

Chapter 2
CFD Analysis for Propeller Performance in Straight and Inclined Shaft Conditions

2.1 Introduction

In this chapter, CFD analysis system for evaluation of Long-Tail Boat propeller performance is described. The present system is built based on the ANSYS Fluent 14.0 [50]. Next, validation of the present system is conducted by comparing the results with experimental data of propeller characteristics in straight and inclined shaft conditions. In addition, pressure distributions on the propeller blade surface in inclined shaft condition are compared with the experimental data and the accuracy of the present system is confirmed. Here the experimental data of not Long-Tail Boat propeller but two well-known propellers are referred.

2.2 CFD Analysis System for Propeller Performance

2.2.1 Governing Equations

The governing equations can be derived from the statements of the conservation of mass, momentum and energy for the flows which involve heat transfer or flow compressibility but incompressible flow in the ANSYS Fluent 14.0 is solved with conservation equations only for mass and momentum.

The flow is simulated with enforcing the conservation of mass and momentum. The conservation equations are commonly known as Navier-Stokes equations. It was used in their incompressible form and the general Reynolds Averaged Navier-Stokes (RANS) equations can be written in Cartesian tensor form as follows:

$$\frac{\partial \rho}{\partial t} + \frac{\partial (\rho u_i)}{\partial x_i} = 0 \tag{2.1}$$

and the momentum equations form as follows:

$$\frac{\partial (\rho u_i)}{\partial t} + \frac{\partial (\rho u_i u_j)}{\partial x_j} = -\frac{\partial p}{\partial x_i} + \frac{\partial}{\partial x_j}\left[\mu\left(\frac{\partial u_i}{\partial x_j} + \frac{\partial u_j}{\partial x_i} - \frac{2}{3}\delta_{ij}\frac{\partial u_l}{\partial x_l}\right)\right] + \frac{\partial}{\partial x_j}\left(-\rho\overline{u_i' u_j'}\right) \tag{2.2}$$

Where δ_{ij} is the Kronecker delta $\left(\delta_{ij} = 1 \; if \; i = j \; and \; \delta_{ij} = 0 \; if \; i \neq j\right)$ and $-\rho\overline{u_i' u_j'}$ are the unknown Reynolds stresses that have to be modeled to close the momentum equation.

RANS modeling can be classified into two groups: Eddy-Viscosity Models (EVMs) and Reynolds-Stress models (RSMs). EVMs are based on the Boussinesq hypothesis where the Reynolds stresses are proportional to the rates of strain form as follows:

$$-\rho\overline{u_i' u_j'} = \mu_t\left(\frac{\partial u_i}{\partial x_j} + \frac{\partial u_j}{\partial x_i}\right) - \frac{2}{3}\rho k \delta_{ij} \tag{2.3}$$

Where μ_t is the eddy viscosity, k is the kinetic energy of the turbulence and δ_{ij} is the Kronecker delta.

2.2.2 Turbulence Model

The SST (Shear Stress Transport) k-ω turbulence model is only used in this study. The SST k-ω turbulence model is employed to calculate Reynolds-Stress term in the RANS equations. The k-ω model is converted from k-ε model [51]. The k is turbulence kinetic energy, ε is dissipation rate of turbulent kinetic energy and ω is specific dissipation rate of turbulent kinetic energy. The details of the standard k-ε and k-ω models are described in Appendix A.

The SST k-ω model was developed by Menter [52] to effectively blend the robust and accurate formulation of the k-ω model in the near wall region with the free stream independence of the k-ε model [51] in the far field. To achieve the k-ε model is converted into k-ω formulation.

The SST k-ω model is similar to the standard k-ω model [53] but includes the following refinements:

- The standard *k-ω* model and the transformed *k-ε* model are both multiplied by a blending function and both models are added together. The blending function is designed to be one in the near wall region which activates the standard *k-ω* model and zero away from the surface which activates the transformed *k-ε* model.
- The SST model incorporates a damped cross diffusion derivative term in the *ω* equation.
- The definition of the turbulent viscosity is modified to account for the transport of the turbulent shear stress.
- The modeling constants are different.

These features make the SST *k-ω* model more accurate and reliable for a wider class of flows such as adverse pressure gradient flows, airfoils, transonic shock waves than the standard *k-ω* model [52]. The SST *k-ω* equations are written as follows:

$$\frac{\partial}{\partial t}(\rho k) + \frac{\partial}{\partial x_i}(\rho k u_i) = \frac{\partial}{\partial x_j}\left(\Gamma_k \frac{\partial k}{\partial x_j}\right) + \tilde{G}_k - Y_k \tag{2.4}$$

$$\frac{\partial}{\partial t}(\rho \omega) + \frac{\partial}{\partial x_j}\left(\rho \omega u_j\right) = \frac{\partial}{\partial x_j}\left(\Gamma_\omega \frac{\partial \omega}{\partial x_j}\right) + G_\omega - Y_\omega + D_\omega \tag{2.5}$$

Where $\tilde{G}_k$ is the production term of turbulence kinetic energy due to mean velocity gradients, G_ω is that of ω, Γ_k and Γ_w are the effective diffusivity of k and ω respectively. Y_k and Y_ω are the dissipation term of k and ω due to turbulence, D_ω is the cross diffusion term.

The effective diffusivities for the SST *k-ω* model are given as follows:

$$\Gamma_k = \mu + \frac{\mu_t}{\sigma_k} \tag{2.6}$$

$$\Gamma_\omega = \mu + \frac{\mu_t}{\sigma_\omega} \tag{2.7}$$

Where μ is molecular viscosity. The σ_k and σ_ω are the turbulent Prandtl numbers for k and ω respectively. The σ_k, σ_ω and μ_t are computed as follows:

$$\sigma_k = \frac{1}{\frac{F_1}{\sigma_{k,1}} + \frac{1-F_1}{\sigma_{k,2}}} \tag{2.8}$$

$$\sigma_\omega = \frac{1}{\frac{F_1}{\sigma_{\omega,1}} + \frac{1-F_1}{\sigma_{\omega,2}}} \tag{2.9}$$

$$\mu_t = \frac{\rho k}{\omega} \frac{1}{max\left[\frac{1}{a^*}, \frac{SF_2}{a_1 \omega}\right]} \tag{2.10}$$

Where

$$a^* = a^*_\infty \left(\frac{a^*_0 + Re_t/R_k}{1 + Re_t/R_k}\right) \tag{2.11}$$

$$Re_t = \frac{\rho k}{\mu \omega}$$

$$R_k = 6$$

$$a^*_0 = \frac{\beta_i}{3},\ \beta_i = 0.072$$

The high-Reynolds number form of the *k*-ω model, $a^* = a^*_\infty = 1$

Where S is the strain rate magnitude, which is defined in Appendix A. The blending functions, F_1 and F_2 are given as follows:

$$F_1 = \tanh(\emptyset_1^4) \tag{2.12}$$

$$\emptyset_1 = \min\left[\max\left(\frac{\sqrt{k}}{0.09\omega y}, \frac{500\mu}{\rho \omega y^2}\right), \frac{4\rho k}{\sigma_{\omega,2} D^+_\omega y^2}\right] \tag{2.13}$$

$$D^+_\omega = \max\left[2\rho \frac{1}{\sigma_{\omega,2}} \frac{1}{\omega} \frac{\partial k}{\partial x_j} \frac{\partial \omega}{\partial x_j}, 10^{-10}\right] \tag{2.14}$$

$$F_2 = \tanh(\emptyset_2^2) \tag{2.15}$$

$$\emptyset_2 = \max\left[2\frac{\sqrt{k}}{0.09\omega y}, \frac{500\mu}{\rho \omega y^2}\right] \tag{2.16}$$

Where y is the distance to the first node from the nearest solid surface and D^+_ω is the positive portion of the cross diffusion term.

The term $\tilde{G}_k$ represents the production of turbulence kinetic energy which is defined as:

$$\tilde{G}_k = \min(G_k, 10\rho\beta^* z\omega) \tag{2.17}$$

Where G_k is defined in the same manner as in the standard *k-ω* model which is shown in Appendix A.

$$\beta^* = \beta_i^*[1 + \zeta^* F(M_t)] \tag{2.18}$$

$$\beta_i^* = \beta_\infty^* \left[\frac{\frac{4}{15}+(Re_t/R_\beta)^4}{1+(Re_t/R_\beta)^4}\right] \tag{2.19}$$

$$\zeta^* = 1.5$$

$$R_\beta = 8$$

$$\beta_\infty^* = 0.09$$

$z = 0.41$

$F(M_t)$ is defined in Appendix A.

The term G_ω represents the production of ω and is given by

$$G_\omega = \frac{a}{v_t}\tilde{G}_k \tag{2.20}$$

Where the coefficient, $a \approx 1$ is applied for the high-Reynolds number.

The introduction of a cross-diffusion term is defined as follows:

$$D_\omega = 1(1 - F_1)\rho \frac{1}{\omega\sigma_{\omega,2}} \frac{\partial k}{\partial x_j} \frac{\partial \omega}{\partial x_j} \tag{2.21}$$

The Y_k and Y_ω are defined in Appendix A.

And the model constants are given as follows:

$\sigma_{k,1} = 1.176, \sigma_{k,2} = 1, \sigma_{\omega,1} = 2, \sigma_{\omega,2} = 1.168, a_1 = 0.31.$

More information can be found in the ANSYS Fluent 14.0 Theory Guide [50].

The turbulences modeling have been verified involving the best suitable turbulence model for solving propeller performances problem [54]. It is found that SST *k-ω* turbulence model is shown the best accuracy when compared with the other turbulence model.

2.2.3 Numerical Method

(1) Discretization

This study has employed pressure-based solver which belongs to a general class of methods called the projection method. In the projection method, constraint of mass conservation (continuity) of the velocity field is achieved by solving a pressure equation. The pressure equation is derived from the continuity and the momentum equations in such a way that the velocity field is corrected by the pressure and satisfies the continuity.

Fluent uses a control volume based technique to convert a general scalar transport equation to an algebraic equation that can be solved numerically. This control volume technique consists of integrating the transport equation about each control volume, yielding a discrete equation that expresses the conservation law on a control volume basis.

Discretization of the governing equations can be illustrated most easily by considering the unsteady conservation equation for transport of a scalar quantity, $\emptyset$. This is demonstrated by the following equation written in integral form for an arbitrary control volume V as follows:

$$\int_V \frac{\partial \rho \emptyset}{\partial t} dV + \oint \rho \emptyset \vec{v} \cdot d\vec{A} = \oint \Gamma_\emptyset \nabla_\emptyset \cdot d\vec{A} + \int_V S_\emptyset dV \qquad (2.22)$$

Where

$\rho =$ Density

$\vec{v} =$ Velocity vector

$\vec{A} =$ Surface area vector

$\Gamma_\emptyset =$ Diffusion coefficient for $\emptyset$

$\nabla_\emptyset =$ Gradiant of $\emptyset$

$S_\emptyset =$ Source of $\emptyset$ per unit volume

The pressure-based solver is performed with pressure-velocity coupling. The pressure-velocity coupling is achieved through the SIMPLE algorithm [55]. The SIMPLE algorithms use a relationship between velocity and pressure corrections to enforce mass conservation and to obtain the pressure field. The discretized equations are solved by using pointwise Gauss-Seidel iterations.

(2) Computational Domain and Meshing

(a) Straight Shaft Condition

The periodic boundary condition can be applied in the case of straight shaft with uniform inflows, only one blade passage is contained to computational domains which are convenient for calculations. Moreover, it saves time in calculation. Fig. 2.1 shows computational domains used in this study.

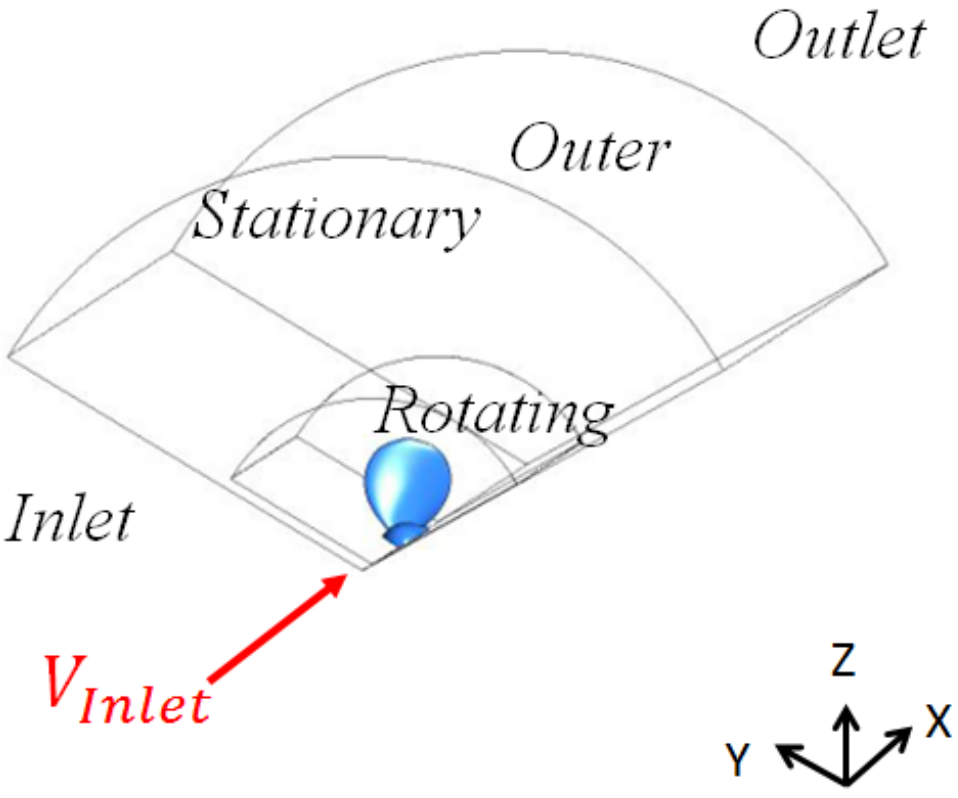

Fig. 2.1 Computational domain of periodic boundary condition

The propeller rotation is simulated by using the multiple reference frame approaches and the computational domains are subdivided into two regions: the first, a fixed region called “Stationary” where the governing equations are solved in a fixed frame and the second, a rotating region called “Rotating” where the governing equations are solved in a rotating frame [50].

The numerical simulations are carried out by using Fluent. The boundary conditions are applied: inlet boundary is set into the free stream velocity components. Outlet boundary is set into a fixed value static pressure. The rotational periodicity is assumed on the periodic boundaries. The no slip boundary condition is applied on solid surfaces (blade and hub) and the slip condition is imposed on outer boundary

The RANS equations with the shear stress transport SST k-ω turbulence model are solved in this study to simulate the propeller performance. The advantages of this model are seen in its ability to cope simultaneously with low Reynolds number in near wall and high Reynolds number in far field zones. Furthermore, it can predict more accurately for non-equilibrium regions in boundary layers with adverse pressure gradients such as separation regions [56]. The turbulence intensity and turbulence viscosity are imposed 3 % at the domain inlet.

The grids are generated by automated mesh technique with unstructured cells which have a high flexibility to fit the complex geometry of the propeller. The surface mesh beside blade and hub are discretized by hybrid-unstructured control volume mesh. The blade and hub surfaces are meshed in fineness mesh with small triangles. Meshes for the other surfaces are bigger than those for blade and hub.

Grids are generated independently one from each other. They are generated with the GAMBIT and the ANSYS ICEM CFD. The boundary prism layers on surfaces are generated in the viscous layer near blade and hub. The differential domain regions are joined in Fluent by using the grid interfaces of the solver. Fig. 2.2 shows one example of computational mesh for Rotating and Stationary regions.

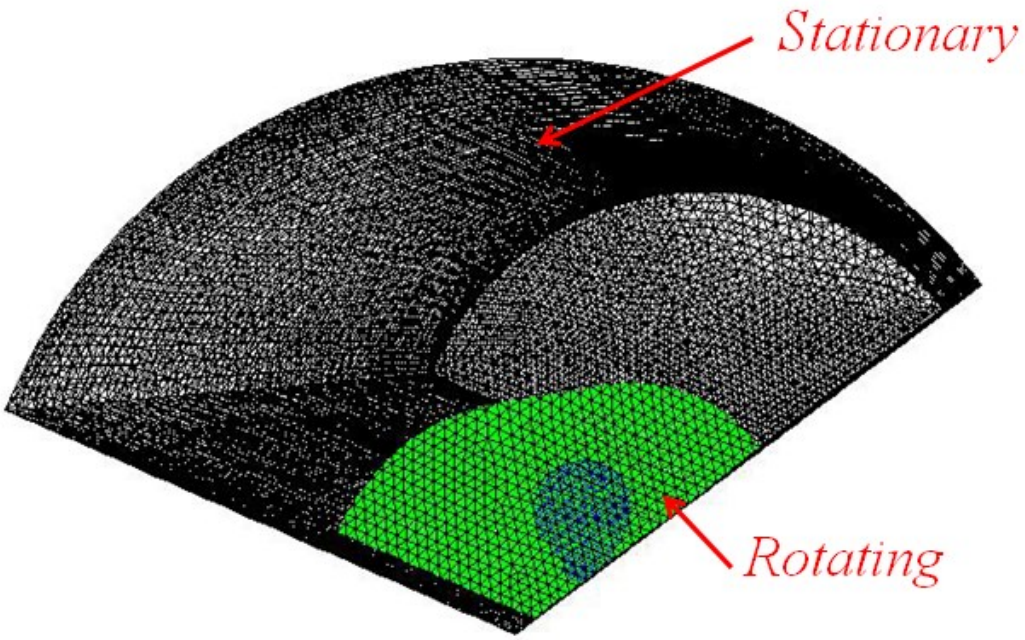

Fig. 2.2 Computational mesh for Stationary and Rotating regions

(b) Inclined Shaft Condition

The computational method performed to simulate the inclined shaft arrangement is very similar to proposed method for cross flow. Therefore, the demonstrated method can be used for any subsequent cross flow simulations. However, a single blade passage is inadequate to simulate inclined shaft arrangement or a cross flow because any non-axial flow component of velocity prescribed at the inlet of the domain will be rotated as the domain. Thus, the full blade propeller is considered for this condition.

The interface sliding mesh technique [50] is applied in this condition. It has been split into two interface zones to be created at the adjacent boundaries of the rotating mesh block which contains propeller and hub and the stationary mesh block. The interface zones are associated to form the grid interface along which the rotating mesh block will slide at the time dependent stage of solution.

In the analysis of the inclined shaft propeller are performed at two stages. At the first stage, the solution was obtained by using moving reference frame approaches for the propeller which sets blade at the vertical top position, in order to provide initial condition for time dependent calculation. At the second stage, a time accurate

simulation was carried out with sliding mesh technique with an appropriate selection of time step. The time step is determined corresponding to one degree of propeller rotation per time step and it is fixed during simulation. The small time step guarantees accurate resolution of gradients in the inflow and prevent the increase of the number of iterations need for the implicit solver to converge at each time step. The maximum number of iterations per time step is set to 20.

The analysis of the inclined shaft propellers are conducted through oblique flow condition. Boundary conditions are imposed propeller rotating while oblique flow came to it in the open water. On the inlet boundary, the velocity components of inclined flow with given inflow velocity are imposed. The inflows with inclination angles are decomposed into axial component of velocity defined as:

$$V_x = V_{in} \cos \psi \tag{2.23}$$

$$V_z = V_{in} \sin \psi \tag{2.24}$$

Static pressure is set to be constant equal zero on the outlet boundary. Fig. 2.3 shows computational domain of oblique flow.

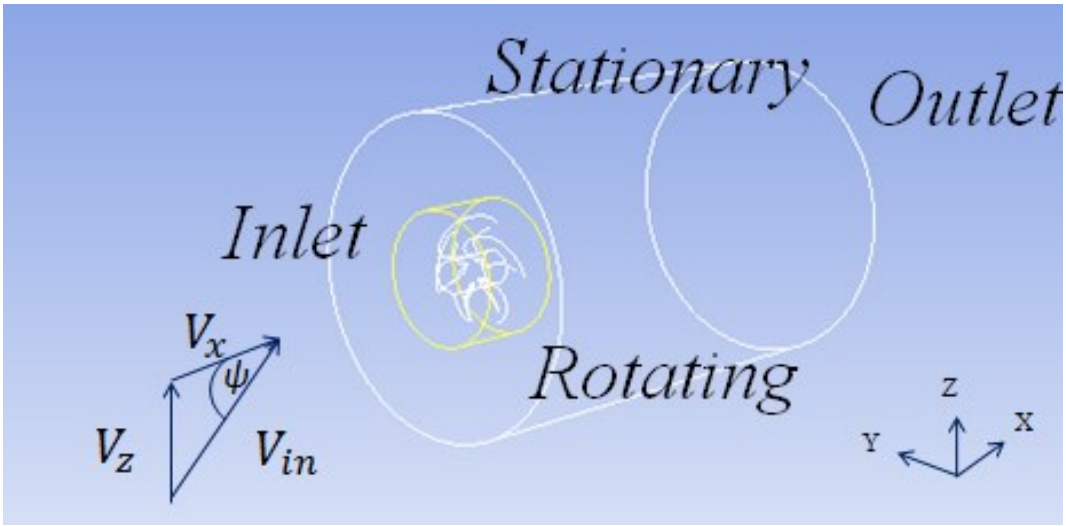

Fig. 2.3 Computational domain of oblique flow

The SST *k-ω* turbulence model is employed to calculate Reynolds stress in the RANS equations as same as the straight shaft condition. Moreover, the turbulence

intensity and turbulence viscosity at the inlet are set as same values for straight shaft calculation.

The meshing methodology in pre-processing has been adopted in this analysis by using the GAMBIT and the ANSYS ICEM CFD. It has been operated to hybrid unstructured mesh and increasing boundary layer meshes. Fig. 2.4 shows one example of computational mesh of oblique flow propeller.

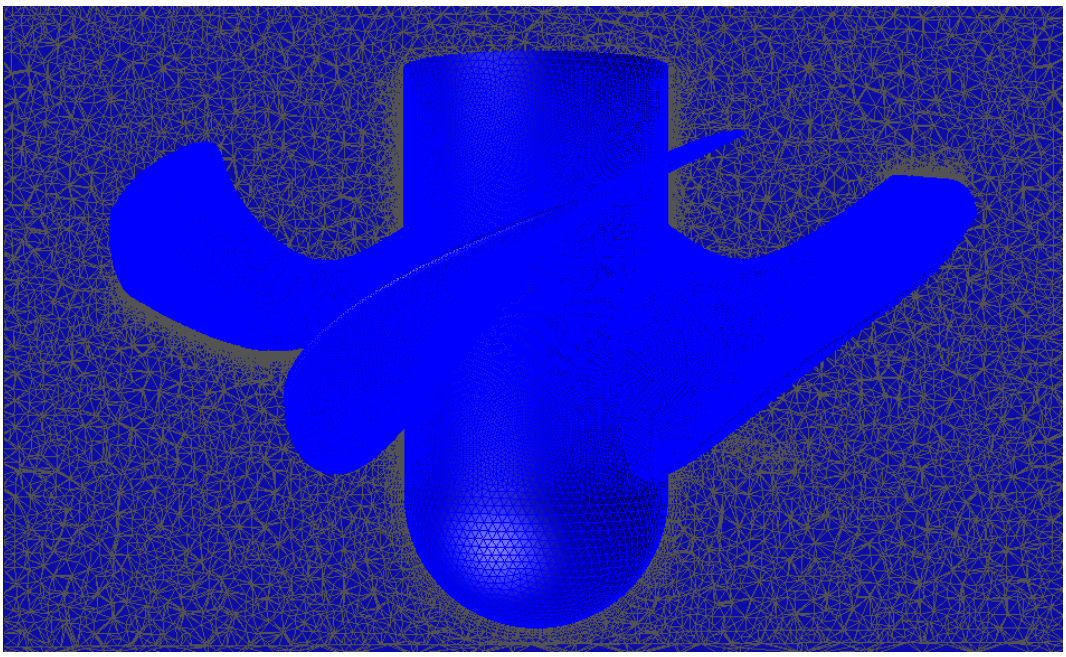

Fig. 2.4 Computational surface mesh beside blade and hub

(3) Computing Environment

In this study a personal computer with Intel(R), Core(TM), i7-3770 CPU @ 3.40 GHz and 16 GB of memory has been used. The operating system is Microsoft Windows 7, 64 bit.

2.3 Analysis of Propeller Performance

The section previously described modeling techniques of simulation propeller. The grid generation plays an important role as well as turbulence model on the accuracy of the numerical predictions. This section presents the comparison between results of simulation and experimental data. The numerical simulations for two model propellers, N4990 and P4679 were conducted. The propeller performances of simulation are predicted using different mesh quality for straight shaft and inclined shaft propeller.

The introduction of the propeller and the numerical simulations are presented first. Then, exhaustively description of computation domains and computation grids are displayed. After that, the results of the numerical simulations have been demonstrated. Finally, the concluding remarks are given.

2.3.1 Introduction of N4990 and P4679 Propellers

The N4990 model propeller is considered in this chapter. Propeller thrust, torque and efficiency with straight shaft were measured in the first step. The model was applied for inclined shaft propeller arrangement by Naval Surface Warfare Center Carderock Division (NSWCCD) [41]. The inclined shaft propellers with two inclined angles with 4.8° and 8.8° were examined. The experimental data were obtained in 36 inch water tunnel when the propeller was mounted on the inclined shaft. The principal particulars of N4990 propeller are shown in Table 2.1. Fig. 2.5 shows the CAD model which is full blade with smoothing hub of N4990.

Table 2.1 Principal particulars of N4990 propeller

Model Name	N4990
Number of Blade	5
Diameter (mm)	402.7424
Hub Ratio	0.3
Expanded Area Ratio	0.7838
Section Mean line	NACA a=0.8
Section Thickness	NACA66 (Modified)

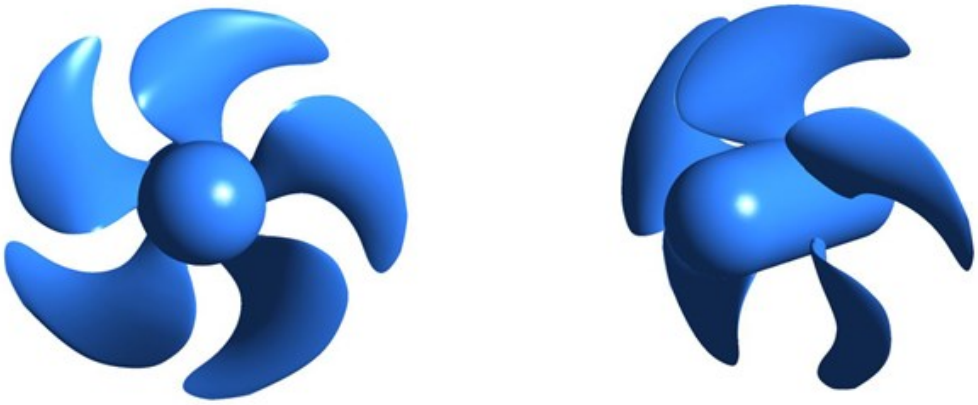

Fig. 2.5 Geometry of N4990 propeller for front view (left) and isometric view (right)

Pressure distribution on the blade surface of P4679 propeller was measured for inclined shaft angle with 7.5° in uniform inflow by Jessup [28]. The experimental data are well known in general and they were adopted as benchmark data in the 22nd ITTC propulsion committee propeller RANS/Panel method workshop [30]. The pressure measurements were performed on the pressure and suction sides at r/R=0.5, 0.7 and 0.9 respectively. The pressures were analyzed in the form of mean pressure distribution, first harmonic amplitude and first harmonic phase angle. The principal particulars of this propeller are shown in Table 2.2. Fig. 2.6 shows the CAD model which is full blade with smoothing hub of P4679.

Table 2.2 Principal particulars of P4679 propeller

Model Name	P4679
Number of Blade	3
Diameter (mm)	607
Hub Ratio	0.3
Expanded Area Ratio	0.755
Section Mean line	NACA a=0.8
Section Thickness	NACA66 (Modified)

Fig. 2.6 Geometry of P4679 propeller for front view (left) and isometric view (right)

2.3.2 Computational Domain and Meshing

The computational domains are different between straight shaft propeller with uniform inflow and inclined shaft propeller arrangement. The description can be found as below.

(1) Straight Shaft Condition

This problem considers N4990 propeller and the computational domains is defined only for one blade passage by using periodic boundary condition. The calculation domains for steady flow calculation divided into discrete control volumes by the unstructured grids which have a high flexibility to fit the complex geometry of the propeller. The blade and hub surfaces were meshed in fineness mesh with small triangles. On other surfaces, meshes were generated to be bigger than the blade and hub surfaces. The boundary prism layers on surfaces were generated in the viscous layer near on blade and hub. It created single flow passage around one blade as shown in Fig. 2.7.

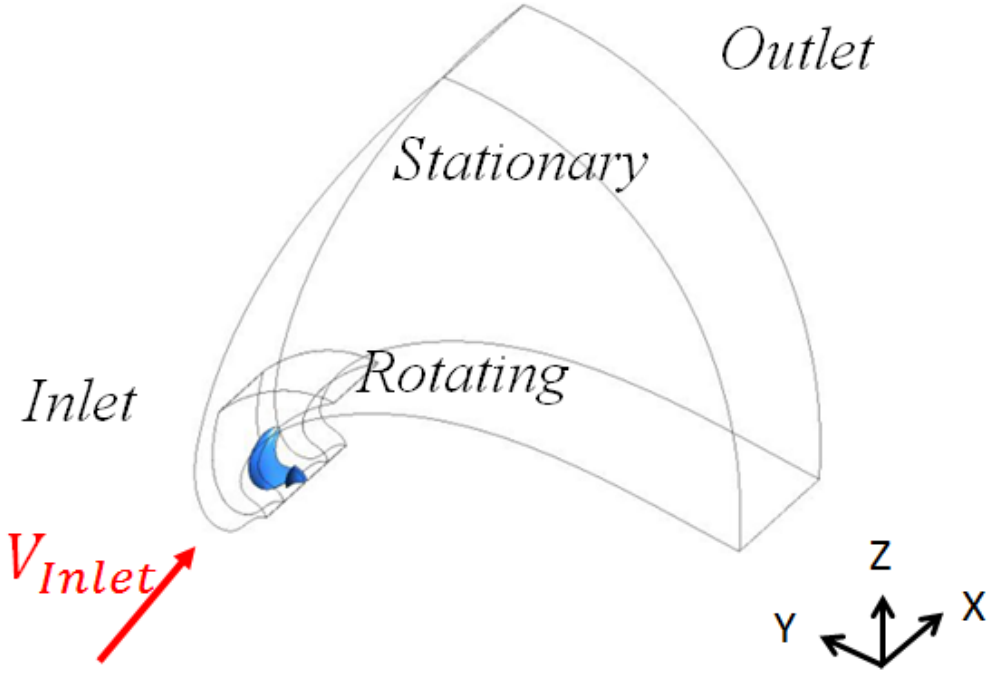

Fig. 2.7 Computational domain of periodic boundary condition

The locations of inlet and outlet boundaries are set at 10D for upstream and downstream respectively where D is the propeller diameter. The diameter of stationary domain is 6D. The diameter of rotating domain is 1.8D and it length is 10D. At the inlet, inflow velocity is imposed. At the outlet, static pressure is set to constant which is equal to zero. The rotationally periodic boundary condition with 72º between each blade of N4990 propeller is applied to calculate the flow rotating around propeller in open water.

The grid independence was studied by comparing two difference mesh, the first is "baseline mesh" which contains total mesh about 0.9 million cells. It contains in rotating domain about 0.5 million cells and in stationary domain about 0.4 million cells. The second is "refined mesh" which is applied to fineness with about 2 million cells for total mesh. Each domain was divided about 1.3 million and 0.7 million cells respectively. Fig. 2.8 shows the computational mesh around the blade and hub. The quality of surface mesh on the blade is shown in Fig. 2.9.

Fig. 2.10 shows cut plane of the prismatic layers on the blade at r/R = 0.7 where r and R are the radial position and propeller radius, respectively. The prismatic layers

were imposed about 15 layers around blade. The average values of y^+ on the solid surfaces (blade and hub) were used 30. Turbulence intensity and turbulence viscosity in this condition were used to 3%.

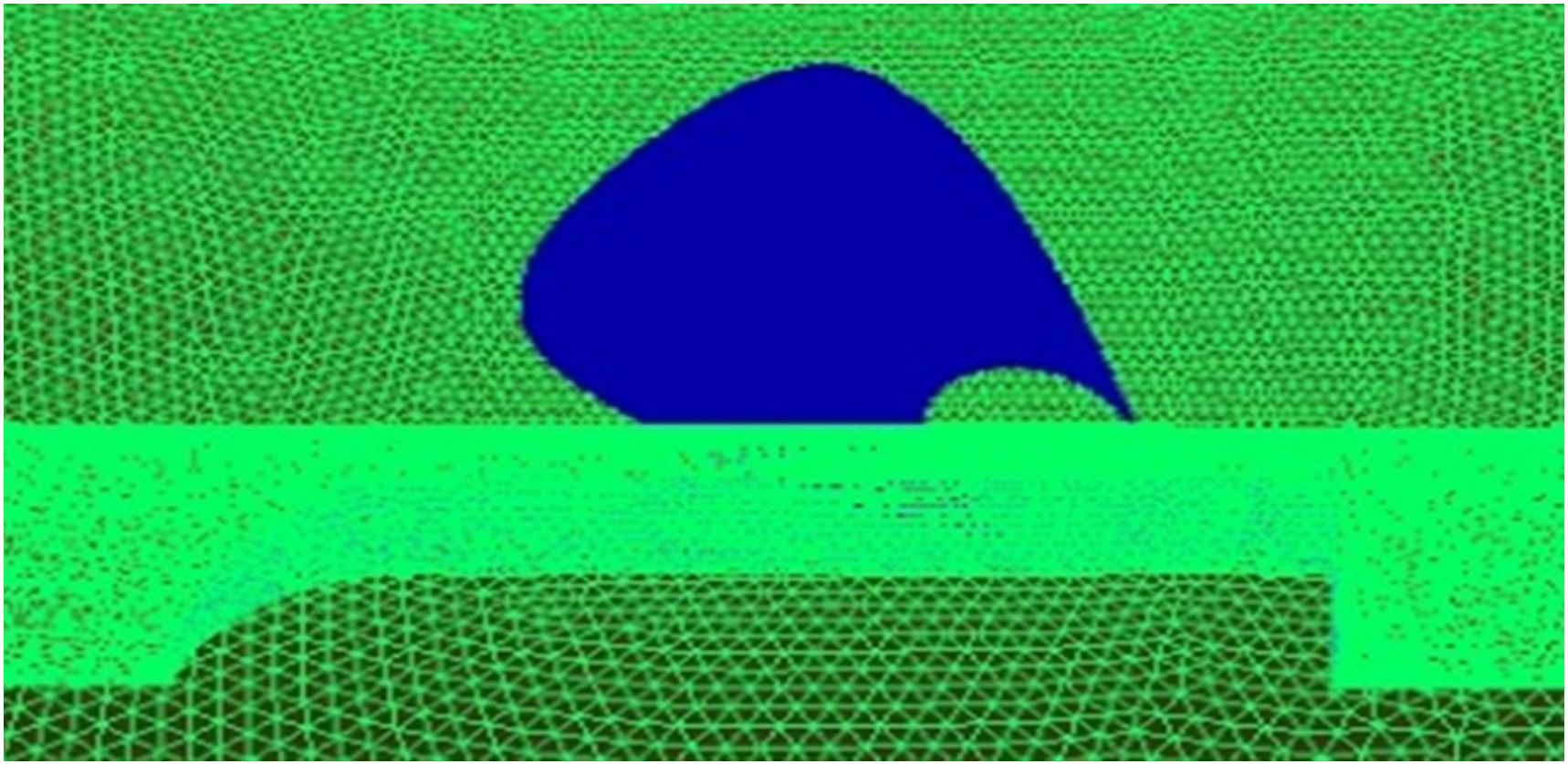

Fig. 2.8 Computational mesh around one blade and hub (refined mesh)

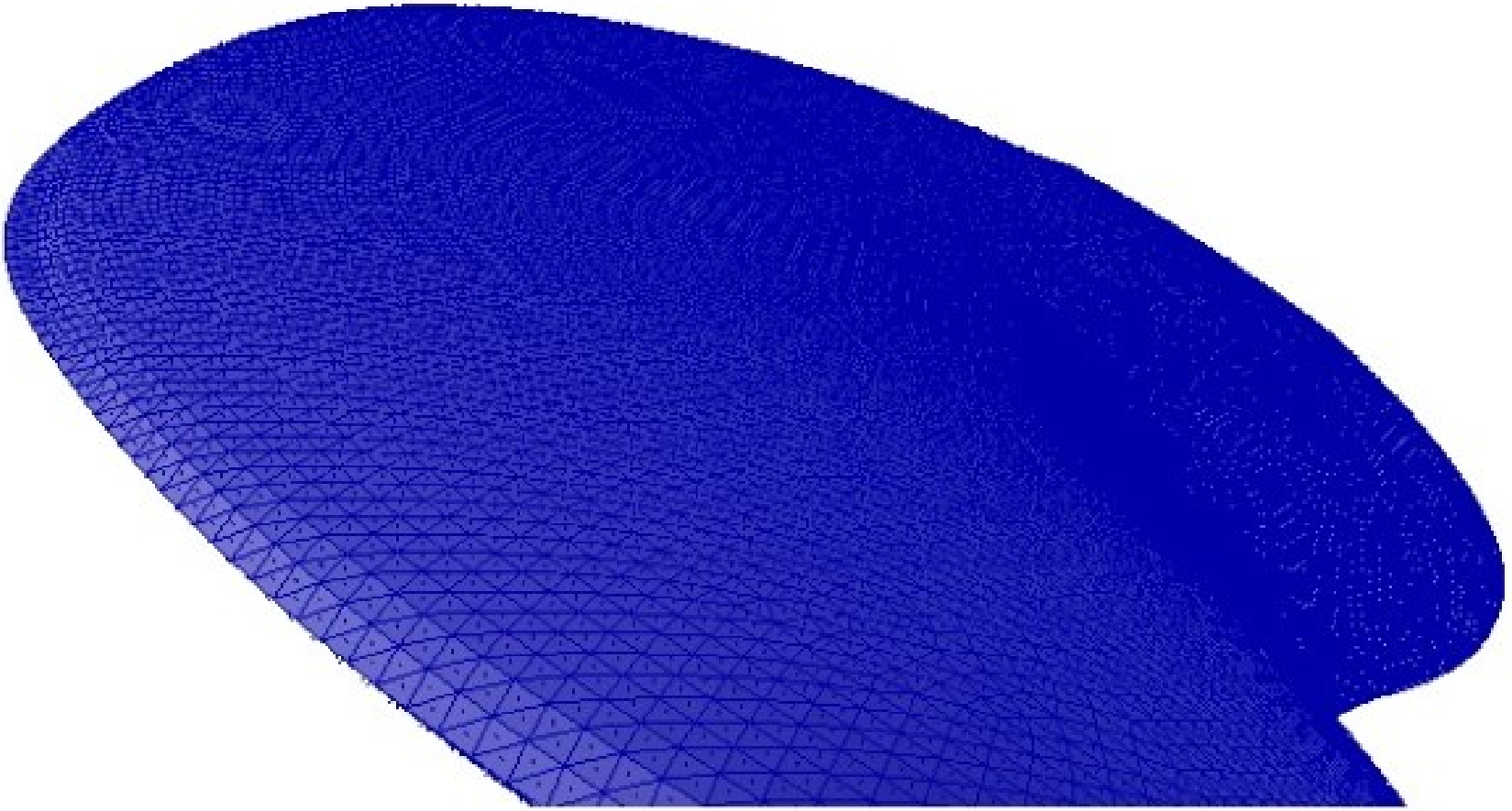

Fig. 2.9 Computational surface mesh on blade (refined mesh)

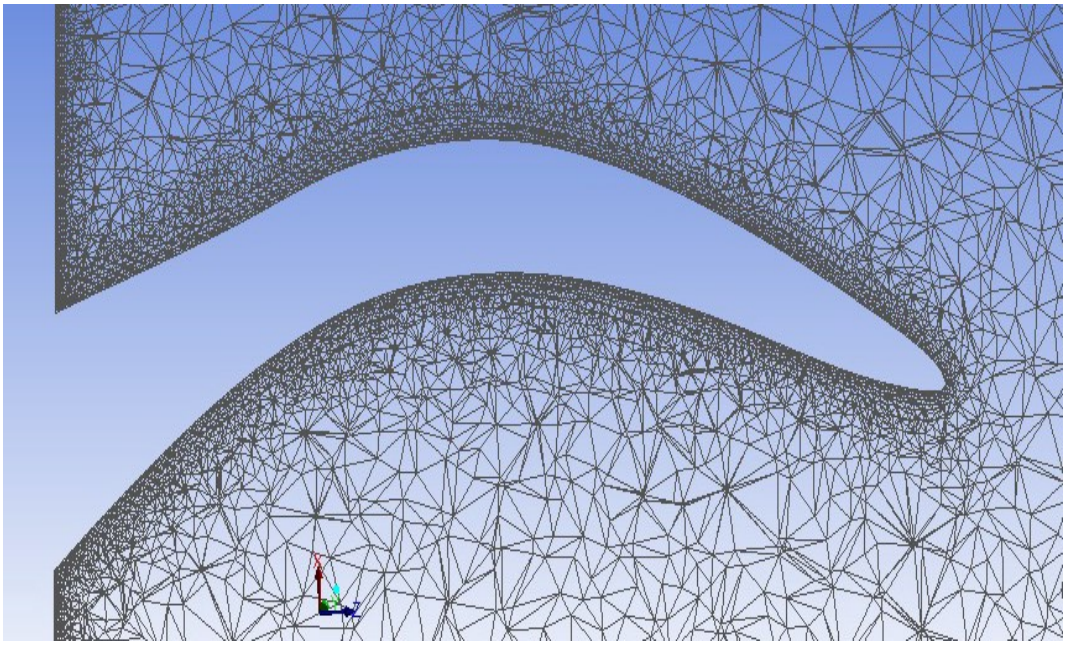

Fig. 2.10 Prismatic cells on blade at r/R=0.7 (refined mesh)

(2) Inclined Shaft Condition

The oblique flow calculations were carried out for N4990 and P4679 propellers. It was conducted by using the sliding mesh technique. The computational domains were split into fixed part called “Stationary” and rotating part called “Rotating”. The inflow with inclination angle is decomposed into velocity components defined as: $V_x = V_{in} \cos\psi$ and $V_z = V_{in} \sin\psi$ as shown in Fig. 2.11. Setting of inlet is 0.2D upstream and the exit is 4.5D downstream. The diameter of the rotating part is 1.2D, and the length is 1.5D. The diameter of the stationary part is 3D for N4990 propeller. The inlet, outlet, rotating part and stationary part were defined as 0.5D, 4.5D, 1.2D and 3D from the rotation axis of the blade for P4679 respectively.

The unstructured mesh has been applied in this condition and the domains were divided in the same way as straight shaft calculation for both propellers. The grids independence study was conducted 4 million cells for N4990 which consisted of about 3.4 million cells and about 0.6 million cells for rotating and stationary domains respectively.

For P4679 propeller was imposed total mesh about 2.6 million cells. 2 million and 0.6 million cells for rotating and stationary domains were employed respectively. Figs. 2.12 and 2.13 show mesh on the blade surface for N4990 and P4679 propellers respectively. The prismatic layers were imposed about 15 layers around blade, the average values of y^+ on the solid surfaces (blade and hub) were found after simulations to be 30. Turbulence intensity and turbulence viscosity in this condition were used to 3% for both propellers.

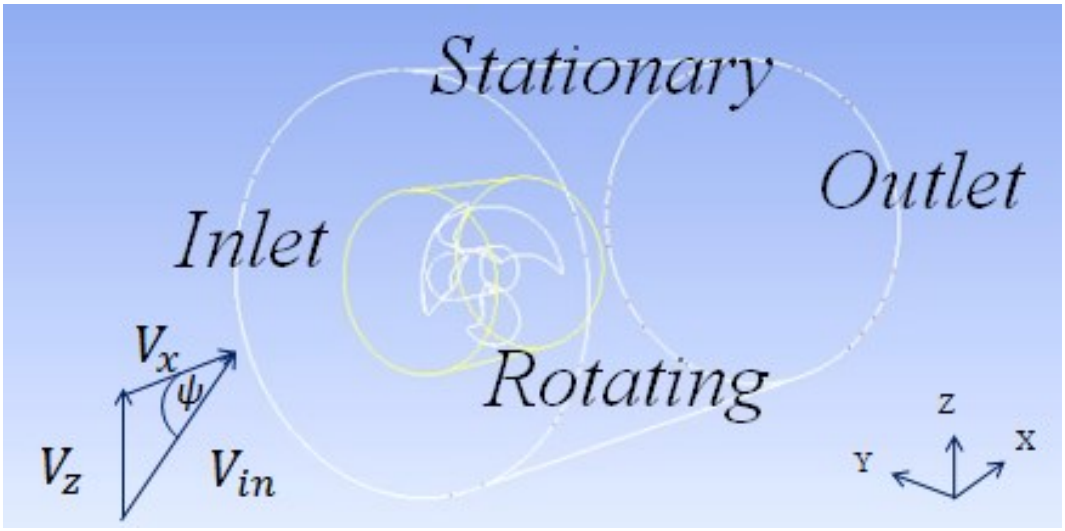

Fig. 2.11 Computational domain of oblique flow

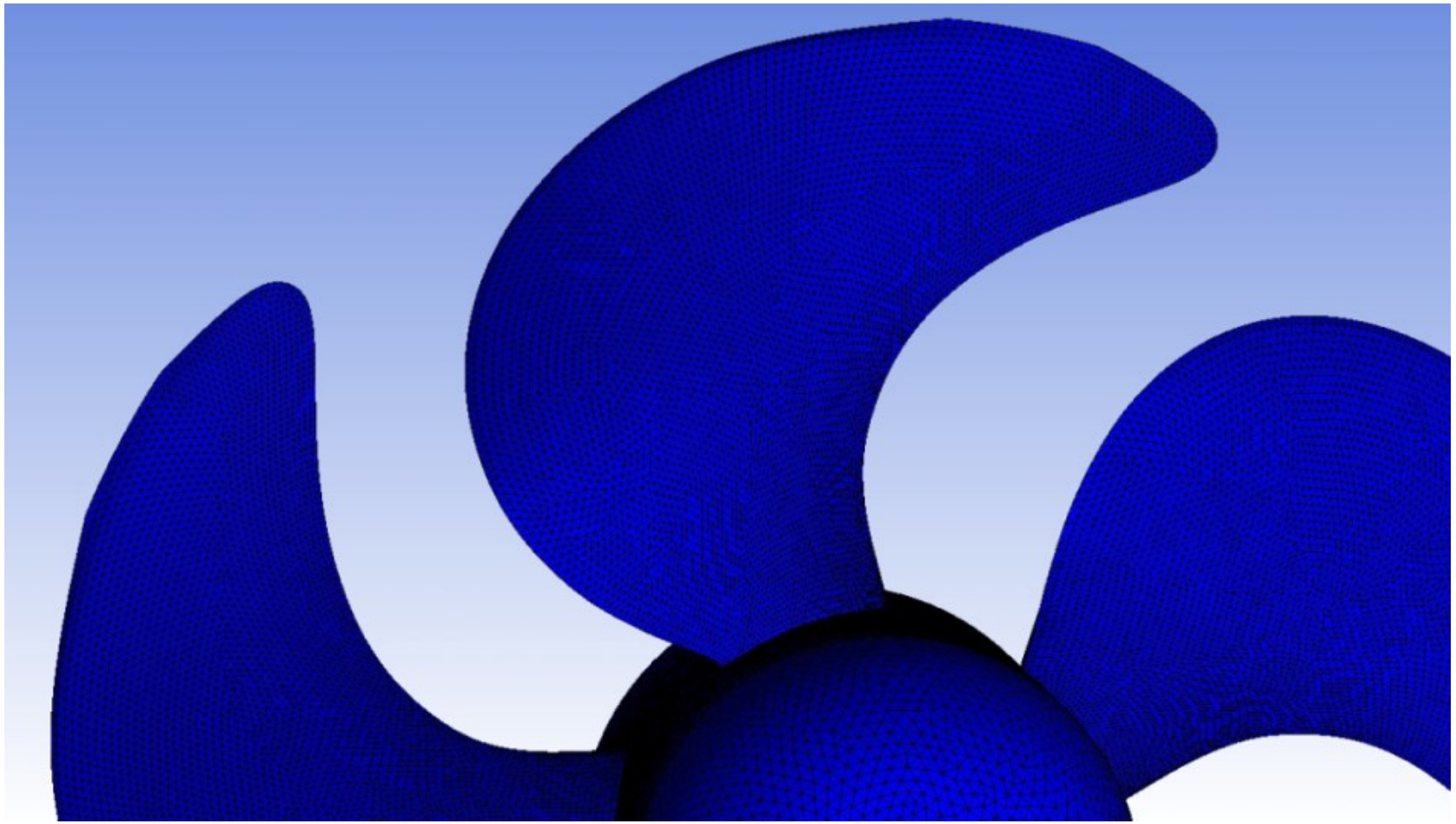

Fig. 2.12 Mesh on blade surface of N4990

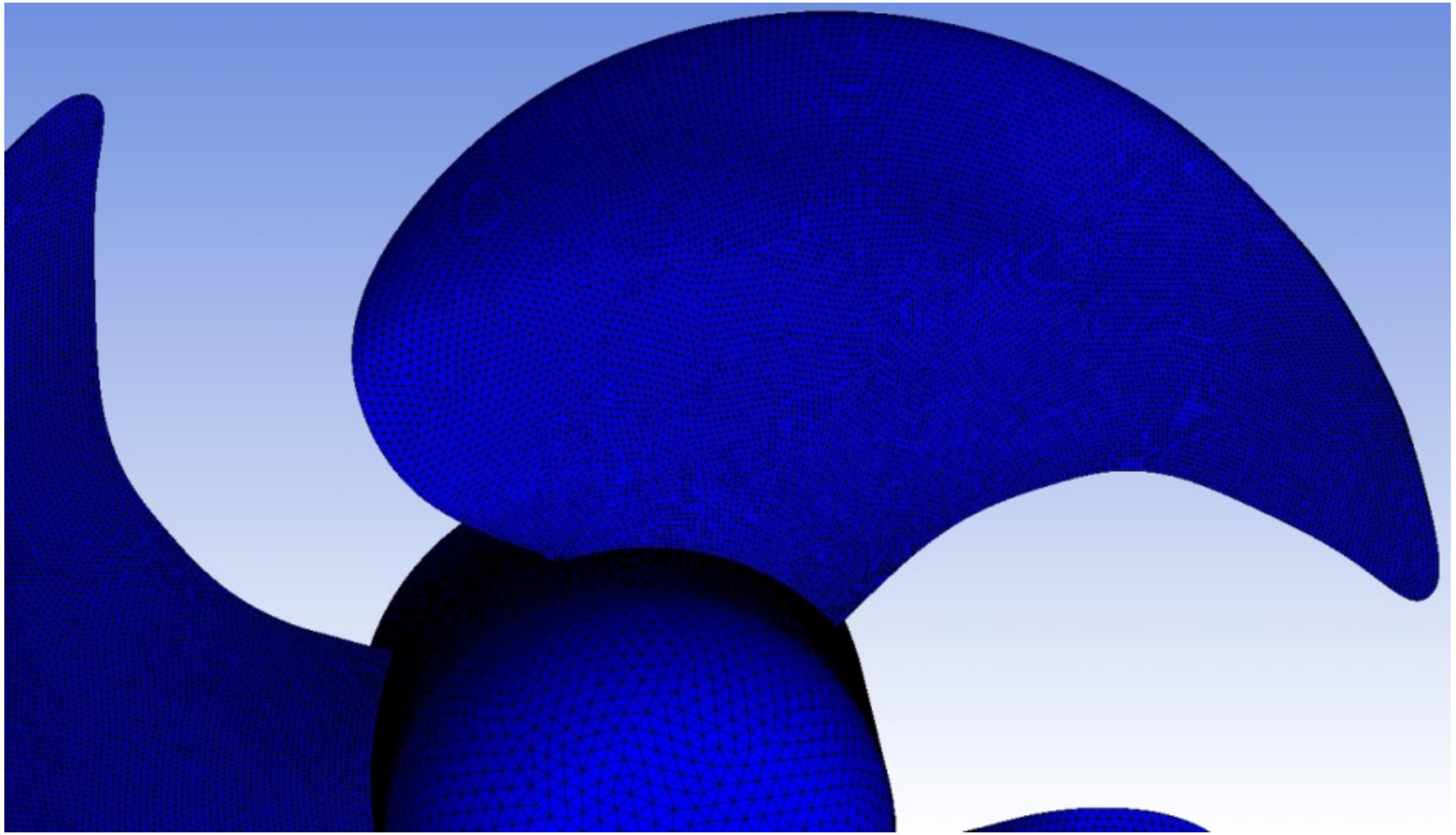

Fig. 2.13 Mesh on blade surface of P4679

2.3.3 Calculated Results

(1) Definition of Propeller Characteristics and Pressure Coefficient on Blade Surface

The present CFD has simulated steady-state flow with straight shaft and inclined flow around two model scale propellers, namely N4990 and P4679 propellers. The cavitation is not considered through this study. The propeller performances of calculation results for straight shaft and inclined shaft propeller using N4990 propeller is compared with the experimental data. The propeller performances are given in the non-dimensional forms of thrust coefficient K_T, torque coefficient K_Q and propeller efficiency η_o. They are defined as follows:

$$K_T = \frac{T}{\rho n^2 D^4} \tag{2.25}$$

$$K_Q = \frac{Q}{\rho n^2 D^5} \tag{2.26}$$

$$J = \frac{V_A}{nD} \tag{2.27}$$

$$\eta_o = \frac{J}{2\pi}\frac{K_T}{K_Q} \tag{2.28}$$

Where T is a thrust, Q is a torque, n is the propeller rotational speed per second, J is the advance coefficient, V_A is the velocity of uniform flow, ρ is the density of water, η_o is the propeller efficiency and D is the propeller diameter.

The Reynolds number defined by Kempf, Re_K at 70% radial position is defined as follow:

$$Re_{K@0.7R} = \frac{C_{0.7R}\sqrt{{V_A}^2+(2\pi n r_e)^2}}{\nu_L} \tag{2.29}$$

Where r_e is 70% of propeller radius and ν_L is the kinematic viscosity of water.

The results of calculation for fully unsteady flow with oblique inflow using P4679 propeller are compared with the experimental data of Jessup which have been summarized in the 22nd ITTC propulsion committee propeller RANS/Panel method

workshop [30]. The measurement of pressure coefficient distributions for the model propeller operating inclined flow with inclined angle of 7.5° has been conducted. The 2 loading conditions (the design advance coefficient, J=0.719 and J=1.078) are examined. The pressure measurements were performed on the pressure and suction side at r/R=0.5, 0.7 and 0.9. The pressures were analyzed in the forms of mean pressure distribution, first harmonic amplitude and first harmonic phase angle. The pressure coefficient is defined as follows:

$$C_p(\theta) = (p - p_0)/(1/2\rho {V_R}^2) \\ = C_{p,m} + C_{p,1}\, cos(\theta - \emptyset_1) \quad (2.30)$$

Where

$C_{p,m}$ = Mean value of pressure coefficient

$C_{p,1}$ = First hamonic amplitude of pressure coefficient

$\emptyset_1$ = Cosin phase angle, corresponding to the angle of maximum pressure

θ = Blade angle position

${V_R}^2 = V^2 + (2\pi nr)^2$

The directions of flow field characteristics are generated according to Fig. 2.14. Therefore the inlet axial velocity component takes negative value in flow direction, the tangential component is assumed positive counterclockwise (looking propeller suction side).

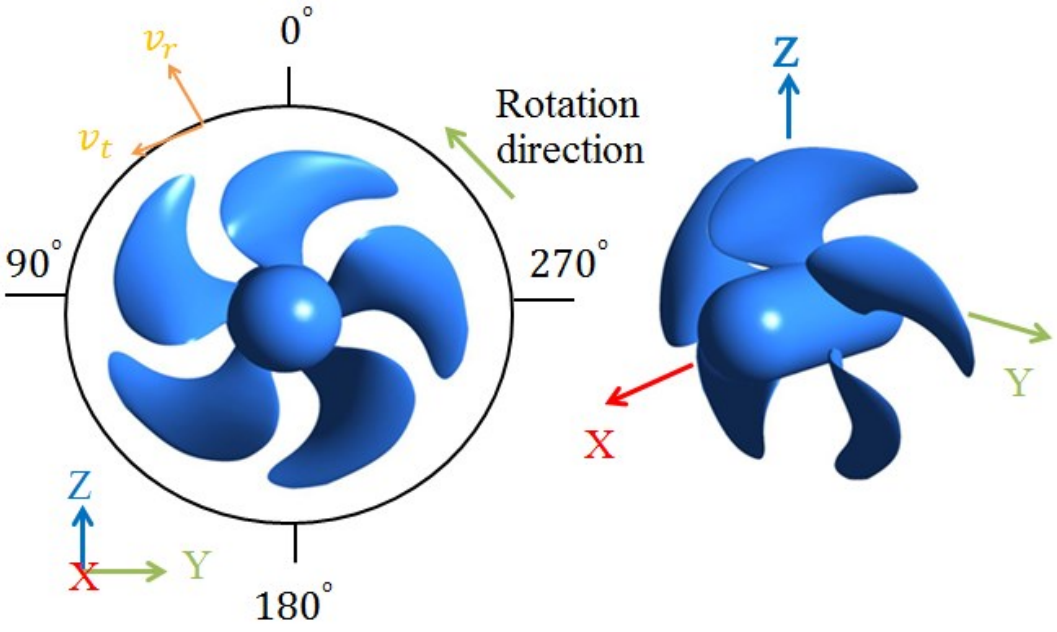

Fig. 2.14 Direction of flow field in oblique flow

(2) Propeller Characteristics

(a) Straight Shaft Condition

The computational results are compared with the experimental data from Naval Surface Warfare Center Carderock Division (NSWCCD) [41]. Fig. 2.15 shows the calculation results of propeller characteristics for two different grids: baseline mesh and refined mesh. The grid independence study is carried out through the comparison with the measurement data. It is found that the accuracy for both mesh are very good including the thrust coefficient K_T, torque coefficient K_Q and propeller efficiency η_o. The maximum error of the calculation is estimated 5 %.

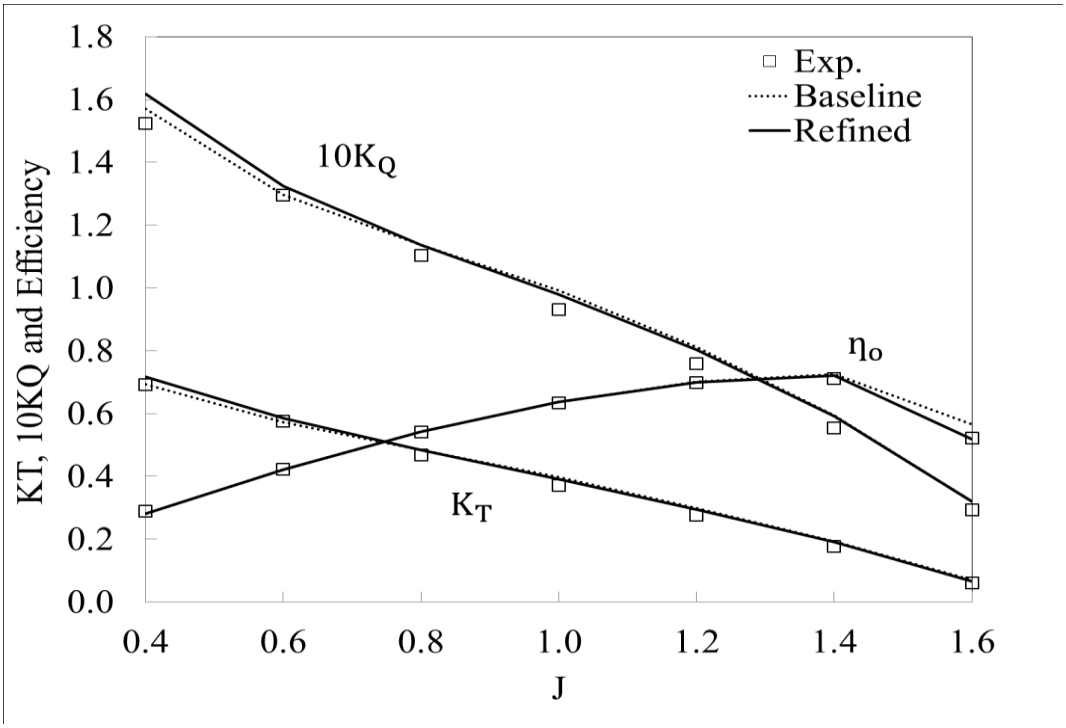

Fig. 2.15 Grid independence study for propeller characteristics of N4990

(b) Inclined Shaft Condition

The measurement results with inclined shaft propellers of NSWCCD [41] are shown in Fig. 2.16. It was found that the effectiveness of inclined shaft 8.8º demonstrated higher efficiency than those of inclined shaft 4.8º and also straight shaft. It is clearly seen that the inclined shaft showed higher efficiency than straight shaft by increment approximately 1-7 %. Thrust coefficient takes similar values regardless of the shaft inclined angle but the torque coefficient is smaller for inclined shaft conditions resulting the better efficiency in those cases.

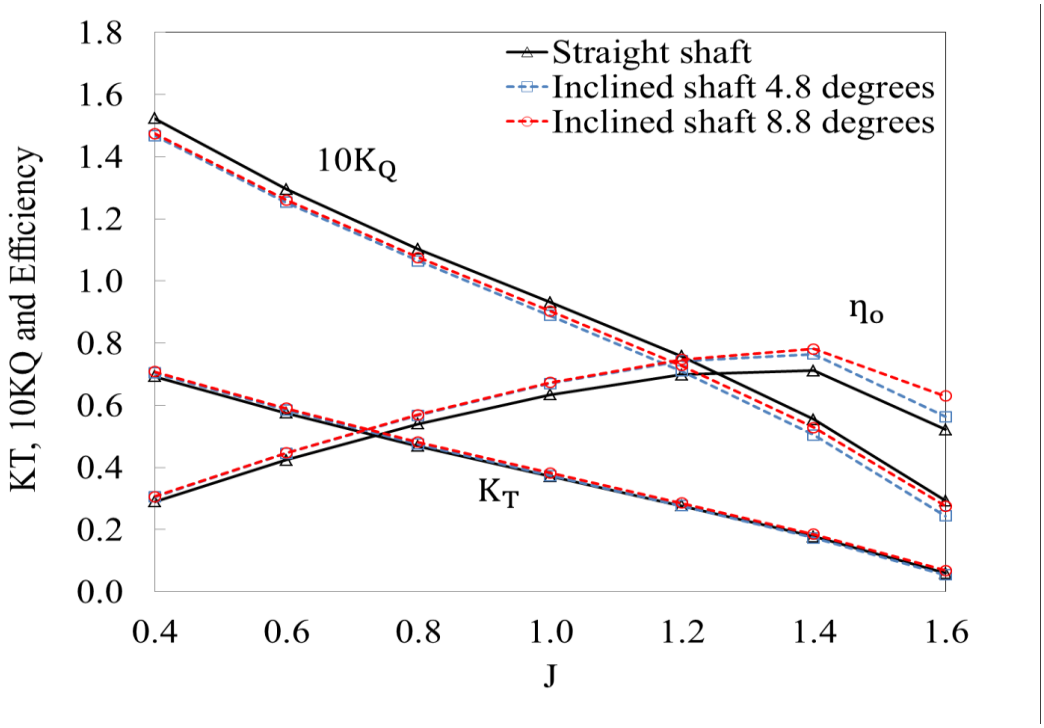

Fig. 2.16 Propeller characteristics of N4990 in experiment with difference inclined shaft angles

The inclined shaft calculations have been performed in uniform inflow with inclined shaft angle. The experiment used N4990 propeller was conducted in open water with different inclined shaft angles. The propeller rotation angle is defined one degree per time step. Figs. 2.17 and 2.18 show calculation results comparing with the measurement data at inclined shaft angles 4.8° and 8.8° respectively. It was found that results of the both conditions have good agreement with the experimental data. The propeller performances comparison of calculated results for straight shaft and inclined shaft angles 4.8° and 8.8° is shown in Fig. 2.19. It is demonstrated that thrust coefficients were seemed equal between straight shaft and inclined shaft with both oblique flow. Torque coefficients of inclined shaft were seemed slightly decreasing from straight shaft. However, propeller efficiency of inclined shaft is increased slightly than that of straight shaft which corresponds to the experimental data.

Figs. 2.20 and 2.21 show single blade thrust and torque coefficients during one rotation of propeller at J = 1.2 with inclined shaft angles 4.8º and 8.8° respectively. It seems that maximum and minimum of them are generated at blade position about 75º and 240º degrees for both angles.

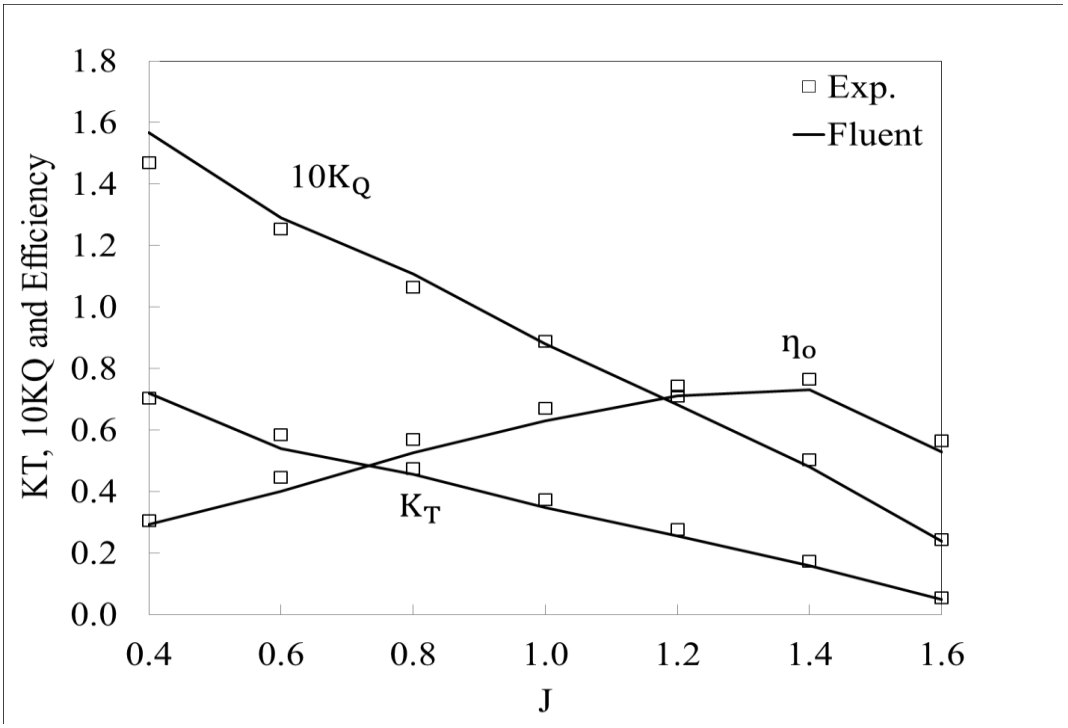

Fig. 2.17 Propeller characteristics of N4990 with inclined shaft angles 4.8º

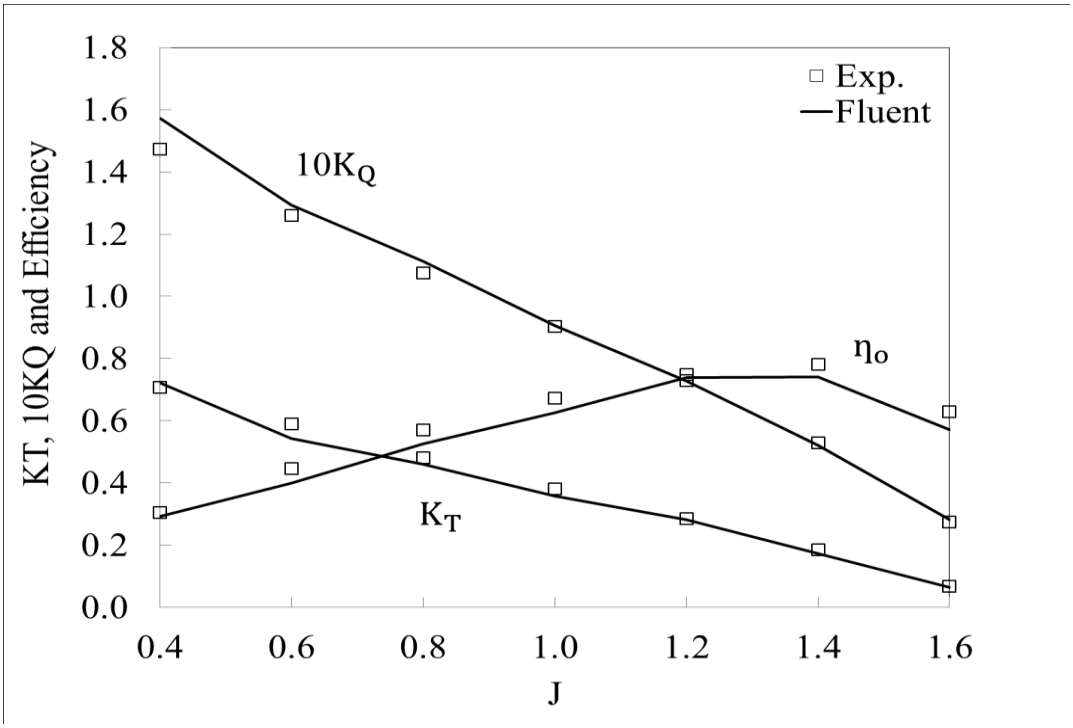

Fig. 2.18 Propeller characteristics of N4990 with inclined shaft angles 8.8º

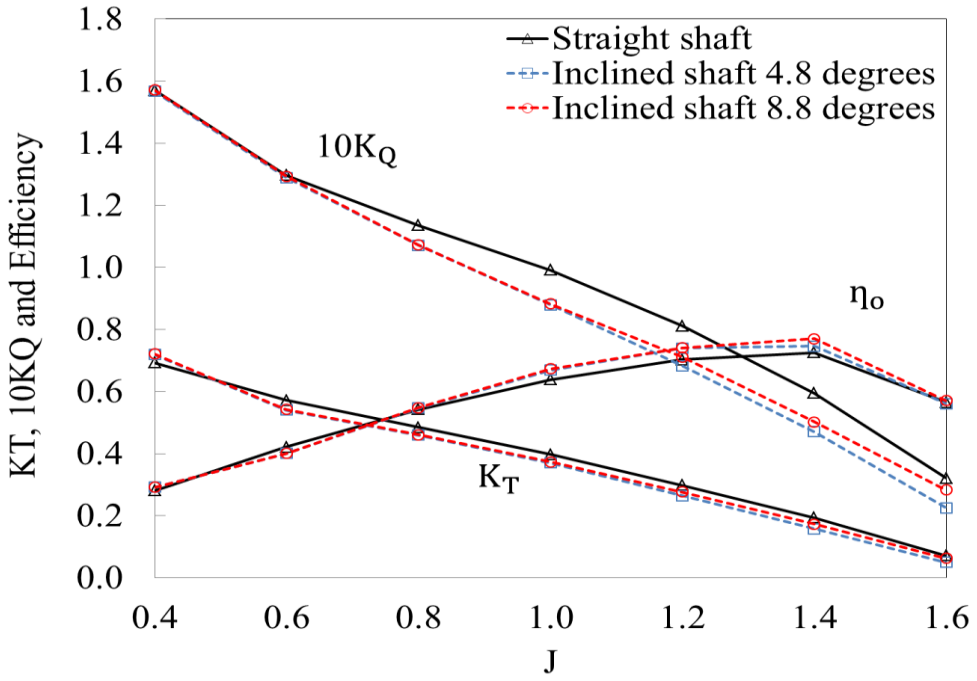

Fig. 2.19 Propeller characteristics of N4990 in calculation with difference inclined shaft angles

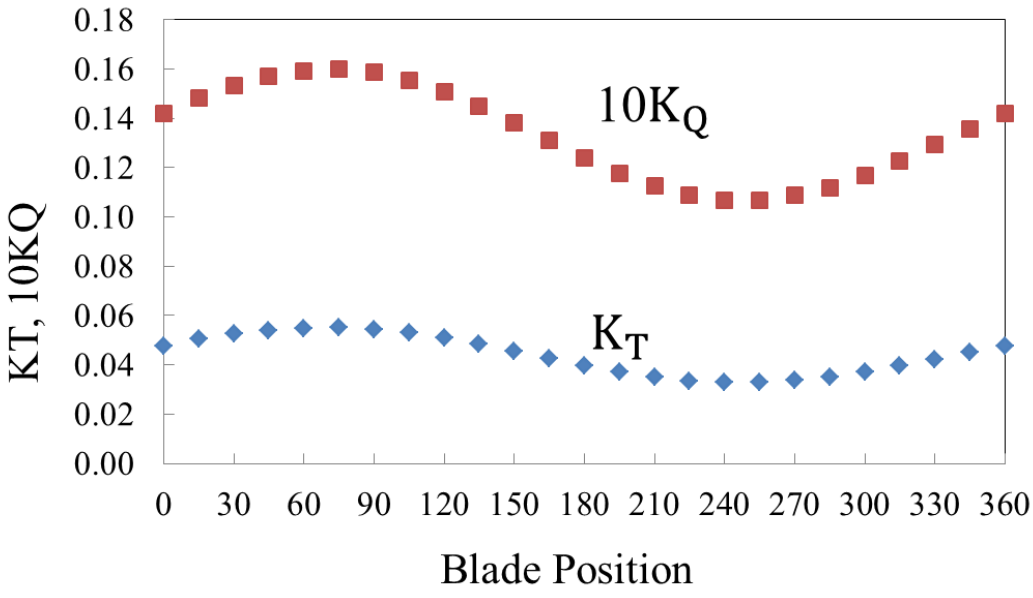

Fig. 2.20 Single blade thrust and torque coefficients for N4990 as functions of blade position at J=1.2 with inclined shaft angles 4.8º.

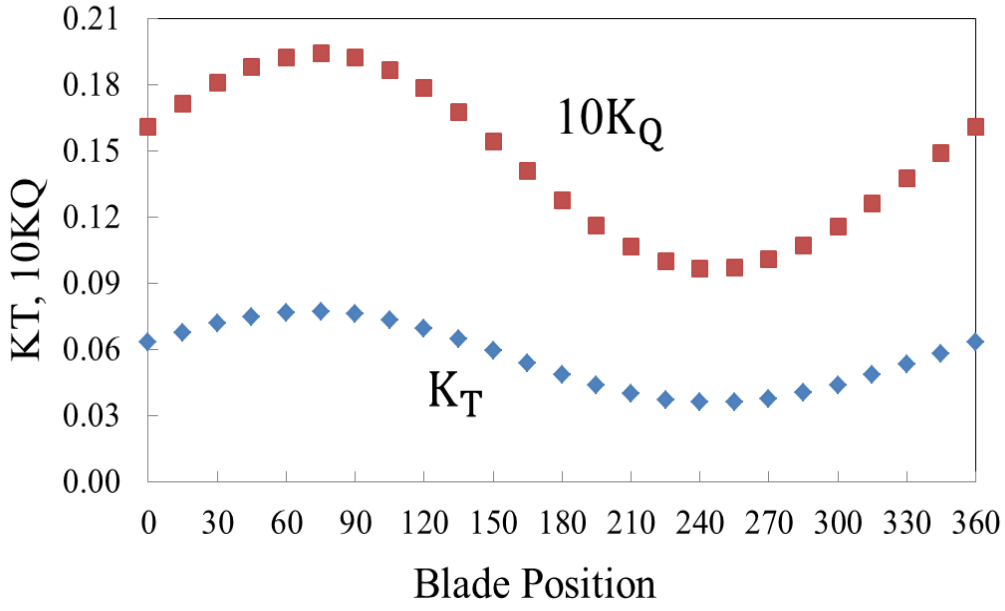

Fig. 2.21 Single blade thrust and torque coefficients for N4990 as functions of blade position at J=1.2 with inclined shaft angles 8.8º

(3) Pressure Distribution on Blade Surface

The second propeller is P4679 as principal particulars of the propeller are shown in Table 2.2. Pressures on blade at pressure and suction sides at r/R=0.5, 0.7 and 0.9 were measured in the experiments. The pressures were analyzed in the form: mean pressure distribution, first harmonic amplitude and first harmonic phase angle.

The calculations were conducted in 2 loading conditions J = 0.719 and 1.078. The time accurate solutions have been determined propeller rotation to one degree per time step. Fig. 2.22 shows the calculation results of pressure coefficient, $C_p(\theta)$ at single point on the blade for r/R=0.7, x/c=0.65 at J=0.719 during one rotation of propeller comparing with measurement data at pressure and suction sides. It was found that the calculation results agree well with measurement data at pressure side but it seemed sliding down from experiment at suction side. The minimum and maximum of pressure coefficients, $C_p(\theta)$ correspond with angular position of blade about 120º and 300º respectively which accorded the measurement at both sides.

Figs. 2.23 to 2.25 show numerical calculation of the mean pressure $C_{p,m}$, first harmonic amplitude $C_{p,1}$ and first harmonic phase angle $\emptyset_1$ from three radial position at J = 0.719 respectively. $C_{p,m}$, $C_{p,1}$ and $\emptyset_1$ can be found from that the Eq. (2.30) and relatives of $C_p(\theta)$. The calculated results have good agreement with the measurement data. Figs. 2.26 to 2.28 show numerical computation of $C_{p,m}$, $C_{p,1}$ and $\emptyset_1$ at J = 1.078, and the same radial positions with J = 0.719 respectively. The calculated results agree well with experimental data.

The contours of static pressure (pascal) on the pressure and suction sides on the blade at J = 1.078 which are corresponding for the inclined flow configuration are shown in Fig. 2.29.

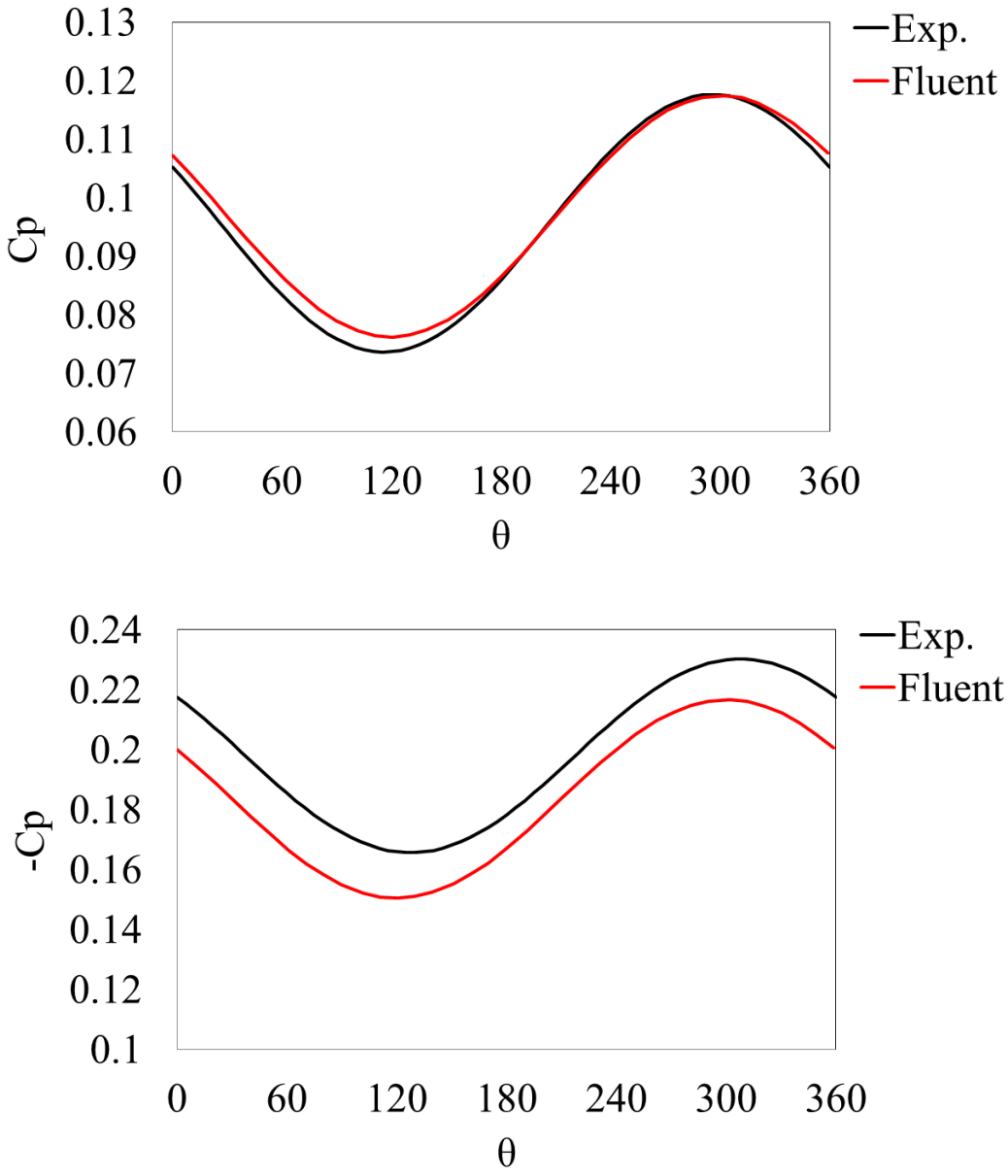

Fig. 2.22 Pressure distribution of P4679 for r/R=0.7, x/c=0.65 and J=0.719 on pressure side (upper) and suction side (lower)

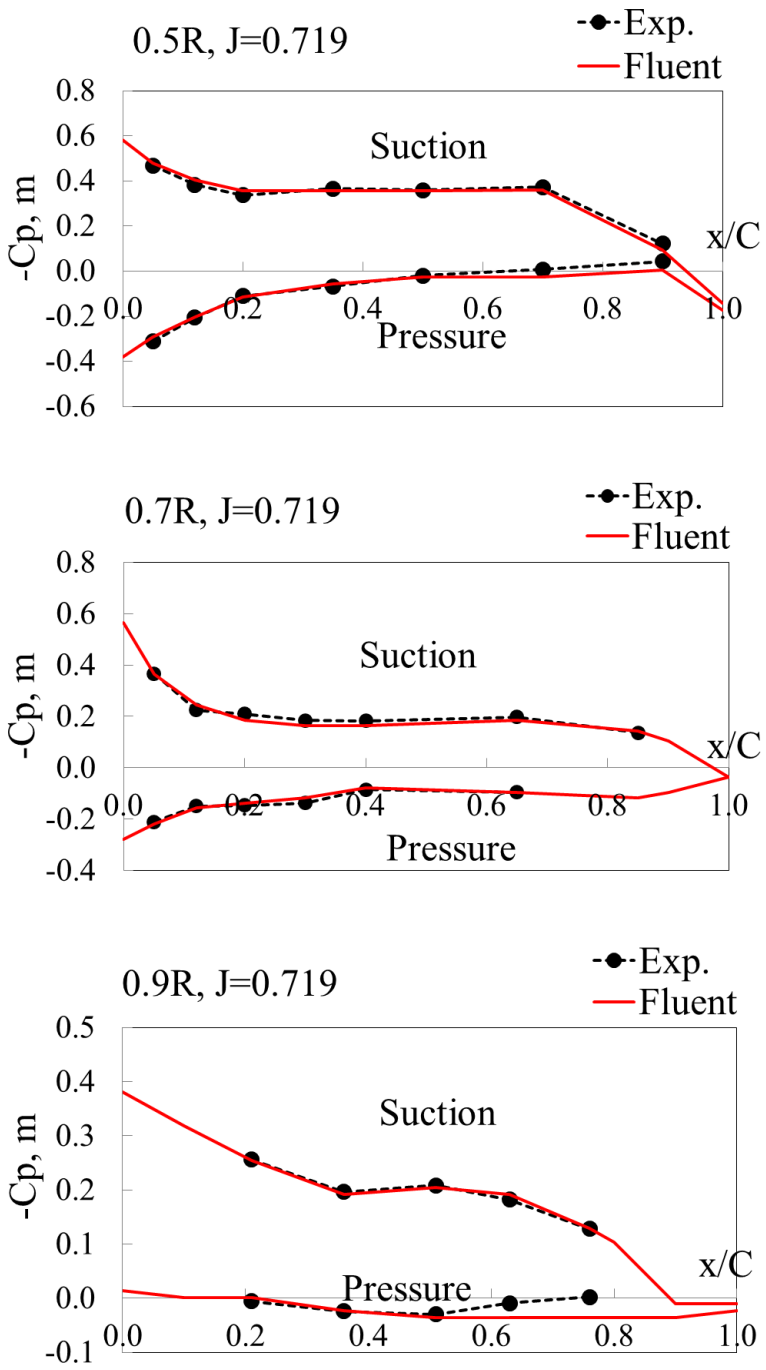

Fig. 2.23 Mean pressure distribution of P4679 at J=0.719 for r/R=0.5 (upper), r/R=0.7 (middle) and r/R=0.9 (lower)

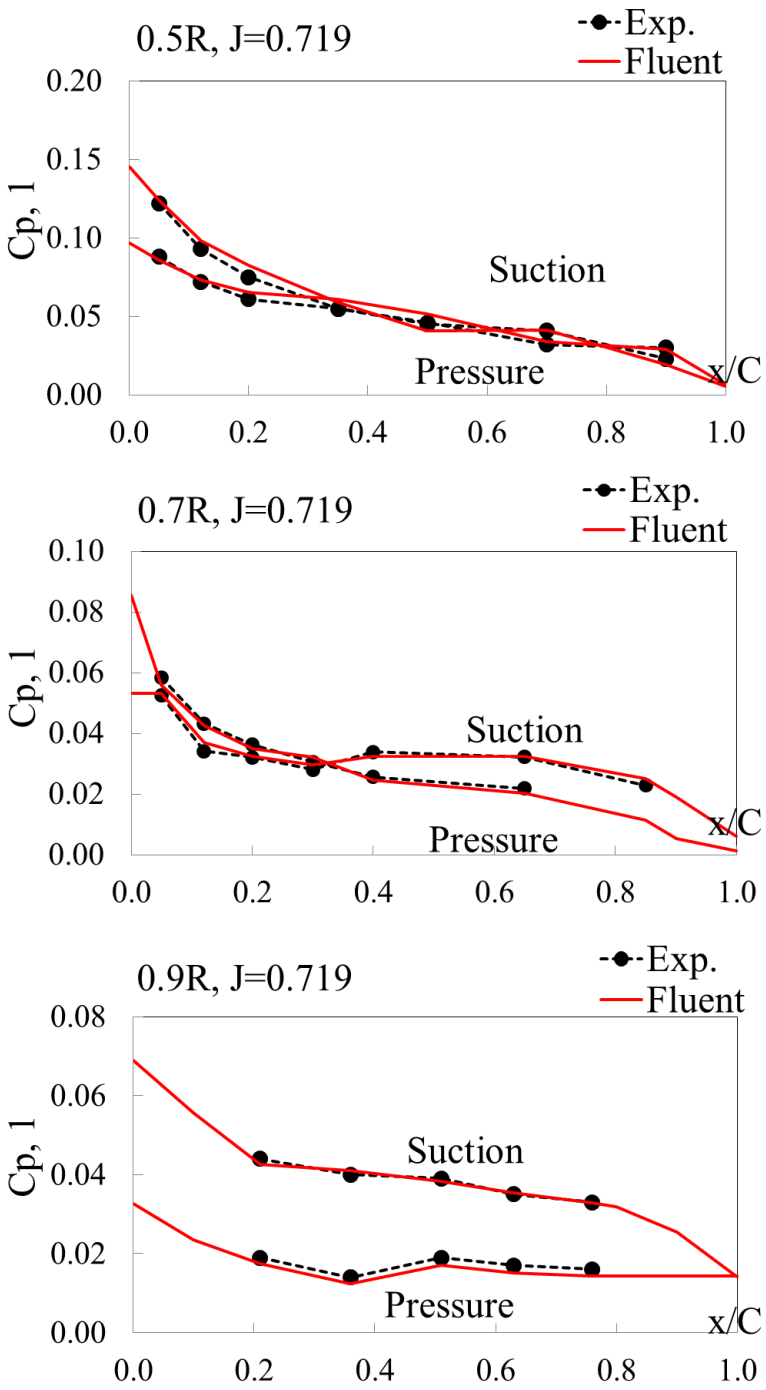

Fig. 2.24 First harmonic amplitude of P4679 at J=0.719 for r/R=0.5 (upper), r/R=0.7 (middle) and r/R=0.9 (lower)

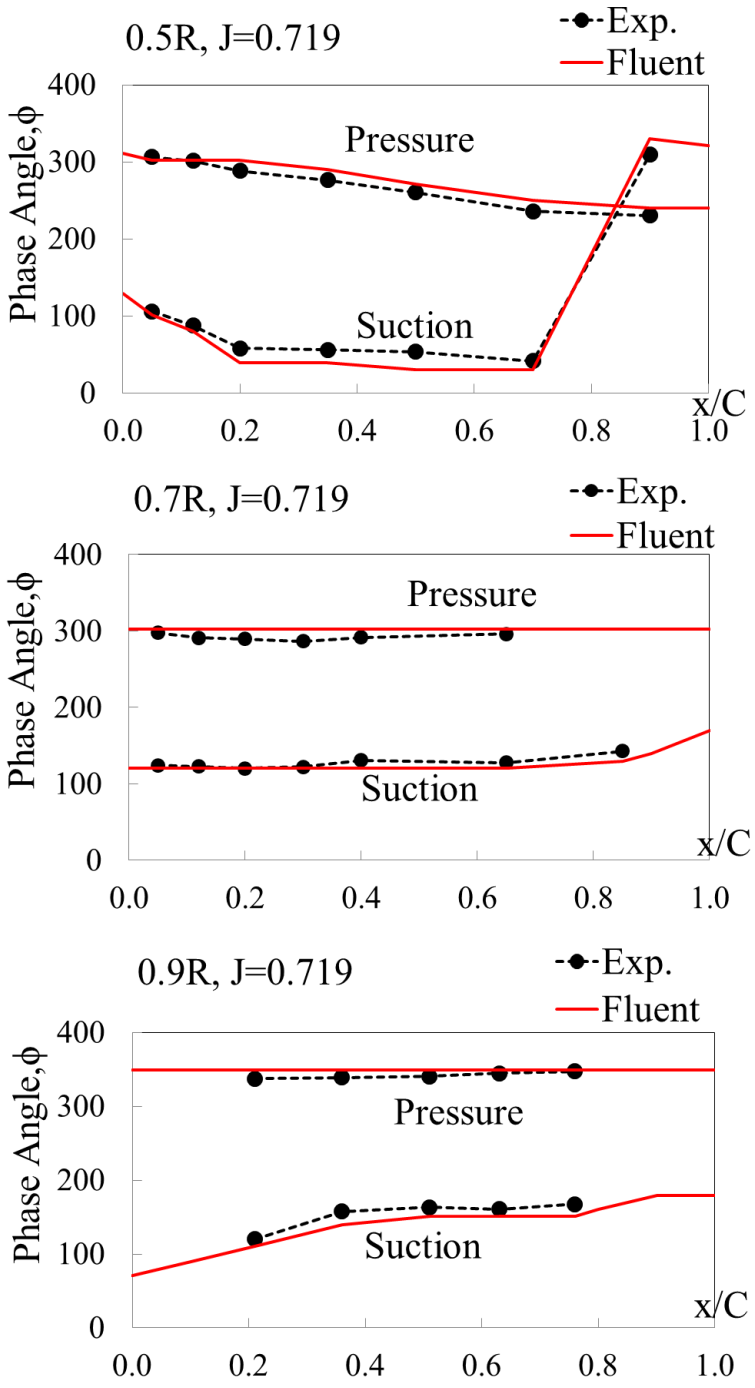

Fig. 2.25 First harmonic phase angle of P4679 at J=0.719 for r/R=0.5 (upper), r/R=0.7 (middle) and r/R=0.9 (lower)

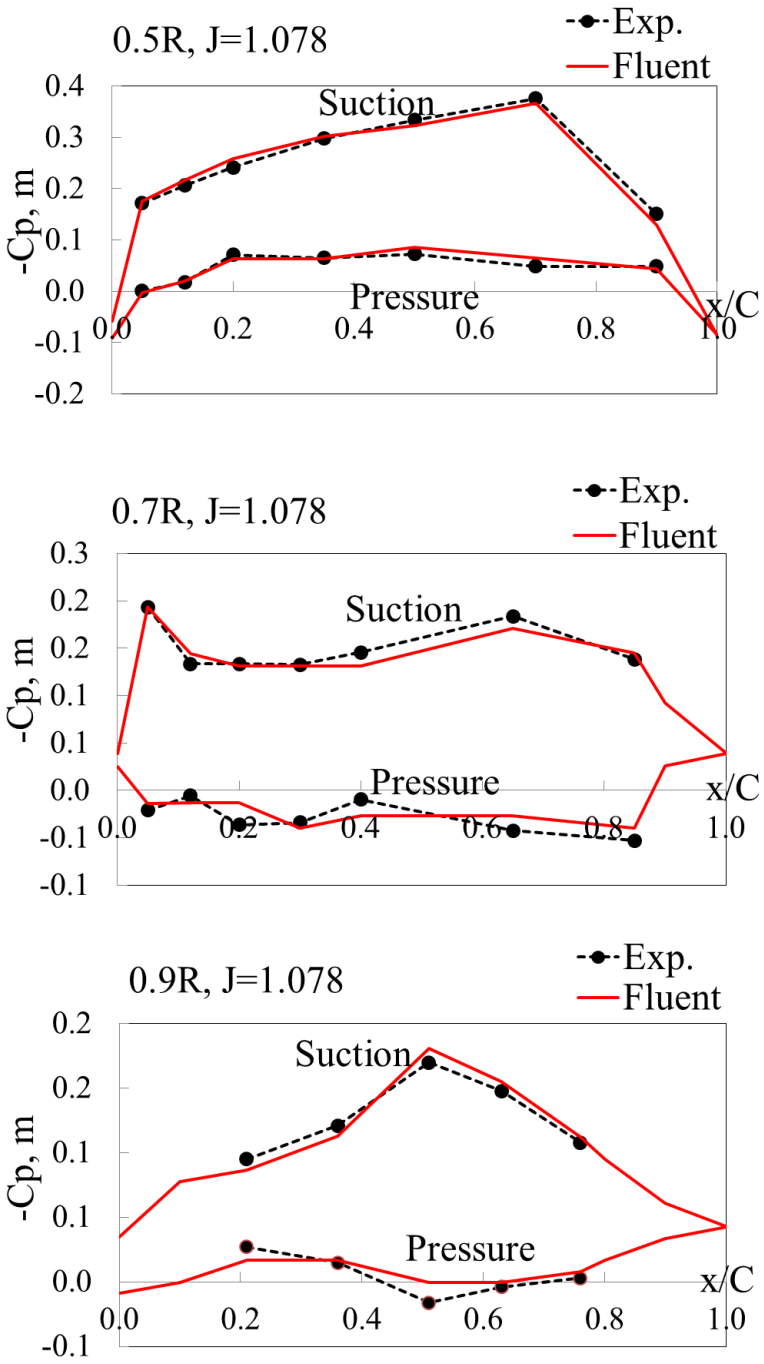

Fig. 2.26 Mean pressure distribution of P4679 at J=1.078 for r/R=0.5 (upper), r/R=0.7 (middle) and r/R=0.9 (lower)

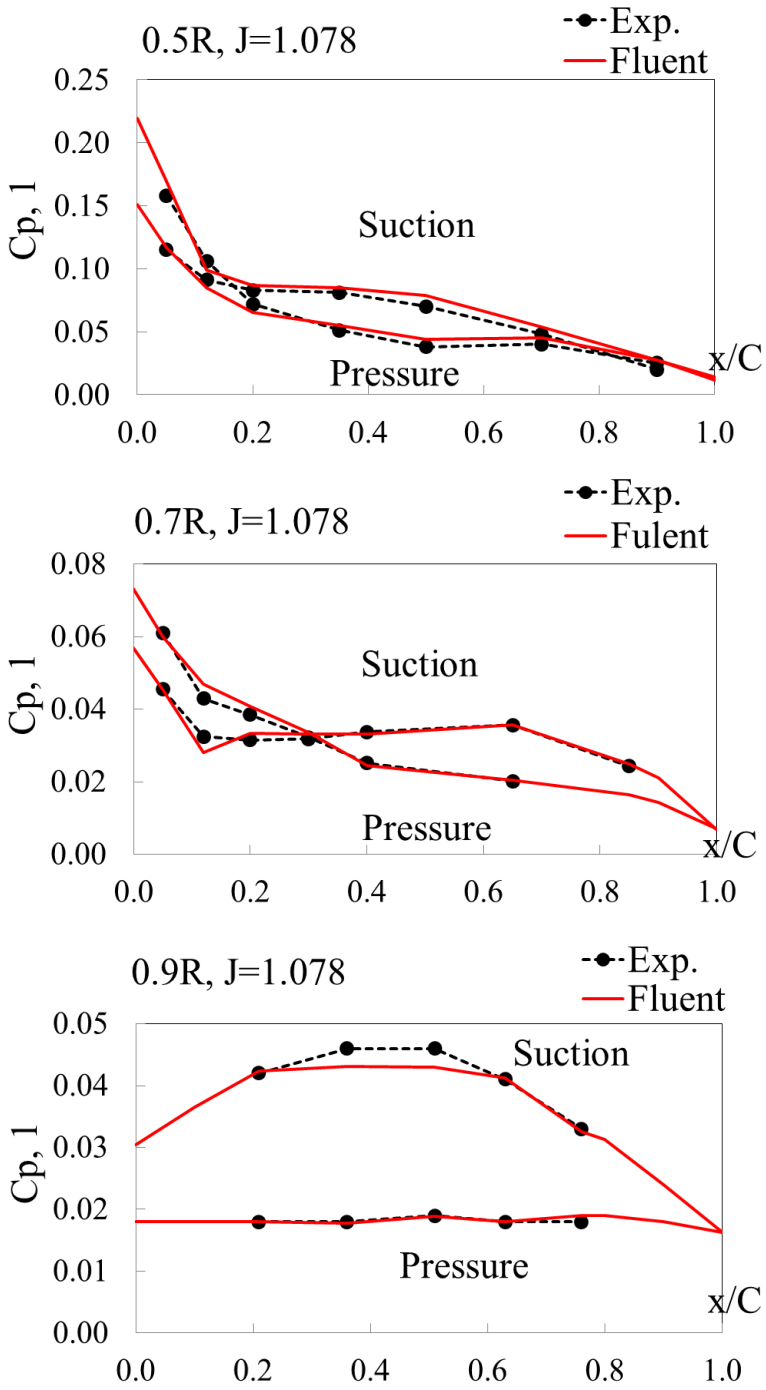

Fig. 2.27 First harmonic amplitude of P4679 at J=1.078 for r/R=0.5 (upper), r/R=0.7 (middle) and r/R=0.9 (lower)

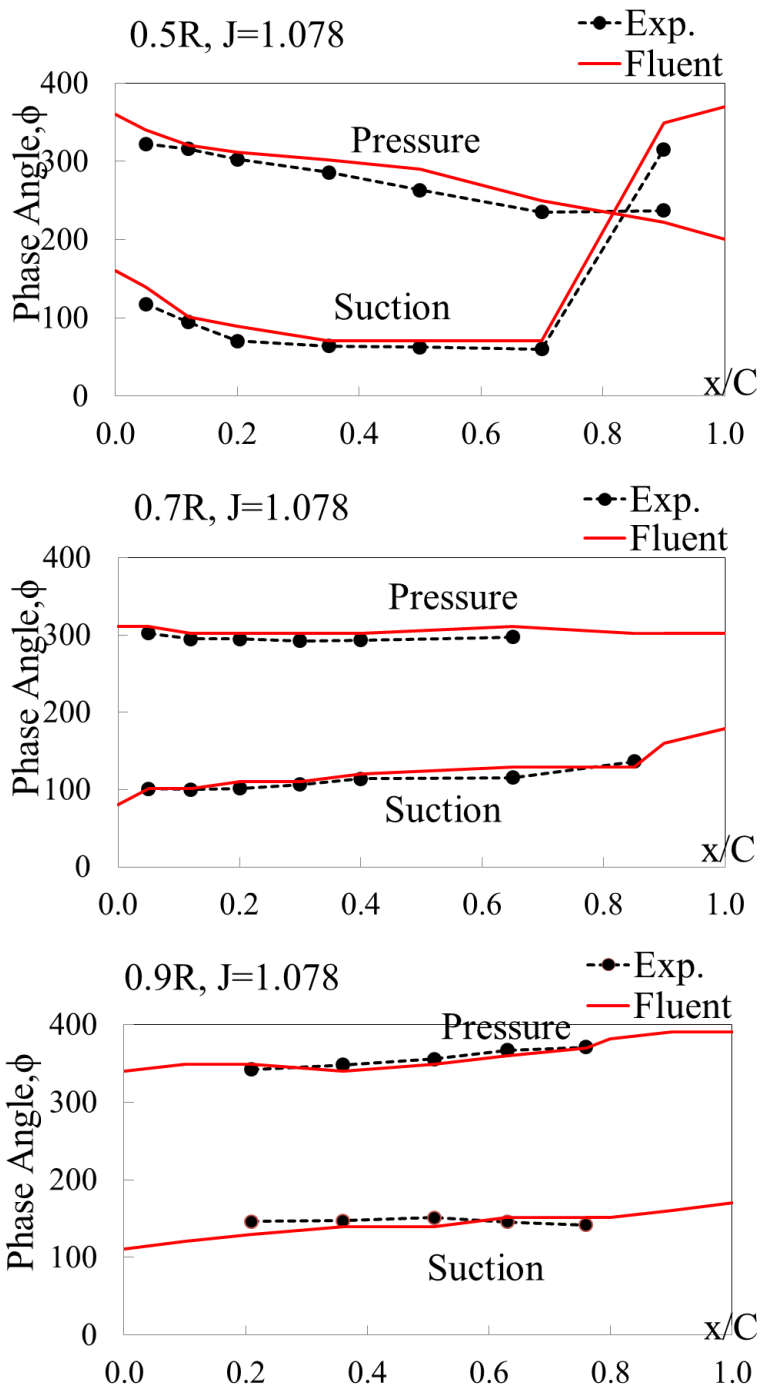

Fig. 2.28 First harmonic phase angle of P4679 at J=1.078 for r/R=0.5 (upper), r/R=0.7 (middle) and r/R=0.9 (lower)

Fig. 2.29 Pressure distributions of P4679 at J=1.078 on suction side (left) and pressure side (right)

2.4 Conclusion

In this chapter, CFD analysis system based on the ANSYS Fluent for evaluation of propeller performance in straight and inclined shaft conditions was described. Validation on the present method was conducted referring the experimental data of two well-known propellers. As a result, the following are confirmed.

(1) In the experiment of N4990 propeller, the propeller characteristics (thrust, torque and propeller efficiency) change by inclined shaft angle. Especially the propeller efficiency in inclined shaft condition is higher than that in straight shaft condition by approximately 1-7%. The tendency of the calculated results is nearly the same to the experimental data.

(2) The calculated mean pressure distribution, first harmonic amplitude and first harmonic phase angle were compared with experimental data of P4679 propeller. The calculated results agree well with the experimental data.

Therefore the presented CFD analysis system seems to be applicable for evaluation of Long-Tail Boat propeller performance.

Chapter 3
Characteristics of Long-Tail Boat Propeller

3.1 Introduction

In this chapter, model test of the standard propeller of Long-Tail Boat from Bangkok in Thailand is conducted in straight shaft condition by using the high speed circulating water channel at Kyushu University. Next, the characteristics of Long-Tail Boat model propeller are calculated by the present CFD analysis system and compared with the experimental data. In addition, the calculation by using a simple surface method "SQCM" [14] which is used for propeller blade shape optimization in Chapter 4 is conducted and the accuracy of SQCM is confirmed.

3.2 Long-Tail Boat Propeller and Its Operating Condition

In this study, the general Long-Tail Boat in the Chao Phraya River, Bangkok of Thailand is focused on. Fig 3.1 shows the propeller and shaft of the Long-Tail Boat studied here. The propeller diameter is 0.34 m and the shaft length is 4.5 m. Fig. 3.2 shows one of the actual standard propeller purchased from a boat owner living in Bangkok.

The boat speed and propeller revolution were measured in the Chao Phraya River, Bangkok of Thailand on December 27, 2013. The relation between boat speed and propeller revolution is shown in Fig. 3.3. The propeller advance velocity is assumed nearly equal to the boat speed because the propeller is operating very far from boat hull. So the relation between the propeller advance velocity and advance coefficient is shown in Fig. 3.4. Assuming the normal speed of the Long-Tail Boat is about 50 km/h, advance

coefficient is nearly equal to 1.1. In this study, the designed advance coefficient is set to 1.1.

Fig. 3.1 Propeller and shaft of Long-Tail Boat

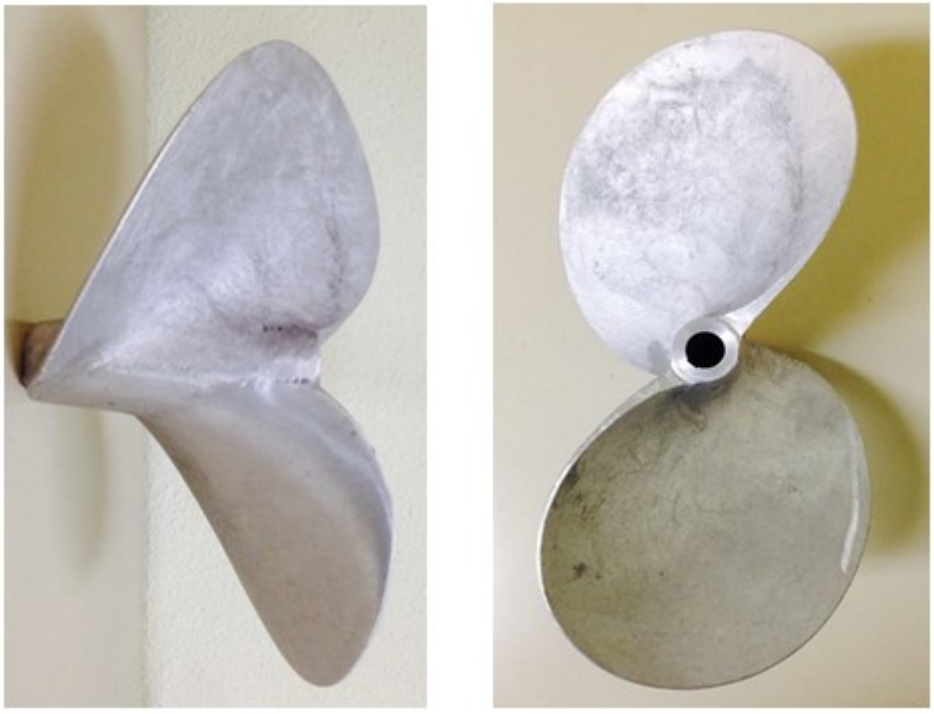

Fig. 3.2 Full scale of Long-Tail Boat propeller at side view (left) and top view (right)

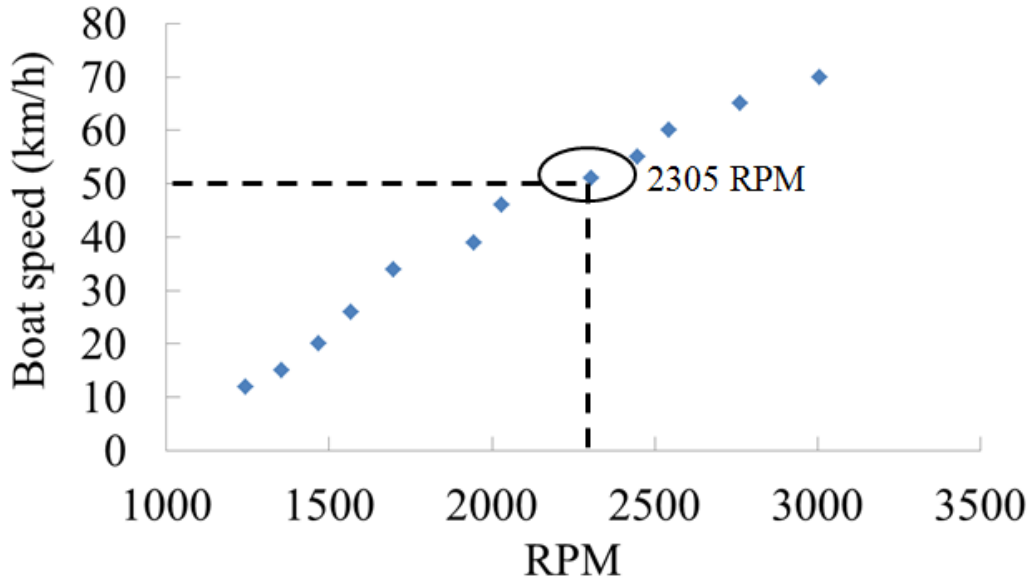

Fig. 3.3 Boat speed versus propeller revolution

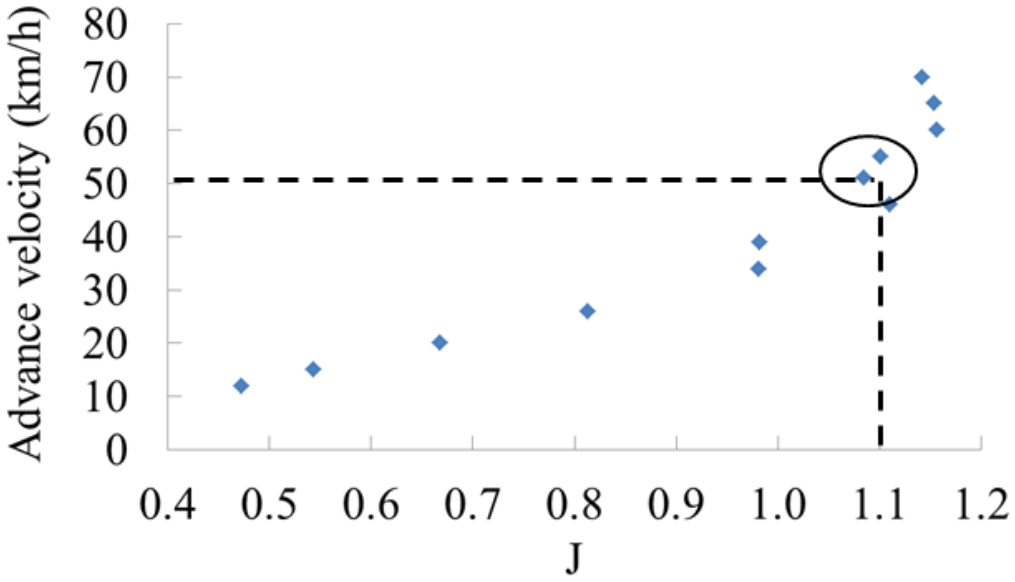

Fig. 3.4 Propeller advance velocity versus advance coefficient

3.3 Experiment

In order to evaluate the characteristics of standard Long-Tail Boat propeller (abbreviated to LTBP) shown in Fig. 3.2, the model test was conducted by using the high speed circulating water channel at Kyushu University. Prior to the model test, the actual propeller geometry was measured at Institute Technology Center of Nagasaki by using a three dimensional optical scanner. Fig. 3.5 shows the same type of 3D scanner equipment.

After smoothing the propeller geometry, the model propeller was made. The principal particulars of the model propeller are shown in Table 3.1. The diameter of the model propeller was decided considering the designed advance coefficient, the capacity of the propeller dynamometer and the current speed of high speed circulating water channel. Fig. 3.6 shows the model of the standard LTBP. The pitch, maximum camber, maximum thickness, chord, rake and leading edge position at each radial position are shown in Figs. 3.7 to 3.12, respectively. The definitions of rake and leading edge position can be found in Appendix B. The blade sections of the LTBP at each radial position are shown in Fig. 3.13.

Fig. 3.5 Scanners for measured propeller geometry

Table 3.1 Principal Particulars of Long-Tail Boat propeller

Model name	LTBP
Type of propeller	Fixed Pitch
Numbers of blade	2
Diameter [mm]	200
Expanded area ratio	0.6
Pitch ratio at 0.7R	1.289
Direction of rotation	Right Hand
Design advance coefficient [J]	1.1

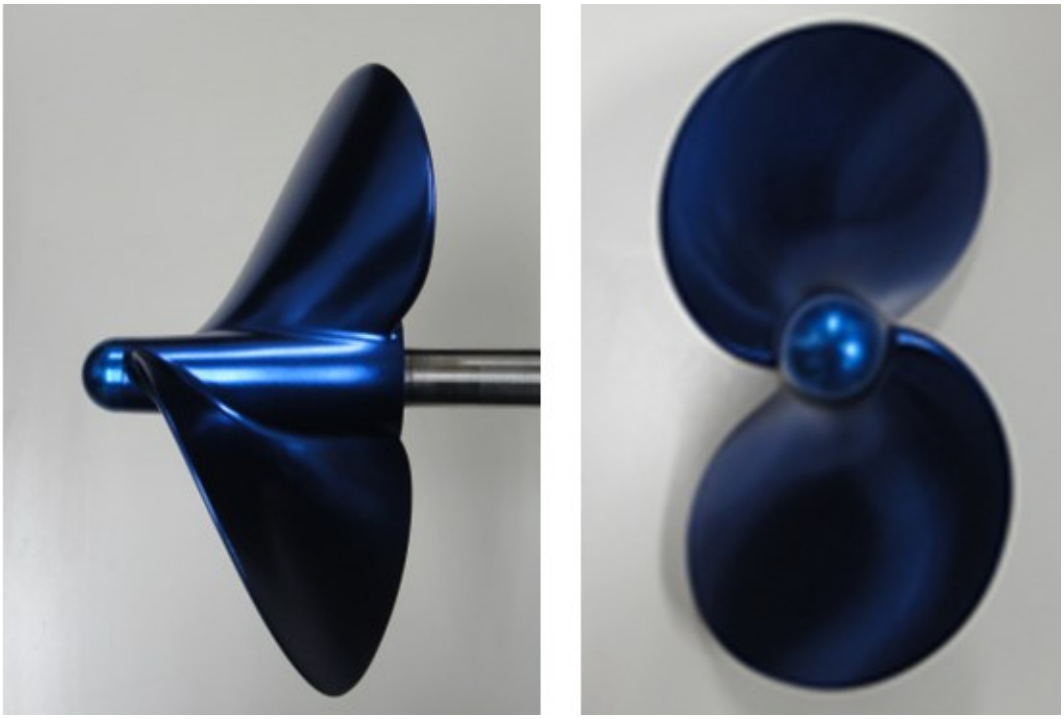

Fig. 3.6 Model of standard LTBP at side view (left) and front view (right)

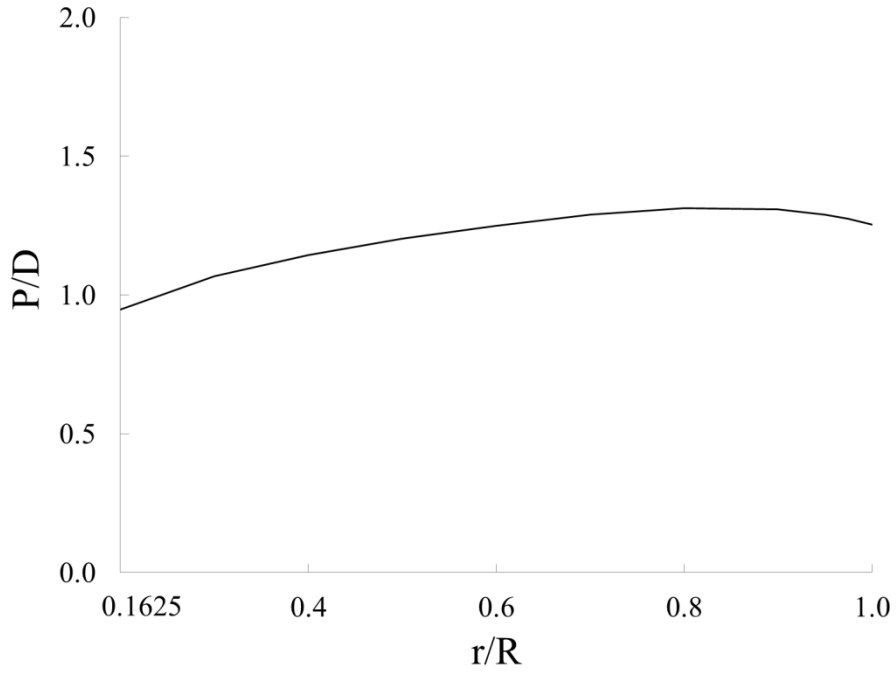

Fig. 3.7 Pitch distribution

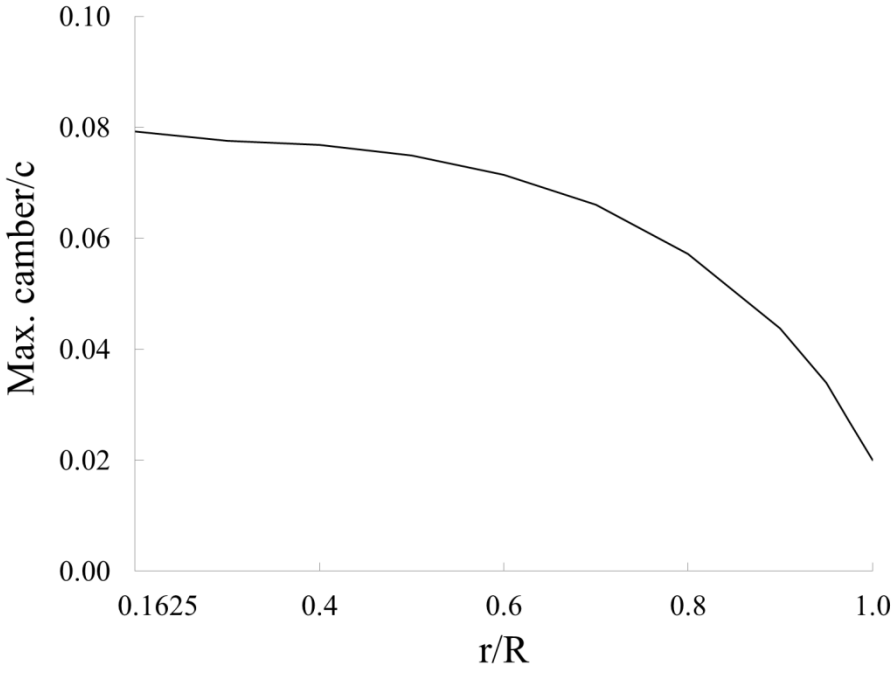

Fig. 3.8 Maximum camber distribution

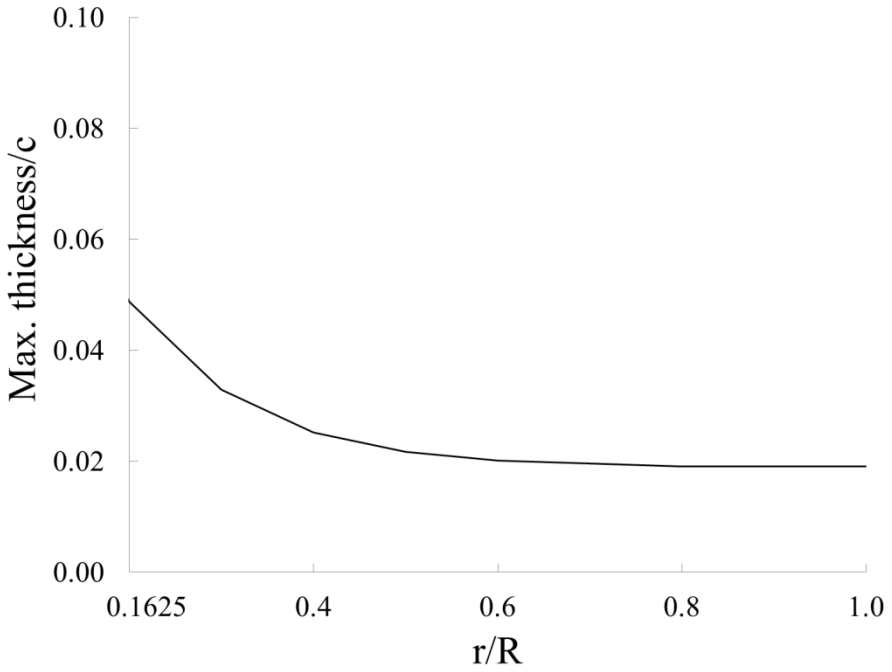

Fig. 3.9 Maximum thickness distribution

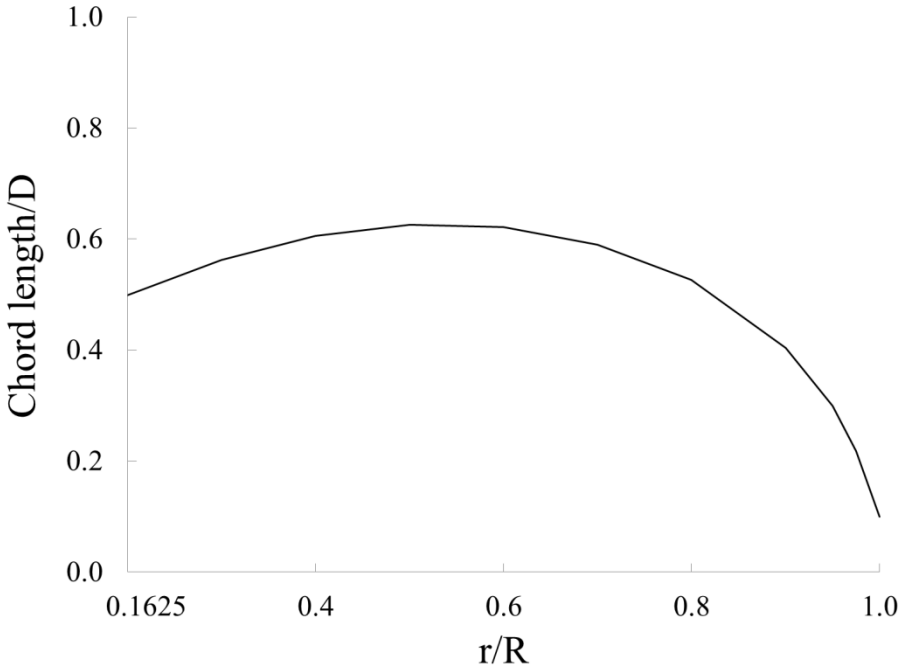

Fig. 3.10 Chord distribution

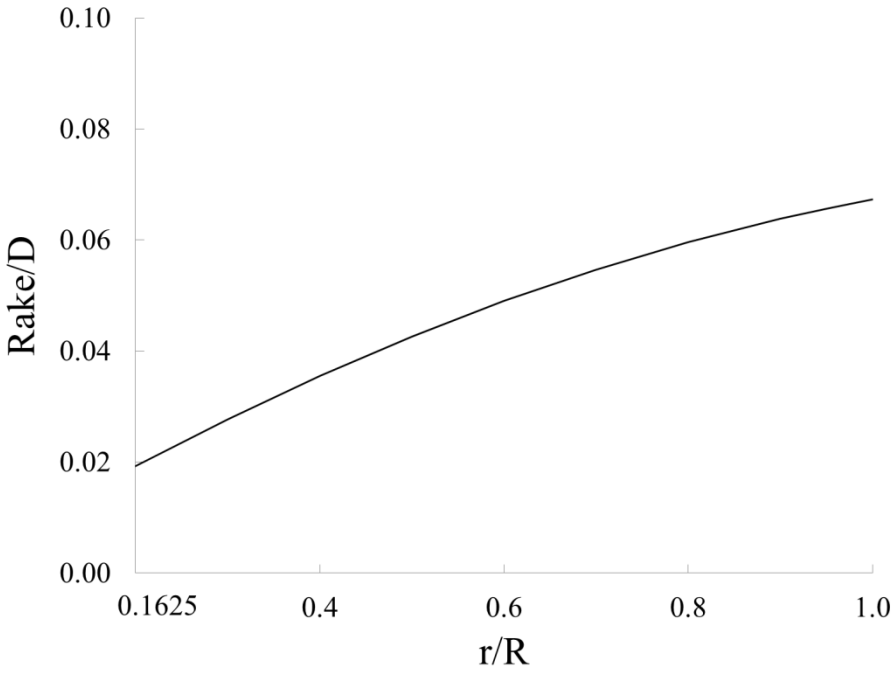

Fig. 3.11 Rake distribution

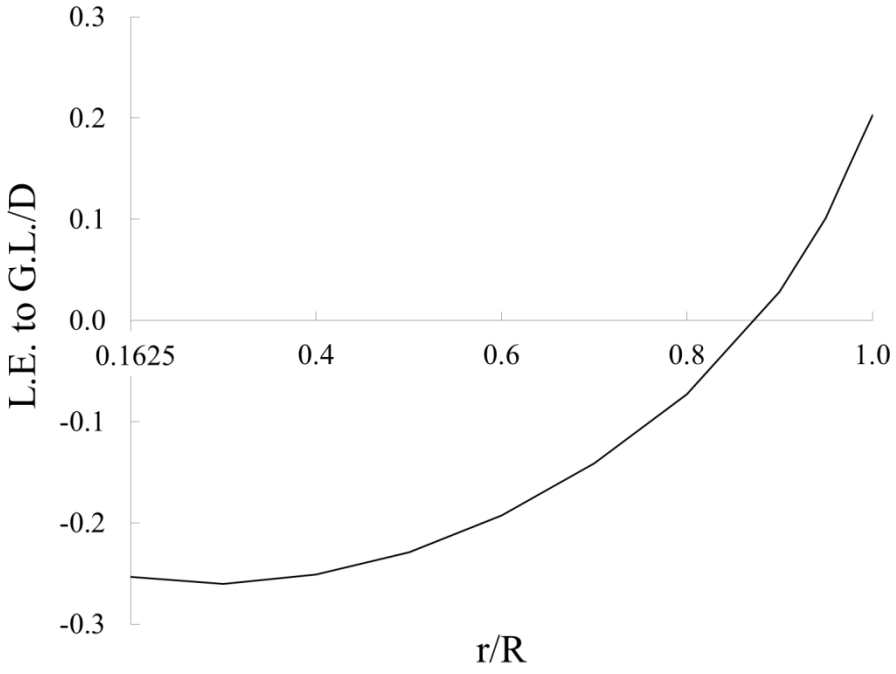

Fig. 3.12 Distribution of leading edge position

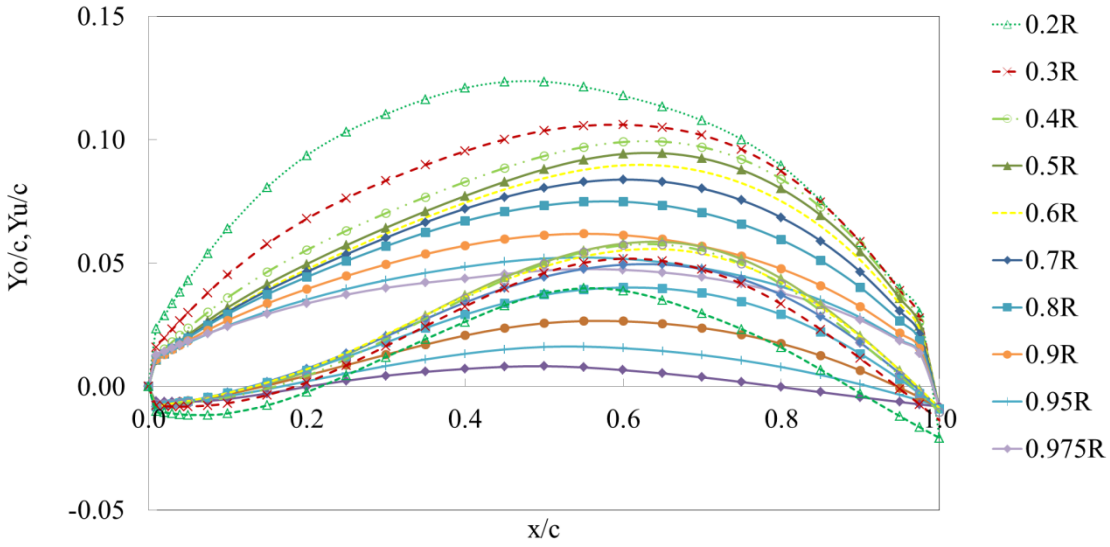

Fig. 3.13 Blade sections at each radial position

The model test of the standard LTBP was conducted by using the high speed circulating water channel at Kyushu University. The specifications are length ≈ 21m, width ≈ 3 m and depth ≈ 7 m respectively. The test sections are length ≈ 6m, width ≈ 2 m and depth ≈ 1 m respectively. Fig. 3.14 shows the arrangement of it. Fig. 3.15 shows the measurement system in order to measure the thrust and torque of the propeller. The ranges of testing are imposed the advance coefficient, J= 0.5-1.4 and propeller rotational speed was fixed 10 rps.

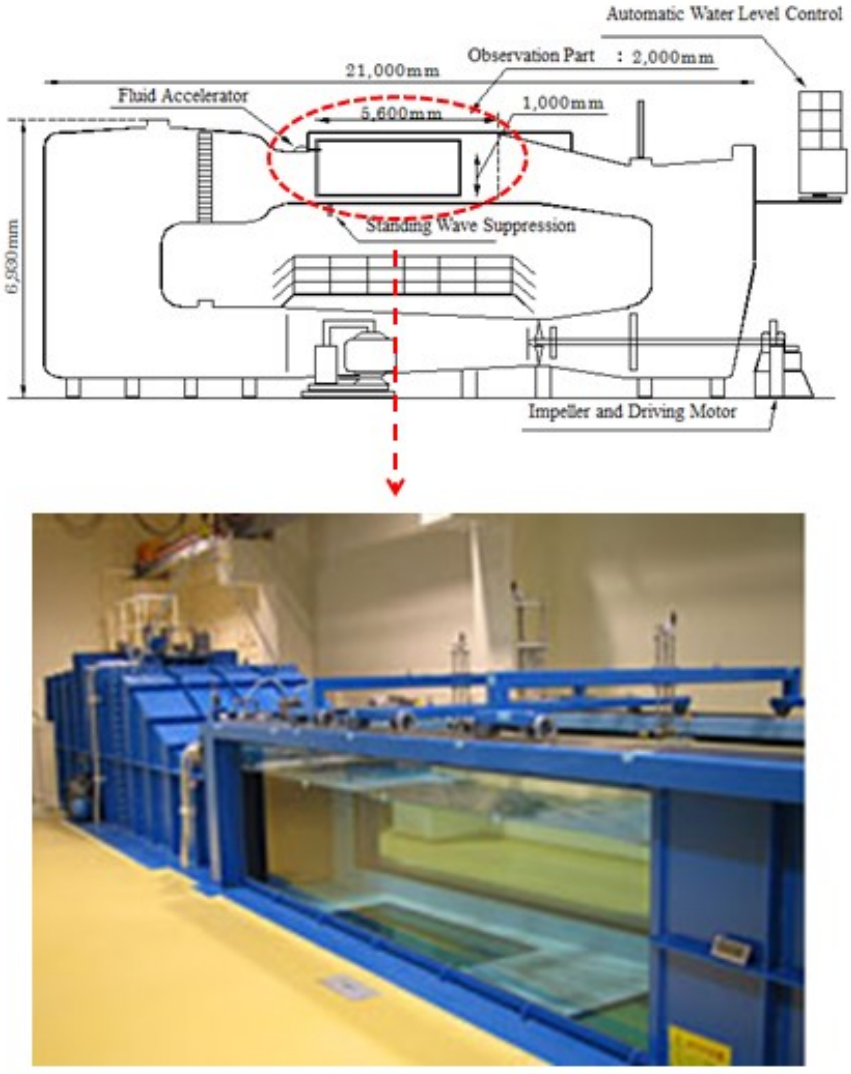

Fig. 3.14 High speed circulating water channel

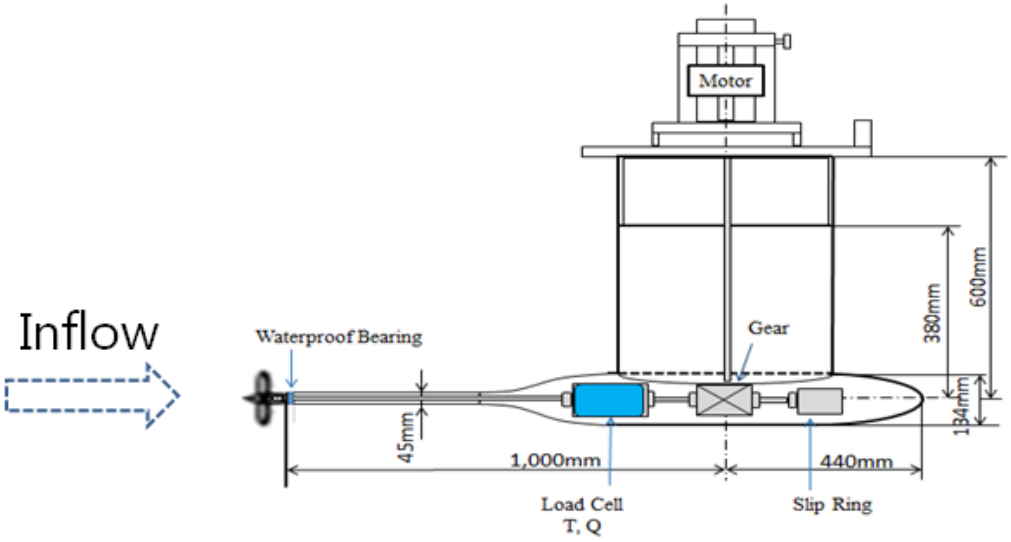

Fig. 3.15 Propeller measurement system

3.4 Computational Domain and Meshing

In this chapter the steady-state analysis with uniform inflow have been performed therefore only one blade was simulated for computational calculation by using periodic boundary condition. The computational domain is made a one-half cylindrical volume including the propeller and hub as shown in Fig. 3.16. It was split into two regions which are a rotating and stationary. The rotating part called “Rotating” and the fixed part called “Stationary”.

Boundary conditions were imposed to simulate the flow around a rotating propeller in open water by the moving reference systems. Inlet component set velocity inlet with the given inflow speed. Turbulence intensity and turbulence viscosity in this condition were used to 3%. Outlet component set static pressure to constant equal zero. No-slip boundary condition was imposed for solid surfaces (blade and hub). Free-slip boundary condition was set for outer surface.

The dimensions of computational domains are defined in Table 3.2 where D is the diameter of propeller.

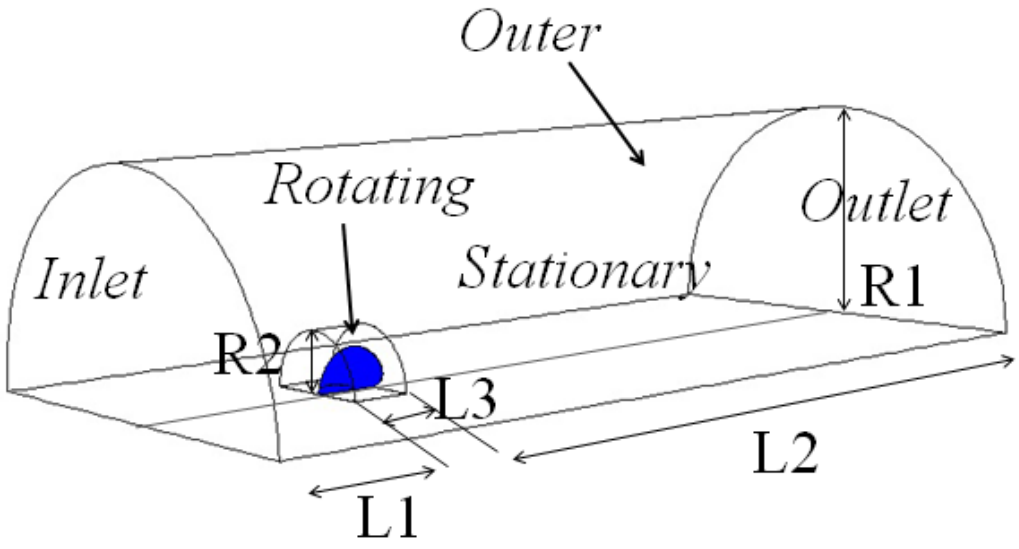

Fig. 3.16 Computational domain of calculation

Table 3.2 Dimension of computational domains

	Rotating	Stationary
L1		2.2D
L2		7.15D
L3	0.65D	
R1		2.5D
R2	0.65D	

The computational domains were generated by automated mesh generation technique with unstructured cells. The mesh in rotational domain including blade and hub were discretized by hybrid-unstructured control volume mesh as shown in Fig. 3.17. Fig. 3.18 shows the surface mesh on the propeller blade. The grid independence was determined about 1.6 million cells for total grids which are divided into rotating part and stationary part contain about 1 million and 0.6 million cells respectively. The prismatic layers were imposed about 15 layers around blade. Fig. 3.19 shows the prismatic layers and mesh beside blade and hub. The average values of y^+ on the solid surfaces (blade and hub) were found to be 25.

In order to confirm the accuracy of SQCM [14] which is used optimization in Chapter 4, calculation by SQCM was also conducted. Outline of SQCM is described in Appendix B. Fig 3.20 shows the panel arrangement in SQCM. Each blade was divided into 10 panels in the radial direction and 15 panels in the chord-wise direction.

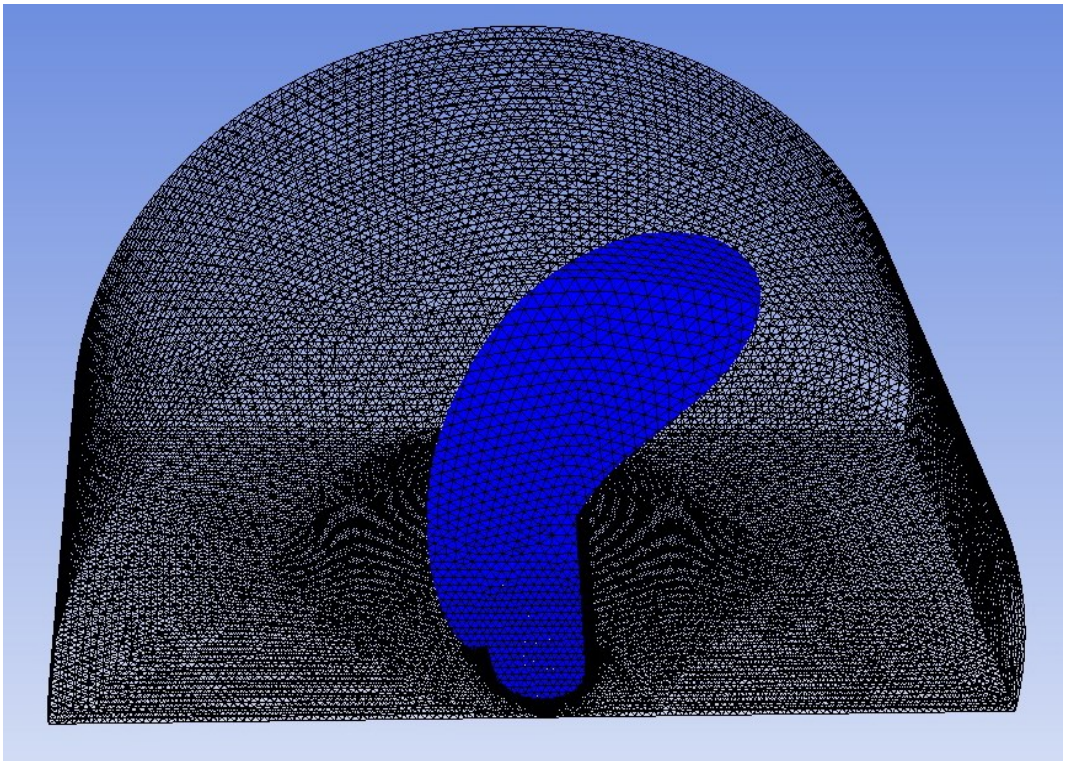

Fig. 3.17 Mesh in rotational domain for original LTBP

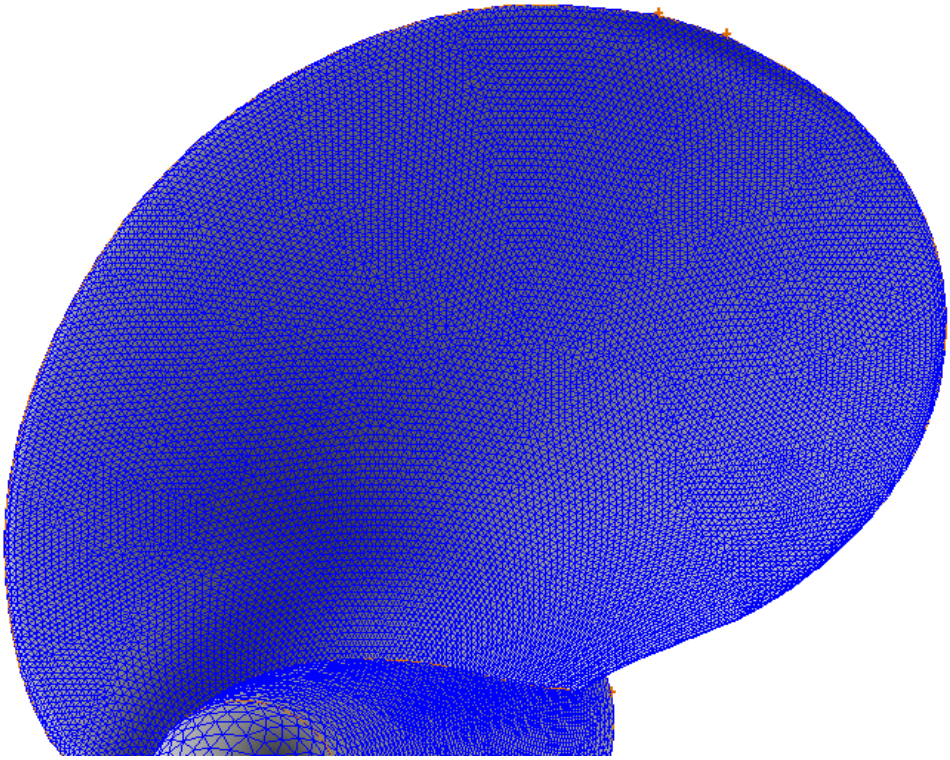

Fig. 3.18 Surface mesh on the blade for original LTBP

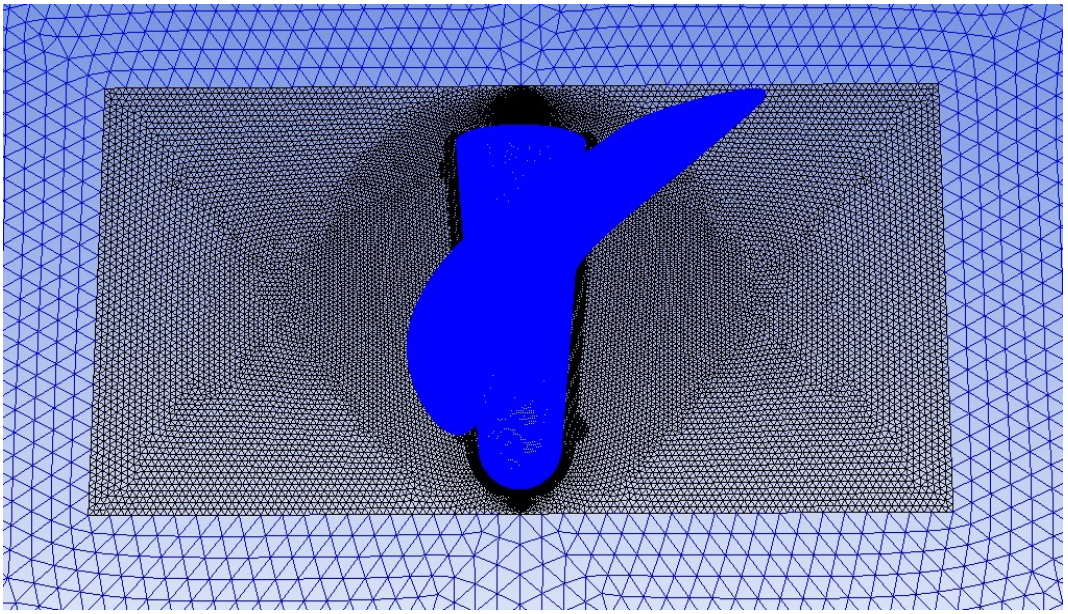

Fig. 3.19 Prismatic cells and mesh beside hub for original LTBP

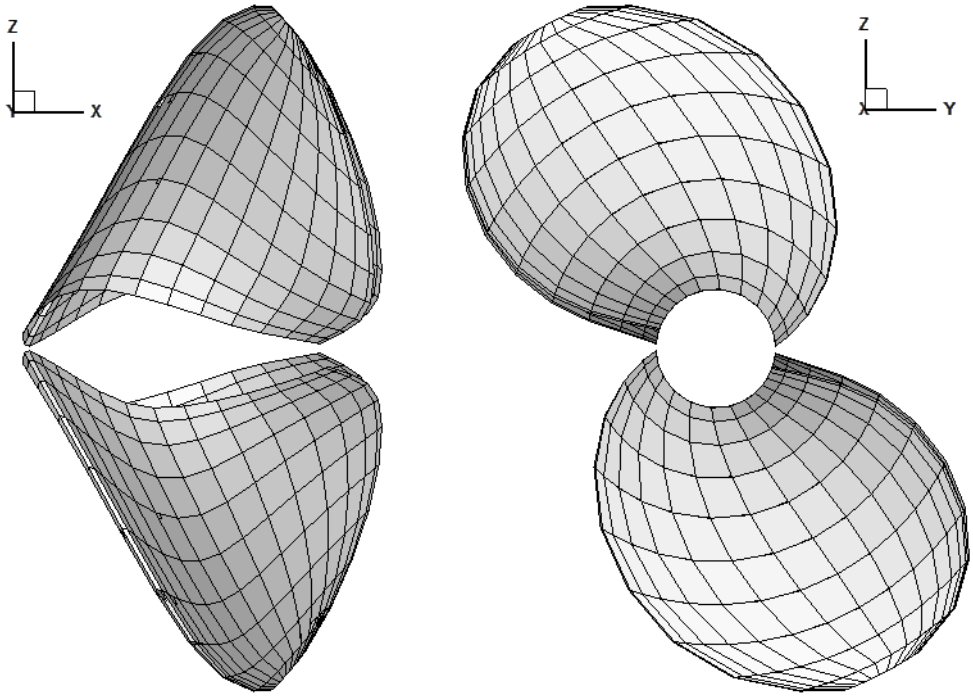

Fig. 3.20 Panel arrangements for original LTBP

3.5 Calculated Results

Fig. 3.21 shows the calculated results of propeller characteristics by Fluent and SQCM at different advance coefficients comparing with the experimental data. It is found that the calculated results of both methods are consistent with measured data. The Fluent results at design advance coefficient J=1.1 are better than SQCM results for thrust and torque coefficient. However, the propeller efficiency of calculation by using both methods was in very good agreement at design point.

Fig. 3.22 shows the contours of static pressure distribution (unit in Pa) on suction and pressure sides at J=1.1 which have been determined to the pressure coefficient, (C_P). The comparison of pressure coefficient distribution on the blade for r/R = 0.3 to 0.95 at J=1.1 between Fluent and SQCM are shown in Figs. 3.23 to 3.26 respectively. It is found that the calculated results of both methods were accorded.

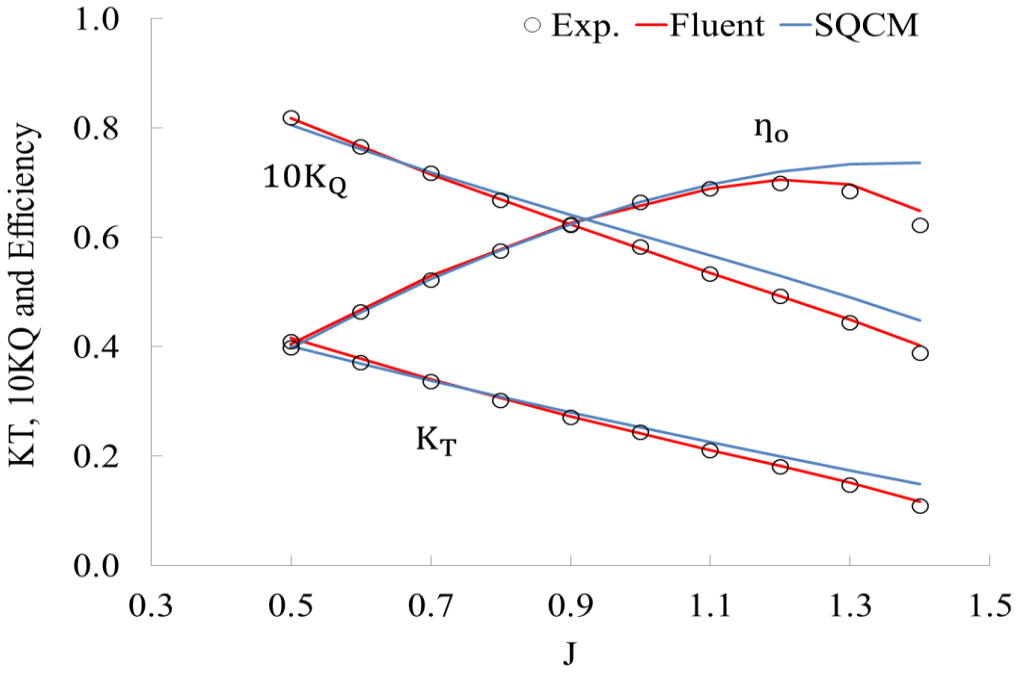

Fig. 3.21 Comparison of propeller characteristics (original LTBP)

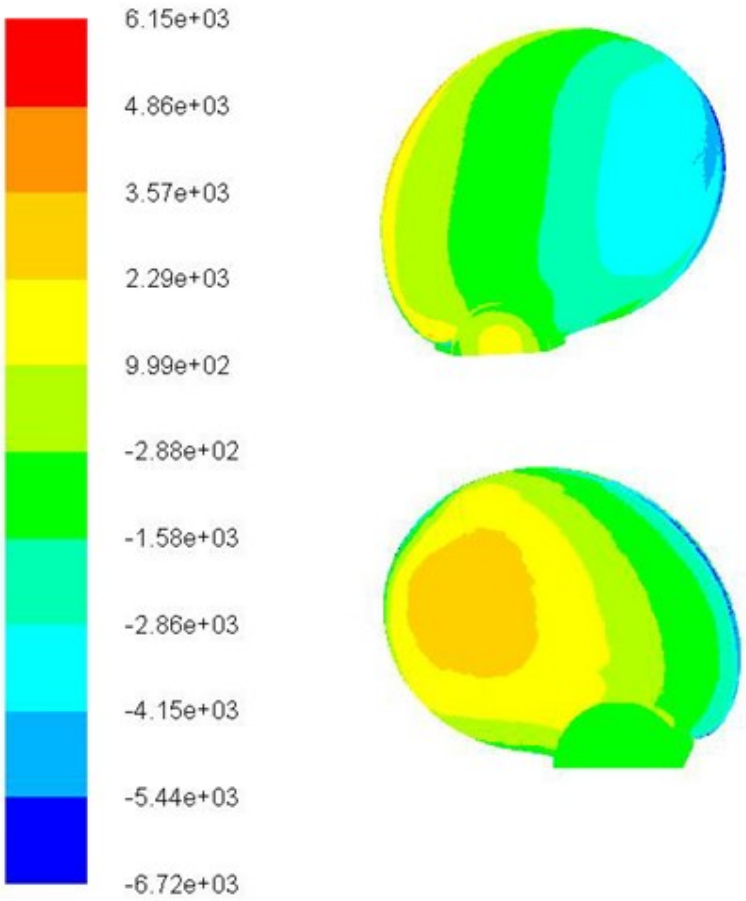

Fig. 3.22 Pressure distributions of original LTBP on suction side (upper) and pressure side (lower)

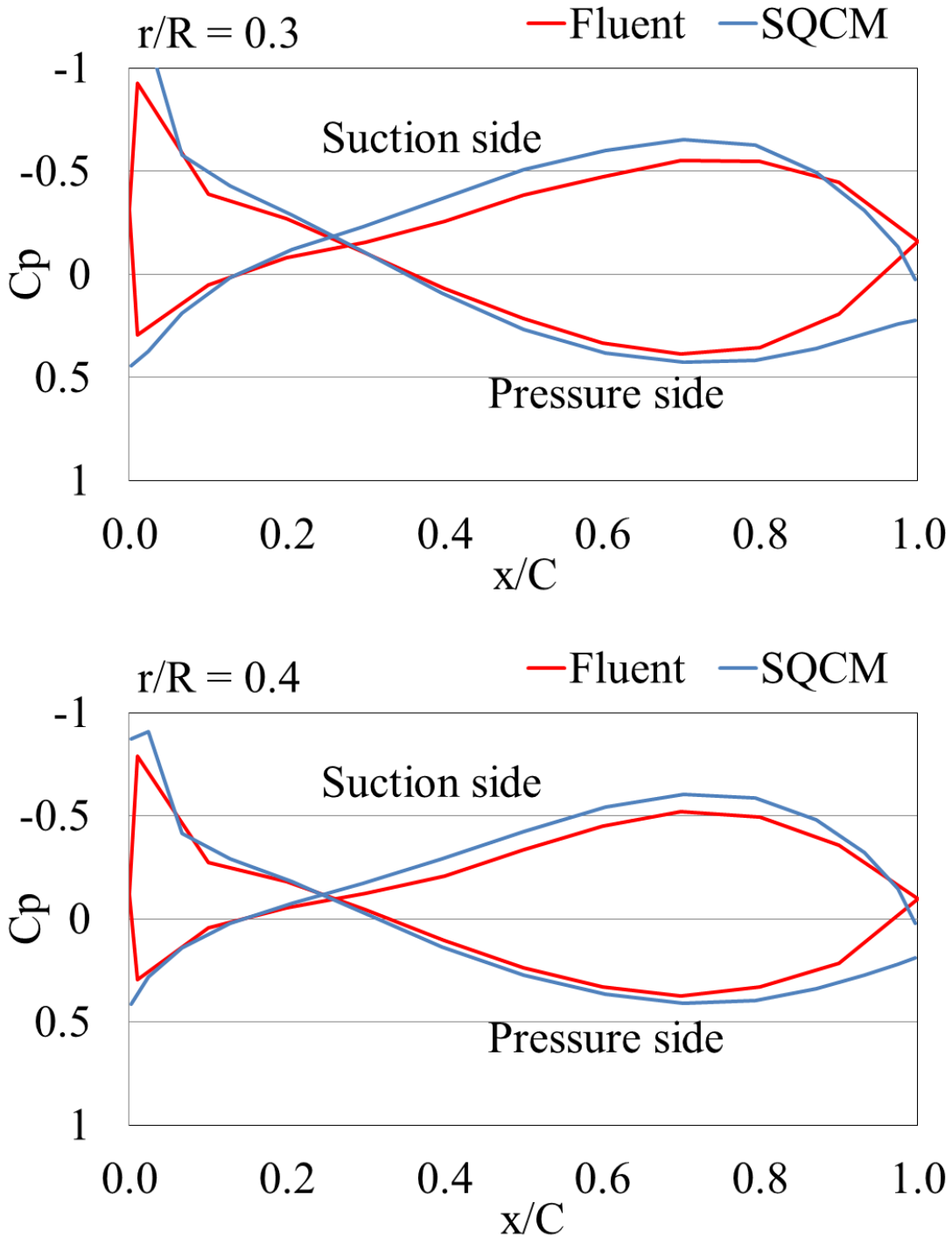

Fig. 3.23 Comparisons of pressure distributions between Fluent and SQCM (Original LTBP, r/R=0.3 and 0.4, J=1.1)

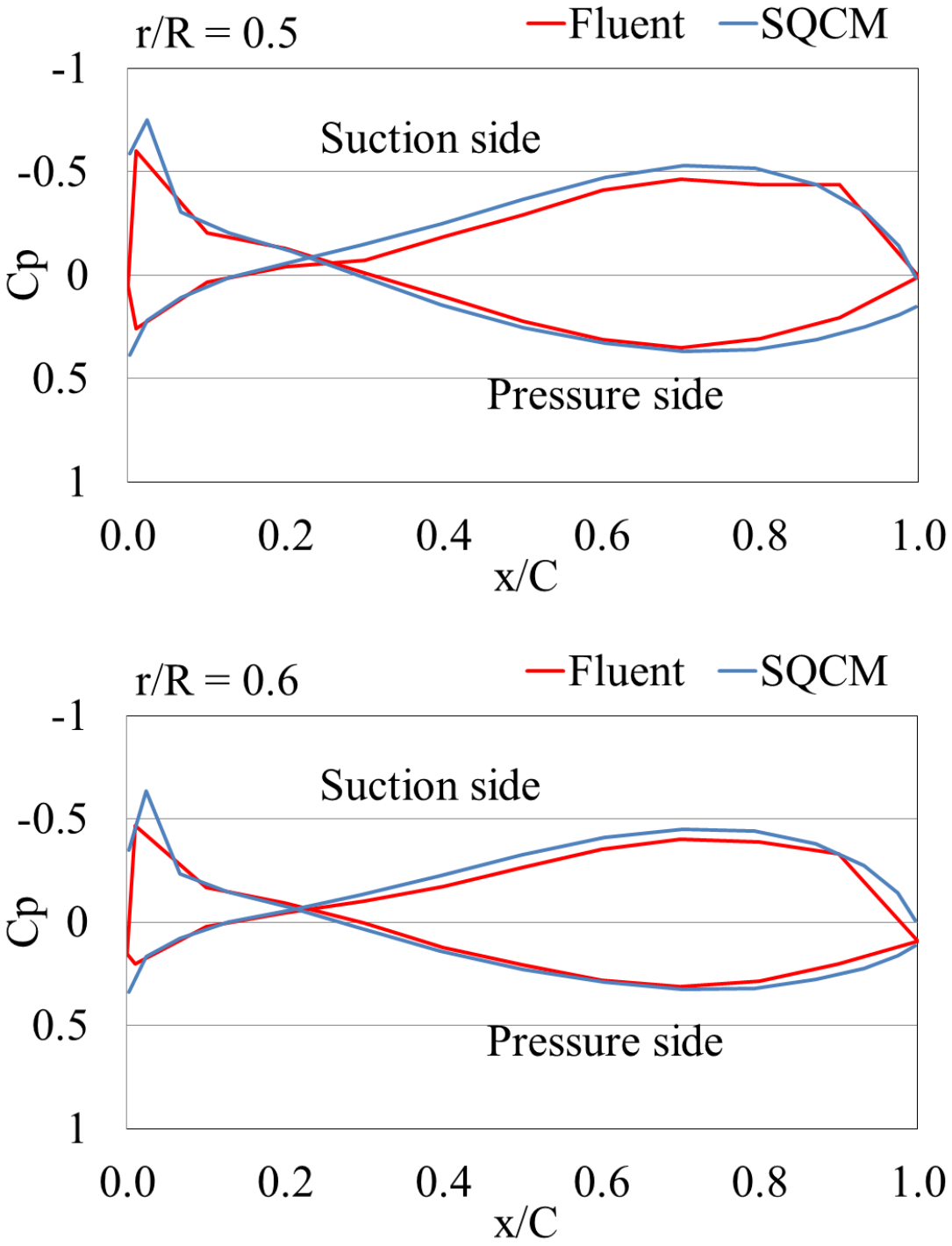

Fig. 3.24 Comparisons of pressure distributions between Fluent and SQCM (Original LTBP, r/R=0.5 and 0.6, J=1.1)

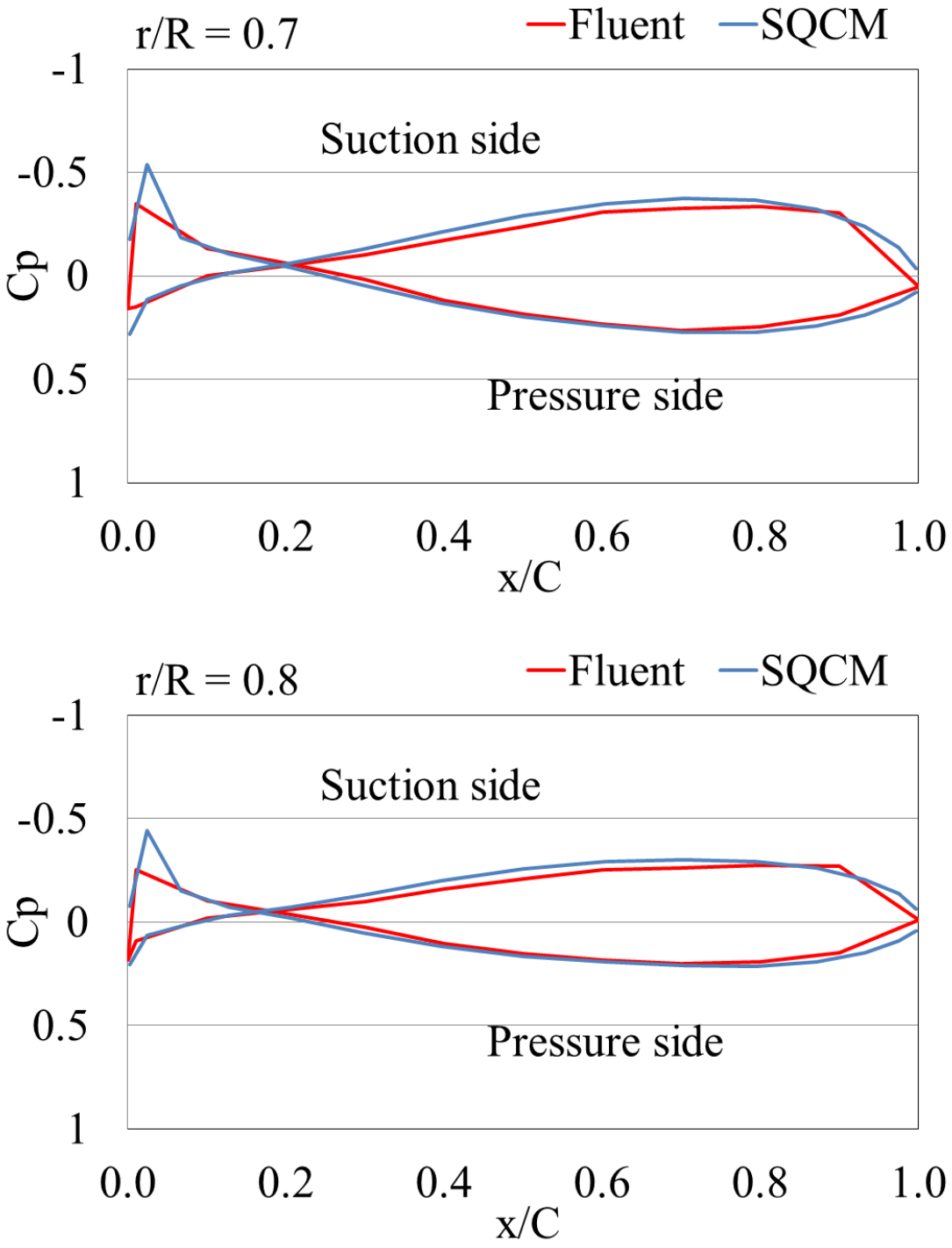

Fig. 3.25 Comparisons of pressure distributions between Fluent and SQCM (Original LTBP, r/R=0.7 and 0.8, J=1.1)

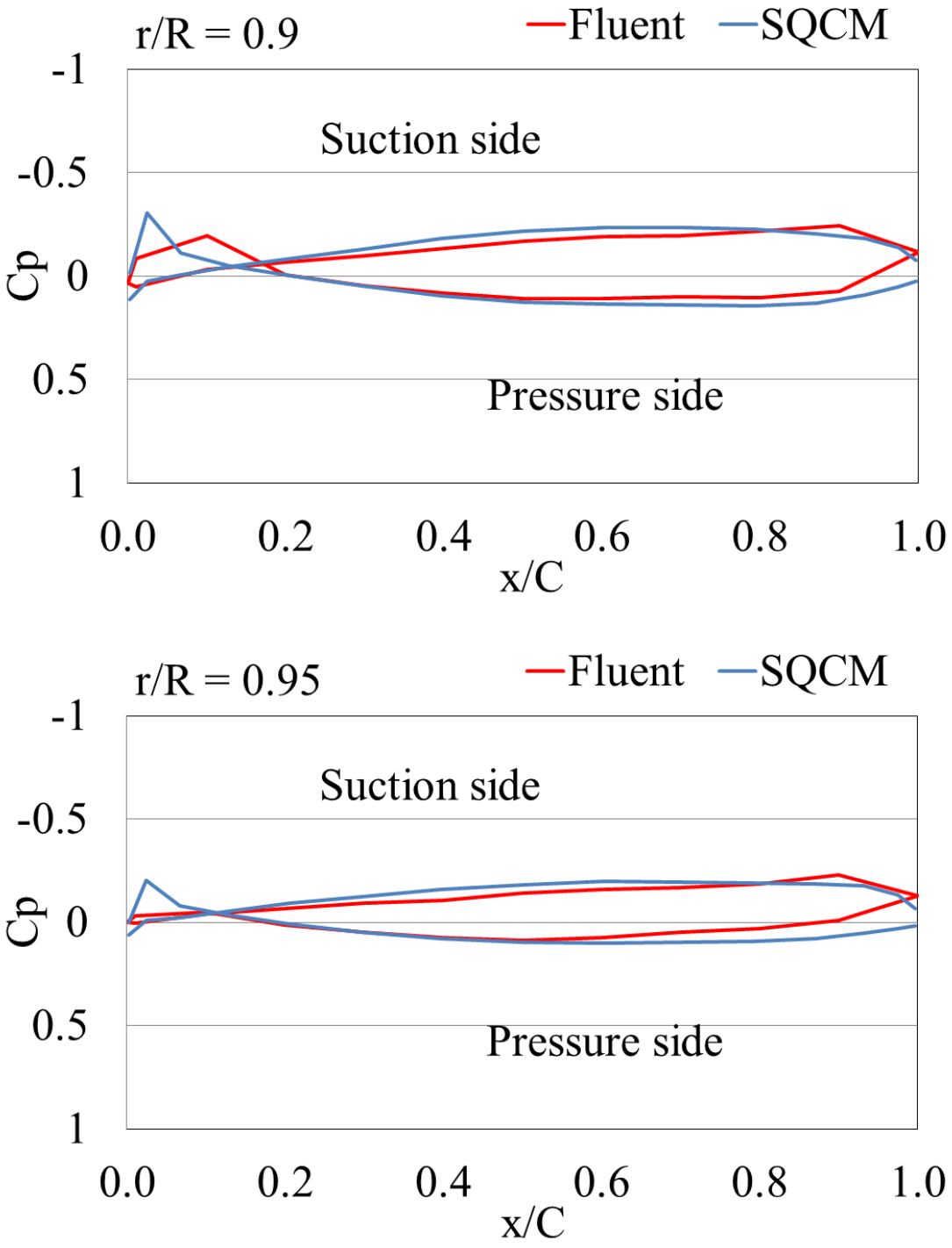

Fig. 3.26 Comparisons of pressure distributions between Fluent and SQCM (Original LTBP, r/R=0.9 and 0.95, J=1.1)

3.6 Conclusion

In this chapter, model test of the standard propeller of Long-Tail Boat from Bangkok in Thailand was conducted in straight shaft condition using the high speed circulating water channel at Kyushu University. The calculated characteristics by the presented CFD analysis system agree well with the experimental data in wide advance coefficient range. The propeller efficiency obtained by SQCM also agree well with the experimental data nearly design point.

Though the presented CFD analysis system is more accurate, SQCM is used for blade shape optimization in order to reduce computational time.

Chapter 4
Improvement of Long-Tail Boat Propeller Performance

4.1 Introduction

In this chapter, the optimization method of propeller blade shape by using real-coded genetic algorithm is described. Then the optimization of the Long-Tail Boat propeller in Chapter 3 adopted as an original propeller is conducted by the present optimization method and an improved propeller is obtained. Next, model test of the improved propeller is conducted in straight shaft condition by using the high speed circulating water channel at Kyushu University and the characteristics of the original and improved Long-Tail Boat propellers are compared with each other. Finally, the characteristics of those propellers in inclined shaft condition are evaluated by the present CFD analysis system.

4.2 Optimization Method of Propeller Blade Shape

4.2.1 Real-coded Genetic Algorithm

The genetic algorithm (GA) is a stochastic optimization technique inspired by the evolution process of natural life. In GA, selection is performed in the population of a certain generation so that an individual with high fitness to the objective function in the optimization problem survives with high probability. Furthermore, the population of the next generation is formed by crossover and mutation. As alternation of generations proceeds, the individuals with higher fitness increase, and the most suitable solution is provided. The above is a basic concept of GA. In general, an individual is expressed by binary string of 0 or 1 of the suitable number per one design variable in GA. And this binary string is transformed to the design variable which is a real number. The chromosome of each individual is expressed by

binary strings of the same number as the number of the design variables. Spaces expressed by binary strings and real numbers are called genotype and phenotype spaces, respectively. The mapping from phenotype to genotype is called coding. The GA with coding by binary string is called binary-coded GA. And binary-coded GA is applied to various problems. On the other hand, several GAs which use the real number directly to express an individual have been proposed. This kind of GA is called real-coded GA.

It has been reported that real-coded GA can surely find the optimum solution if the design variables are continuous in function optimization problems [57]. In the present study, the real-coded GA using Unimodal Normal Distribution CROSSover (UNDX) as a crossover operator is adopted. This GA was applied to the lens design problem, which is known as a difficult problem, and its usefulness was confirmed [58]. UNDX proposed by Ono et al. [57] is a kind of crossover operator in real-coded GAs. Each individual is defined by a real number vector and the dimension of the vector space is the same number as the number of design variables n_D. Two offspring vectors $\vec{C}_1,\ \vec{C}_2$ are generated by the normal distribution which is defined by three parents $\vec{P}_1, \vec{P}_2$ and $\vec{P}_3$ as shown in Fig. 4.1. One of the standard deviation values of the normal distribution, which corresponds to the principal axis connecting Parent 1 and Parent 2, is proportional to the distance between Parent 1 and Parent 2. The other is proportional to the distance of the third parent, Parent 3, from the principal axis connecting Parent 1 and Parent 2 and multiplied by $1/\sqrt{n_D}$. Offspring vectors are expressed by the following equations.

$$\begin{aligned} \vec{C}_1 &= \vec{M} + z_1\vec{e}_1 + \textstyle\sum_{k=2}^{n_D} z_k\vec{e}_k \\ \vec{C}_2 &= \vec{M} - z_1\vec{e}_1 - \textstyle\sum_{k=2}^{n_D} z_k\vec{e}_k \end{aligned} \tag{4.1}$$

Where

$$\vec{M} = \left(\vec{P}_1 + \vec{P}_2\right)/2$$

$$z_1 \sim N(0, \sigma_1^2),\ \ z_k \sim N(0, \sigma_2^2), (k = 2, \cdots, n_D)$$

$$\sigma_1 = \alpha d_1,\ \ \sigma_2 = \beta d_2/\sqrt{n_D}$$

$$\vec{e}_1 = \left(\vec{P}_1 - \vec{P}_2\right)/\left|\vec{P}_1 - \vec{P}_2\right|$$

$$\vec{e}_i \perp \vec{e}_j,\ \ (i \neq j),\ \ (i, j = 1, \cdots, n_D\ )$$

Here z_1 and z_k are normal random numbers. σ_1 and σ_2 are standard deviations. d_1 is the distance between Parent 1 and Parent 2, d_2 is the distance of the third parent, Parent 3, from the principal axis connecting Parent 1 and Parent 2. α and β are constants defined by parameter study and $\alpha = 0.5$ and $\beta = 0.35$ are recommended in the paper [57]. Vectors $\vec{e}_i (i = 2, \cdots, n_D)$ are the orthogonal basis vectors spanning the subspace perpendicular to vector $\vec{e}_1$.

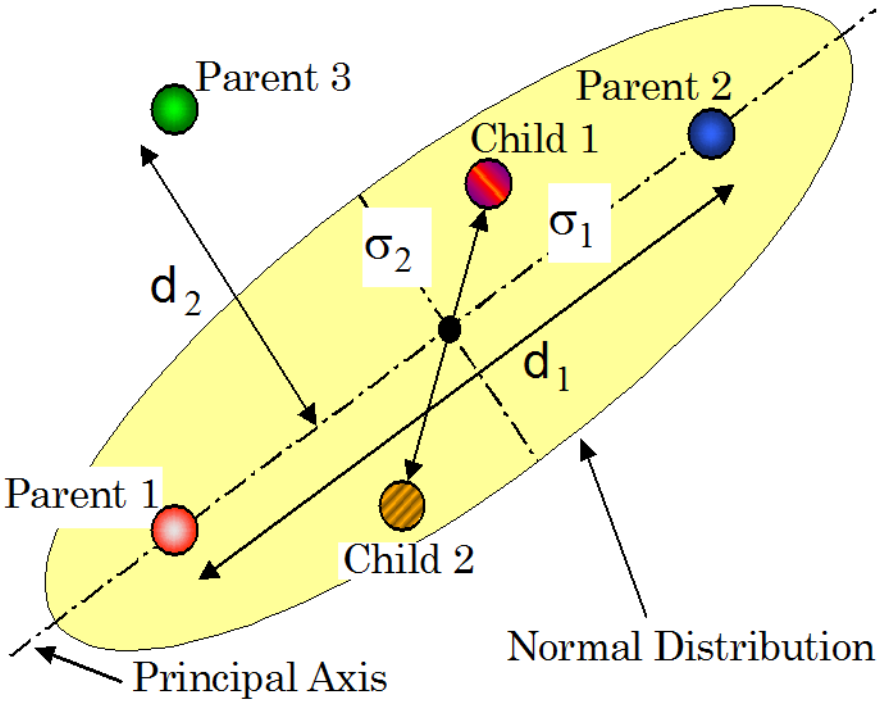

Fig. 4.1 Concept of UNDX

4.2.2 Definition of Optimization Problem

(1) Design Variables

In the present method, the improved propeller has the same chord, skew and maximum blade thickness distributions in the radial direction as the original propeller shown in Chapter 3. The number of the blade is also the same. Nondimensionalized thickness and camber distributions by their maximum values in the chord-wise direction are the same ones of the original propeller in each radial section.

Pitch, maximum camber and rake distributions in the radial direction are selected as the design variables. The design variables of pitch in the radial direction are set at the root, midpoint and tip of the propeller and the distribution is approximated by parabolic function. The design variables of maximum camber in the radial direction are set at the root, 30 % and 80 % radial positions and tip of the propeller and the distribution is approximated by cubic function. The design variable of rake in the radial direction is set at the midpoint and the original values are used at the root and tip. Rake distribution is approximated by parabolic function.

(2) Objective Function

Optimization is conducted to maximize the propeller efficiency η_O keeping the target thrust coefficient K_T^{Target}. The objective function F is expressed by the following equation with the penalty function P.

$$F = P \times \eta_O \tag{4.2}$$

Where

$$P = \exp\left(-\left|K_T - K_T^{\text{Target}}\right| / K_T^{\text{Target}}\right)$$

(3) Constraint Condition

The constraint condition is that the minimum pressure coefficients outer than 80% radial section should not be lower than those of the original propeller.

(4) Procedure of Optimization

In GA, it is very important to use a generation-alternation model which can avoid the early convergence and suppress the evolutionary stagnation. In the present study, Minimal Generation Gap (MGG) model proposed by Satoh et al. [59] is adopted.

The procedure of optimization for improving the propeller efficiency described as follows (See Fig. 4.2):

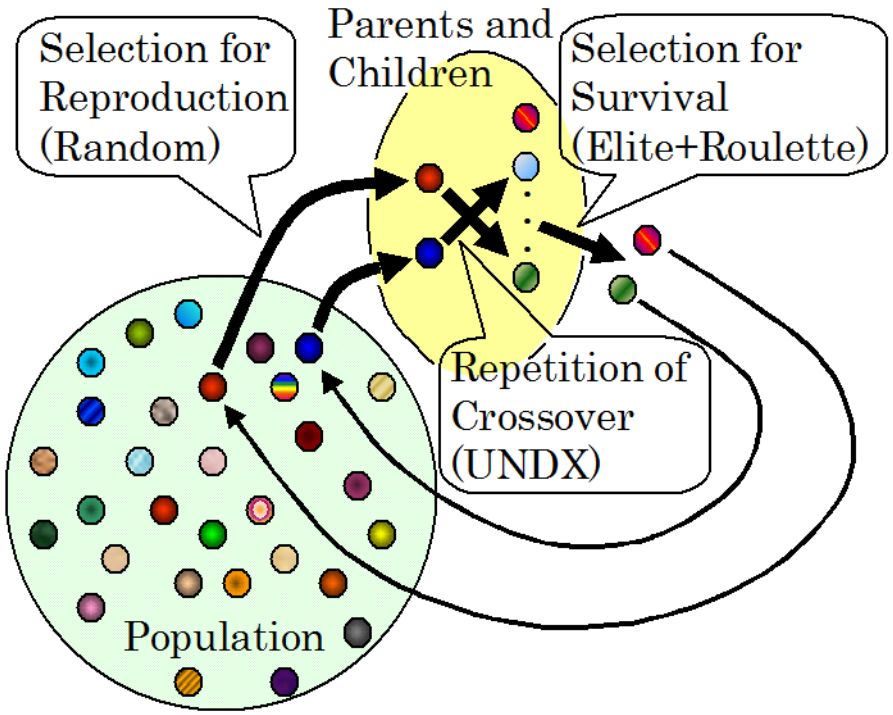

Fig. 4.2 MGG model

(Step 1) Generation of initial population

Obtain the pitch, maximum camber and rake distributions in the radial direction by generating the design variables randomly. Make the propeller geometric data by considering chord, skew and maximum blade thickness distributions in the radial direction of the original propeller. Thickness and camber distributions in the chord-wise direction of the original propeller in each radial section are also considered here.

Calculate the propeller characteristics in straight shaft condition by using SQCM and compare the minimum pressure coefficients near the propeller tip mentioned above. If the constraint condition about the minimum pressure coefficients is satisfied, the propeller is permitted to join the initial population.

Repeat the above procedure until the number of the individuals (propellers) which satisfy the constraint conditions becomes N_P.

(Step 2) Selection for reproduction

Select a pair of parents from the current population randomly.

(Step 3) Generation of offspring

Generate two children by applying UNDX to the selected pair of parents at **Step 2**. Compare the minimum pressure coefficients near the propeller tip. If the constraint condition about the minimum pressure coefficients is satisfied, the propeller is selected as an object of evaluation at the next step. Memorize the propeller characteristics.

Repeat the above procedure until the number of the offspring which satisfy the constraint conditions becomes $2 \times N_C$.

(Step 4) Selection for survival

Select two individuals from the pair of parents selected at **Step 2** and $2 \times N_C$ offspring generated at **Step 3**; one is the best individual and the other is selected from $2 \times N_C + 1$ individuals other than the best one by the rank-based roulette wheel selection. Replace the parents selected at **Step 2** in the population with these two individuals.

Repeat the above procedure from **Step 2** to **Step 4** until a certain condition is satisfied.

4.3 Characteristics of Improved Long-Tail Boat Propeller

This section describes CFD calculation of improved model propeller for LTBP. The improved LTBP simulations were conducted for steady-state flow with straight shaft condition in uniform inflow. The numerical results are compared with the experimental data.

4.3.1 Geometry of Improved Propeller

The propeller characteristics of original model in Chapter 3 have been optimized into improved propeller for increasing propeller efficiency. It was optimized by using Genetic Algorithm (GA) in the previous section. The diameter, chord length, skew and maximum thickness were fixed to those of original model. The pitch, camber and rake distributions were optimized in order to maximize the propeller efficiency. Figs. 4.3 to 4.5 show pitch, maximum camber and rake distributions at each radius on the blade for original and improved propellers. The comparison of blade section geometry between original and improved models at r/R = 0.2 to 0.975 are shown in Figs. 4.6 and 4.7 respectively.

Fig. 4.8 shows the model of the improved LTBP. The model test of the improved LTBP was conducted by using the high speed circulating water channel at Kyushu University. The propeller rotational speed was fixed 10 rps as same to original model.

Fig. 4.9 shows the history of the objective function defined as Eq. (4.2). Fig. 4.10 shows the history of thrust coefficient. The history of increasing propeller efficiency versus number of evaluation is shown in Fig. 4.11.

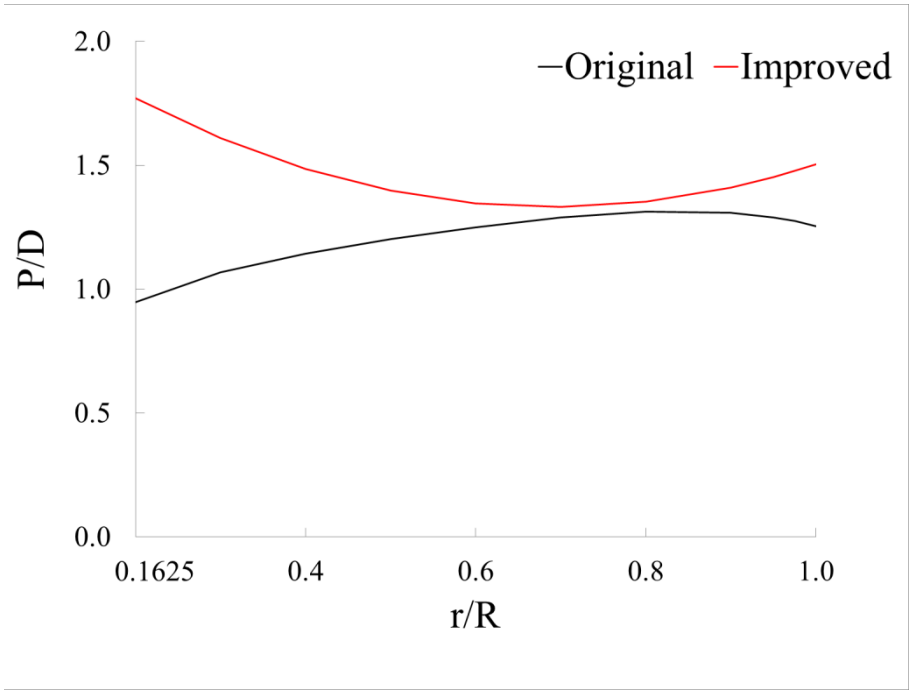

Fig. 4.3 Pitch distributions of original and improved LTBPs

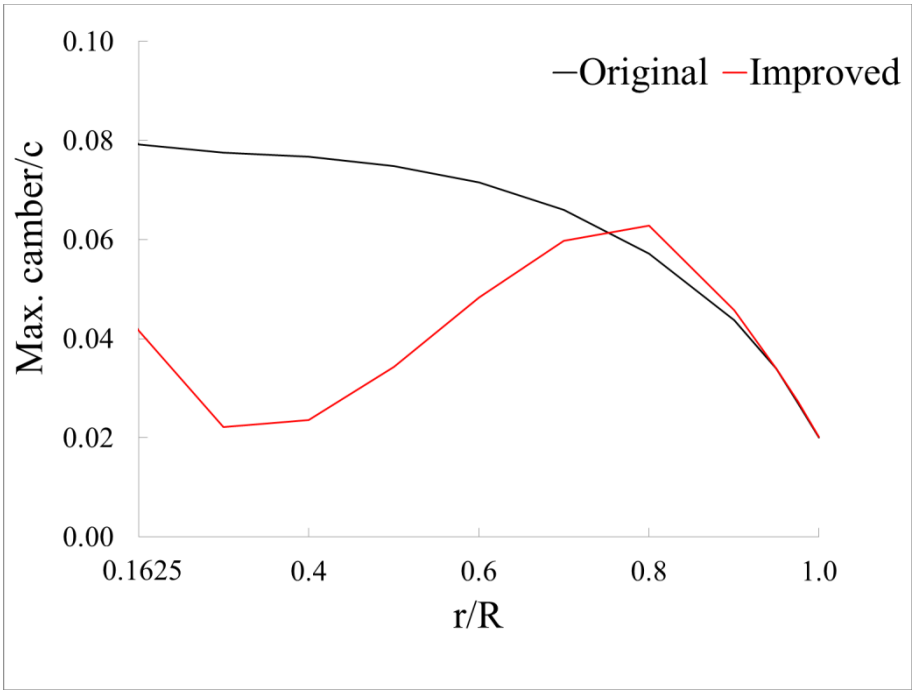

Fig. 4.4 Maximum camber distributions of original and improved LTBPs

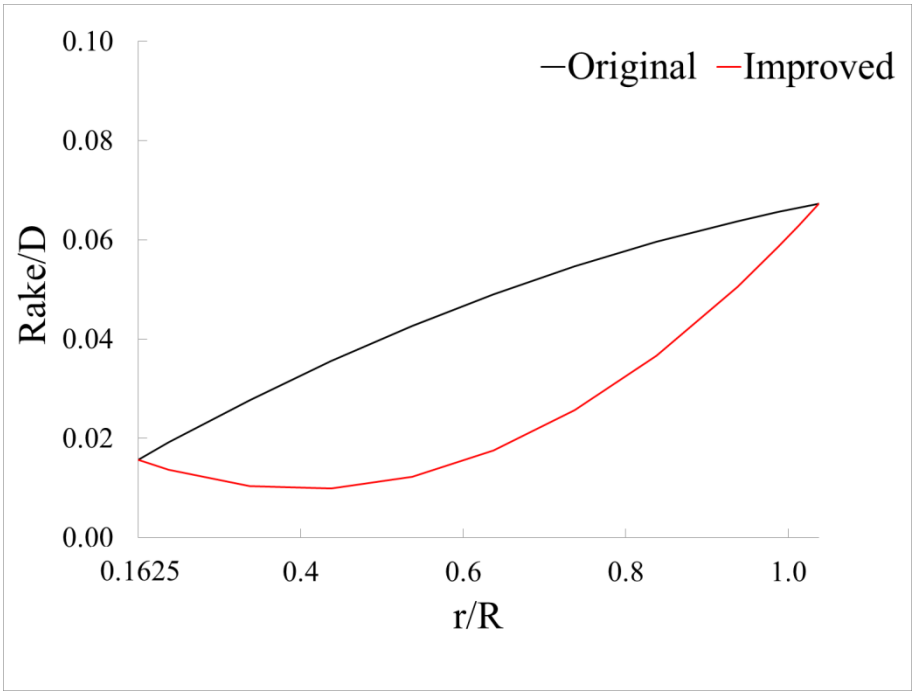

Fig. 4.5 Rake distributions of original and improved LTBPs

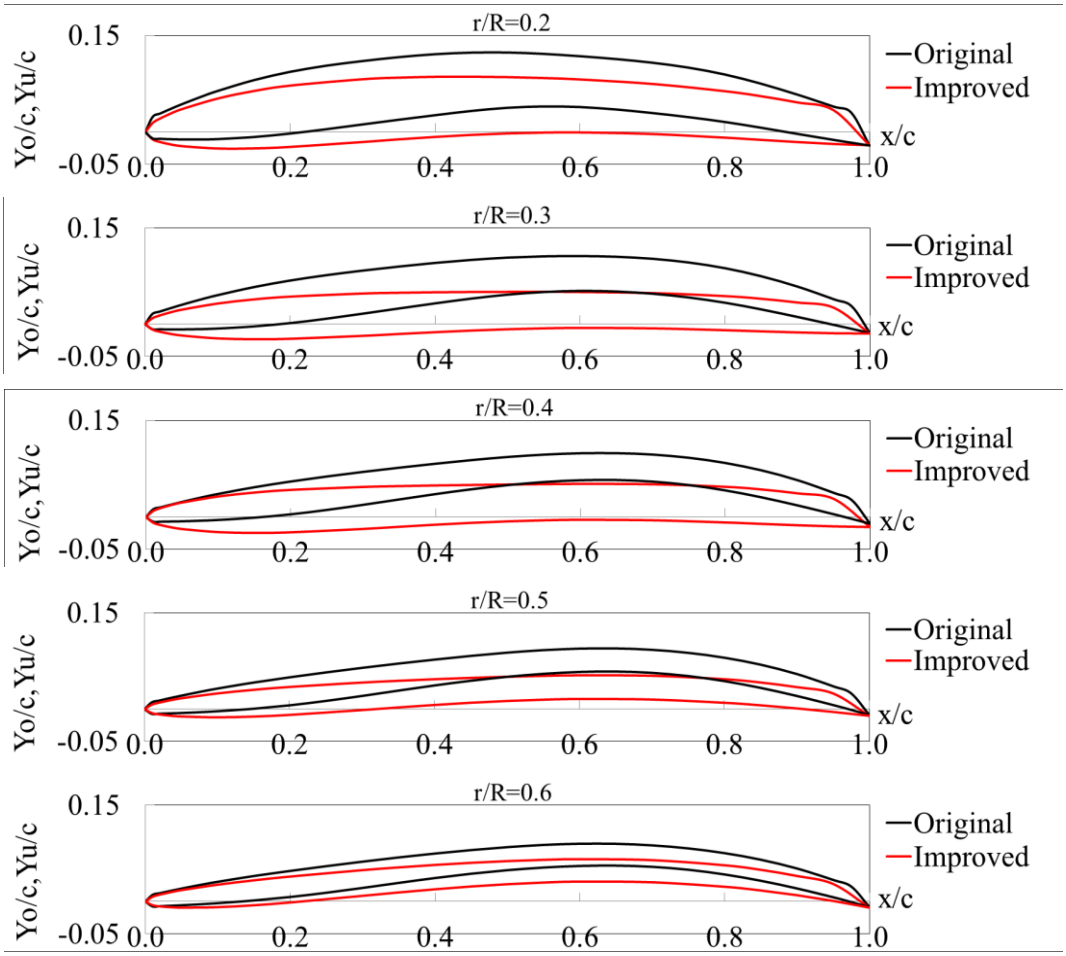

Fig. 4.6 Blade sections of original and improved propellers (r/R = 0.2, 0.3, 0.4, 0.5 and 0.6)

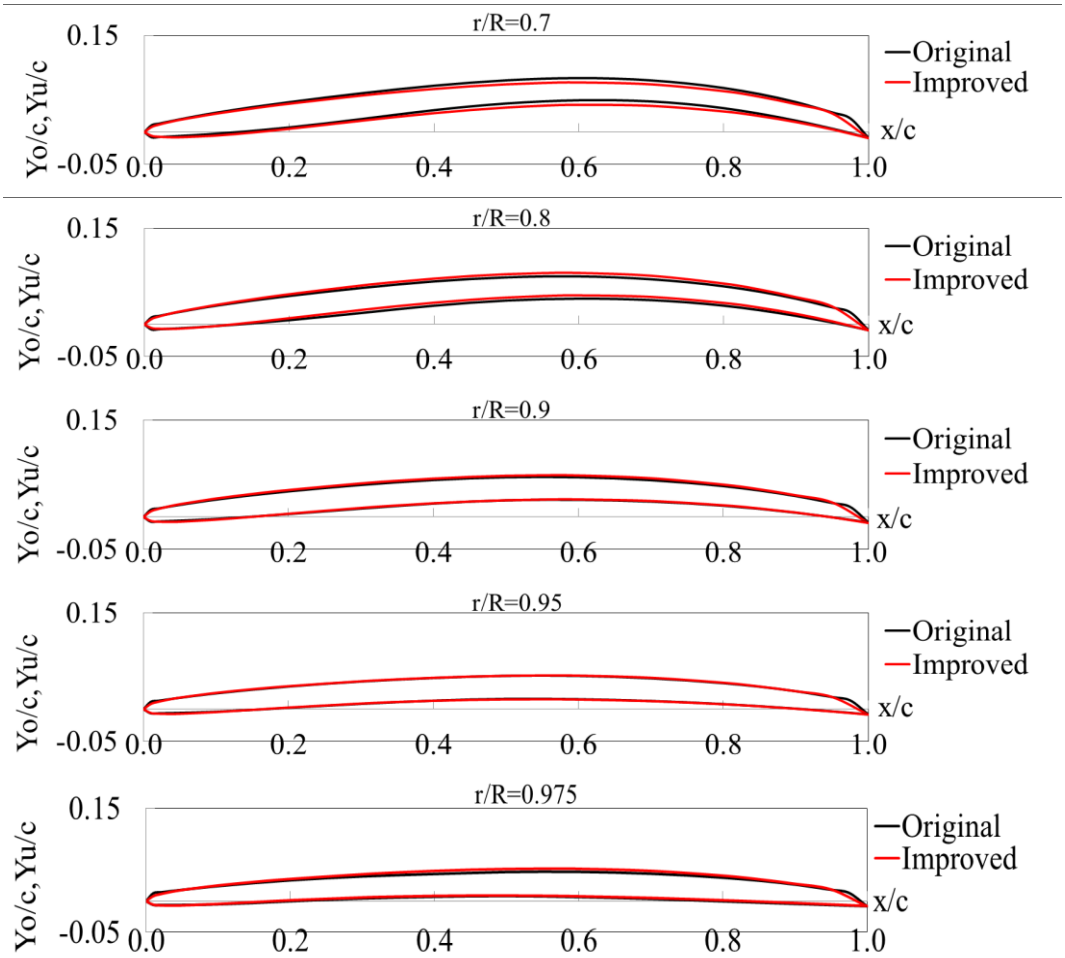

Fig. 4.7 Blade sections of original and improved propellers (r/R = 0.7, 0.8, 0.9, 0.95 and 0.975)

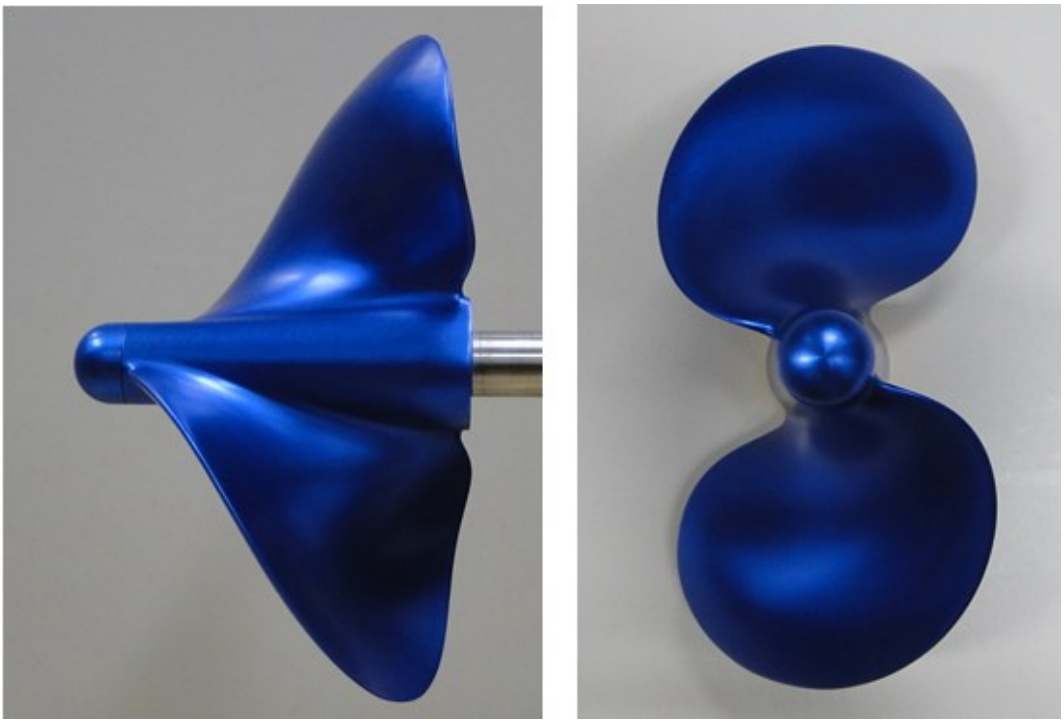

Fig. 4.8 Model of improved LTBP at side view (left) and front view (right)

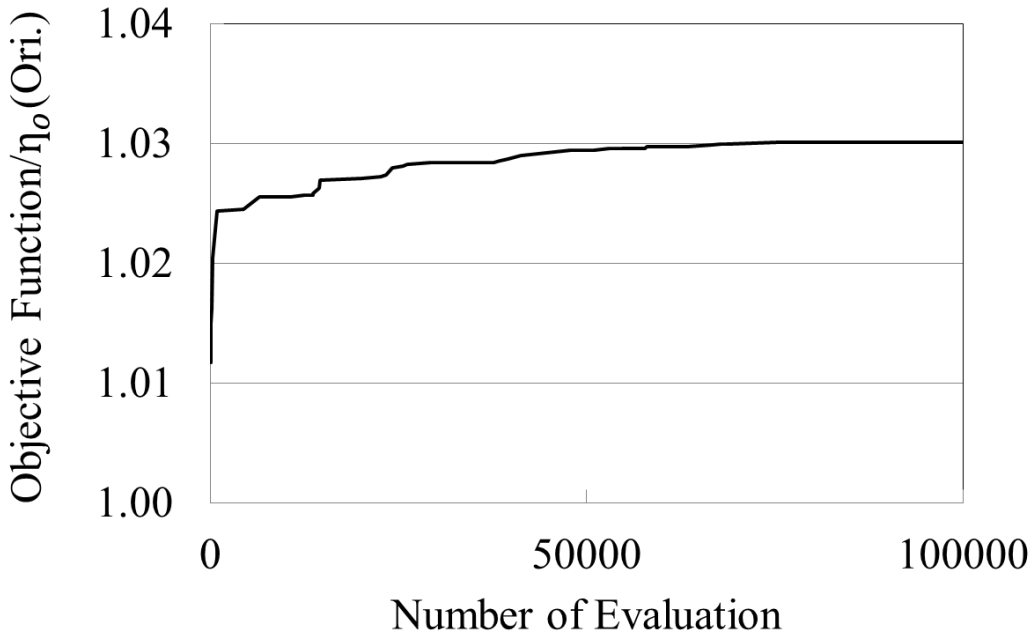

Fig. 4.9 History of objective function

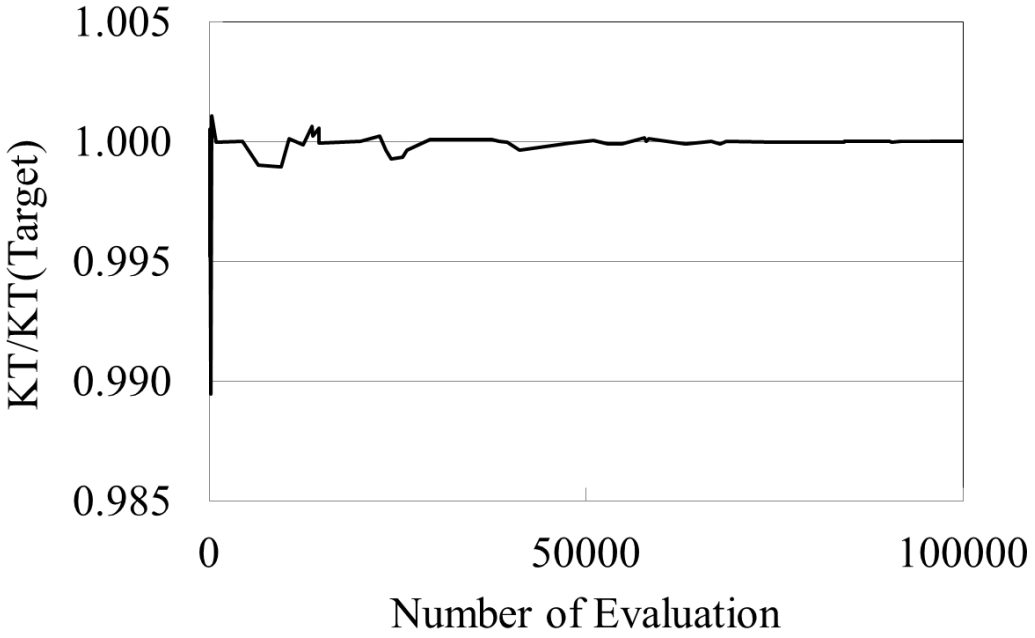

Fig. 4.10 History of thrust coefficient

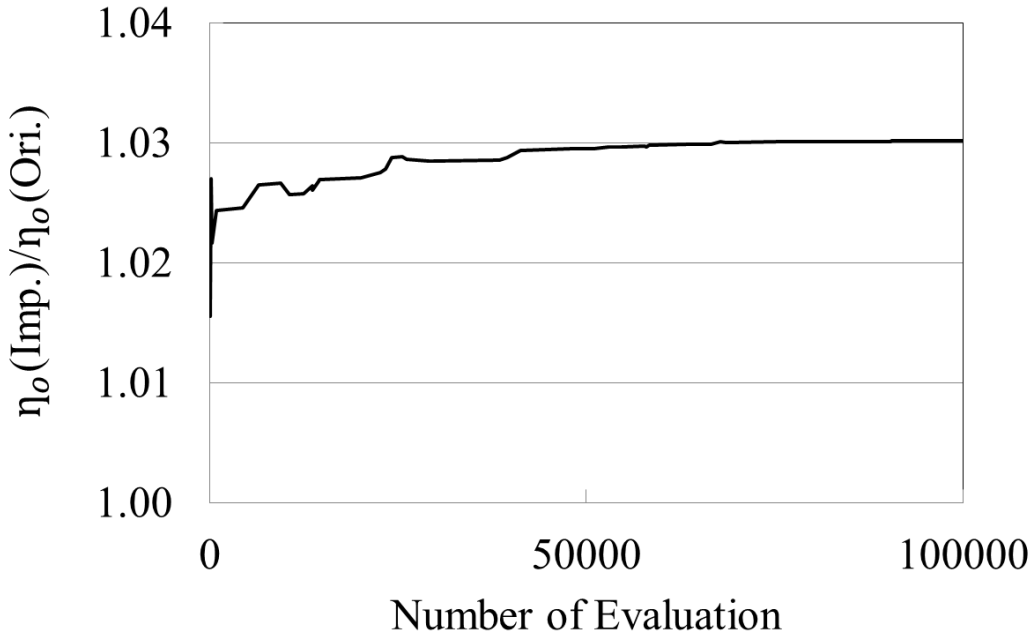

Fig. 4.11 History of propeller efficiency

4.3.2 Computational Domain and Meshing

The computational domain sizes and boundary condition are the same as those for the original LTBP. The surface mesh in rotational domain including blade and hub were generated with hybrid unstructured mesh as shown in Fig. 4.12. Fig. 4.13 shows the surface mesh on the propeller blade. The grid independence was determined about 1.6 million cells for total grids which are divided into rotating part and stationary part with containing about 1 million and 0.6 million cells respectively (kept to be the same as the original model). About 15 prismatic layers were defined around blade and hub. Fig. 4.14 shows the prismatic layers and mesh beside the blade and hub.

The average values of y^+ on the solid surfaces (blade and hub) were found to be 25. Fig. 4.15 shows the panel arrangement in SQCM. Each blade was divided into 10 panels in the radial direction and 15 panels in the chord-wise direction.

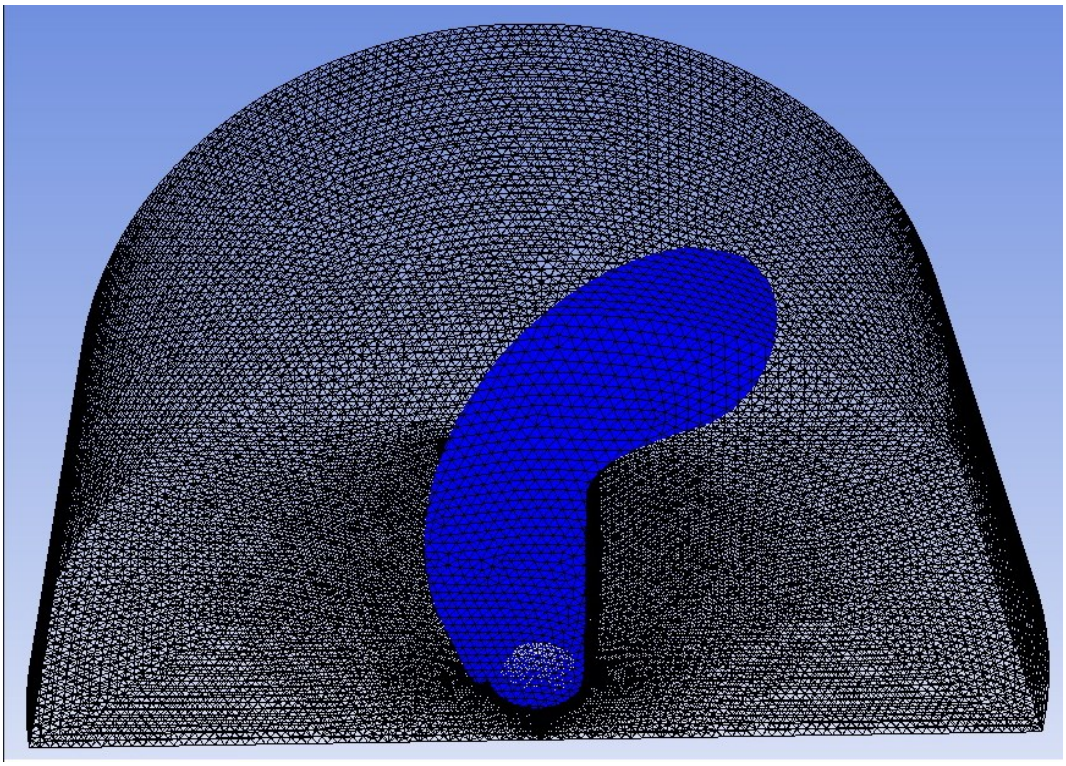

Fig. 4.12 Mesh in rotational domain for improved LTBP

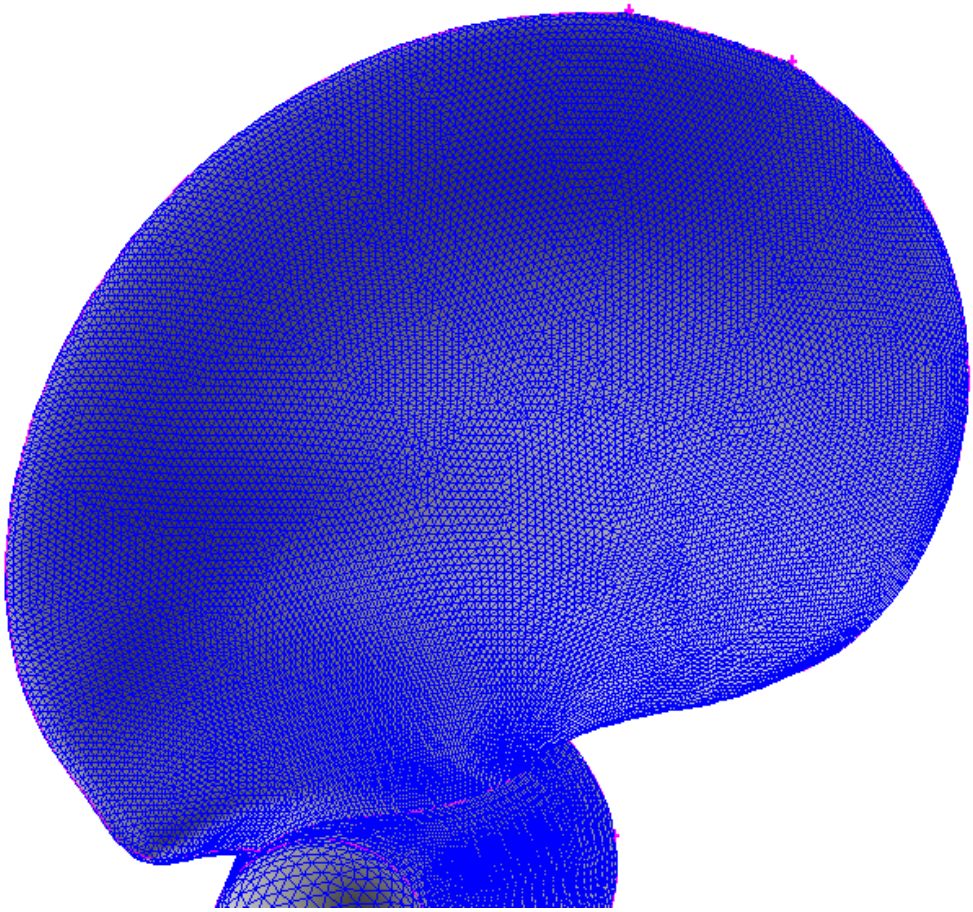

Fig. 4.13 Surface mesh on the blade for improved LTBP

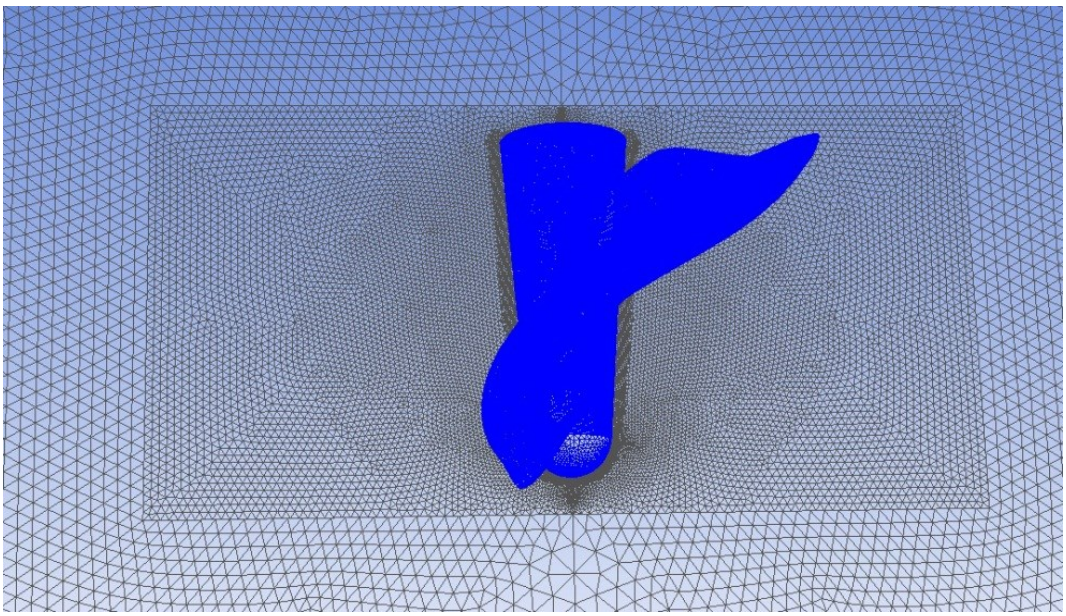

Fig. 4.14 Prismatic cells and mesh beside hub for improved LTBP

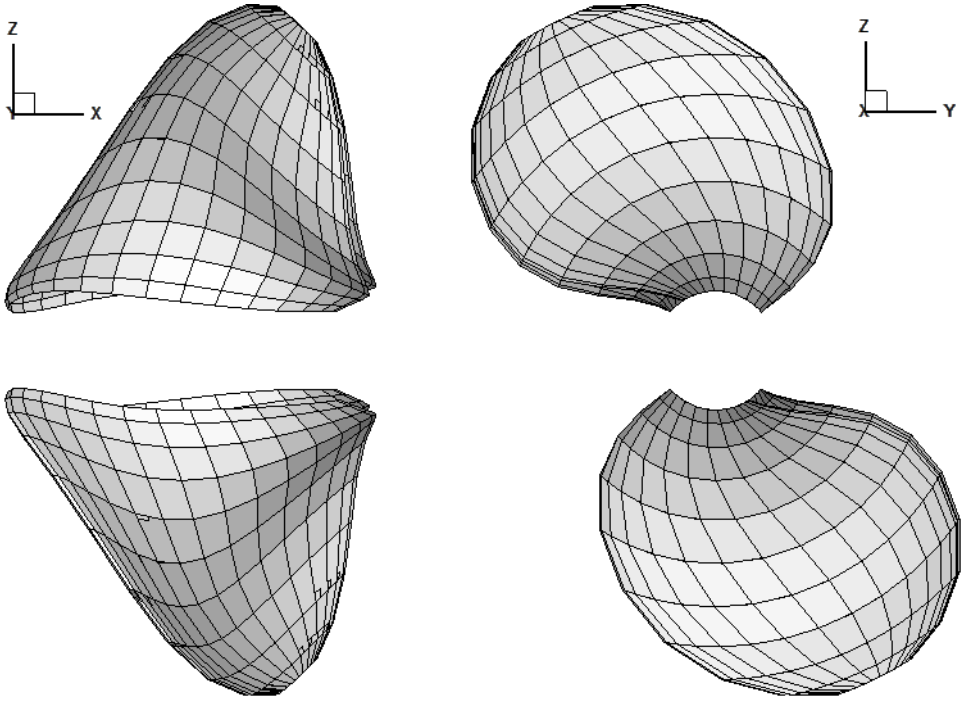

Fig. 4.15 Panel arrangements for improved LTBP

4.3.3 Optimization Results

The comparison of thrust and torque coefficients of original and improved LTBP models in the experiment is demonstrated in Fig. 4.16. It is found that thrust coefficient of improved model was seen little increasing at J=1.1-1.4 but it was seen that equally original at J=0.5-1.0. Torque coefficient of improved model was seen slightly more than original at J=0.5-1.1 but it was seen that as same as original at J=1.2-1.4. Fig. 4.17 shows the propeller efficiency of original model comparing with improved model. It is found that the propeller efficiency of improved model are increased at J=1.1 (design point). The propeller efficiency of improved model are more increased over J=1.1.

Fig. 4.18 illustrates the comparison of propeller performances for thrust and torque coefficients between original and improved model with Fluent and SQCM results. It is found that thrust and torque coefficients of improved model with Fluent were seen slightly increasing from original including at design point. SQCM result for thrust coefficient was kept same original but the torque coefficient was deteriorated slightly at design point. However, Fluent and SQCM results are seen equally at the design point. The propeller efficiency of the improved model was increased at design point for both methods and same tendency which is shown in Fig. 4.19

The propeller performances of calculation results with both methods for original and improved models were compared to measured data as shown in Figs. 4.20 and 4.21 respectively. It was demonstrated that calculation results with Fluent of original model were very good for the thrust, torque coefficients and propeller efficiency at each advance coefficient. Accuracy of the Fluent results is better more than SQCM in higher advance coefficient for the original propeller. The accorded of thrust coefficient for improved model between calculations with both methods and measured data. Torque coefficient of improved model for calculation with Fluent was overestimated around the lower advance coefficient but it was lower estimated around the lower advance coefficient for SQCM.

However, at J=1.1 (design point), thrust and torque coefficient of both methods are considered to agree with the measured data. Moreover, in terms of propeller efficiency of improved model, it is found that the results from calculation with both methods agree well with the experimental data.

Fig. 4.22 shows the comparison of propeller efficiency versus K_T / J^2 for experiments and calculations with both methods between the original and improved model. In order that to confirm the increment of propeller efficiency of improved model. It is found that the propeller efficiencies of improved model at design point calculated by using Fluent and SQCM are similar but they are slightly larger than experimental result. Fig. 4.23 shows the increasing propeller efficiency ratio of improved model for experiment and calculation. It is found that the propeller efficiency of improved model at K_T/J^2 = 0.174 (design point), measured data in open-water test was increased approximately 3.3 %. The calculation results of improved model were increased approximately 4.0 % and 3.2 % from Fluent and SQCM respectively.

Fig. 4.24 shows the contours of static pressure distribution (unit in Pa) on suction and pressure sides at J=1.1 (design point) for improved model which have been transformed to pressure coefficient. Figs. 4.25 to 4.28 show the comparison of pressure coefficient distribution at the design point between Fluent and SQCM for improved model at r/R = 0.3 to 0.95 respectively. It is found that the results of both methods are in good agreement.

Fig. 4.29 to Fig. 4.32 show the comparison of pressure coefficient distribution at design point for r/R =0.3 to 0.95 between the original and improved propellers with Fluent. It is found that the pressure at suction side in x/C = 0.4 to 1.0 for r/R = 0.3 to 0.8 of improved model are increased more over than original model. The pressure at pressure side in x/C = 0.4 to 1.0 for r/R = 0.3 to 0.6 of improved model are decreased from the original model.

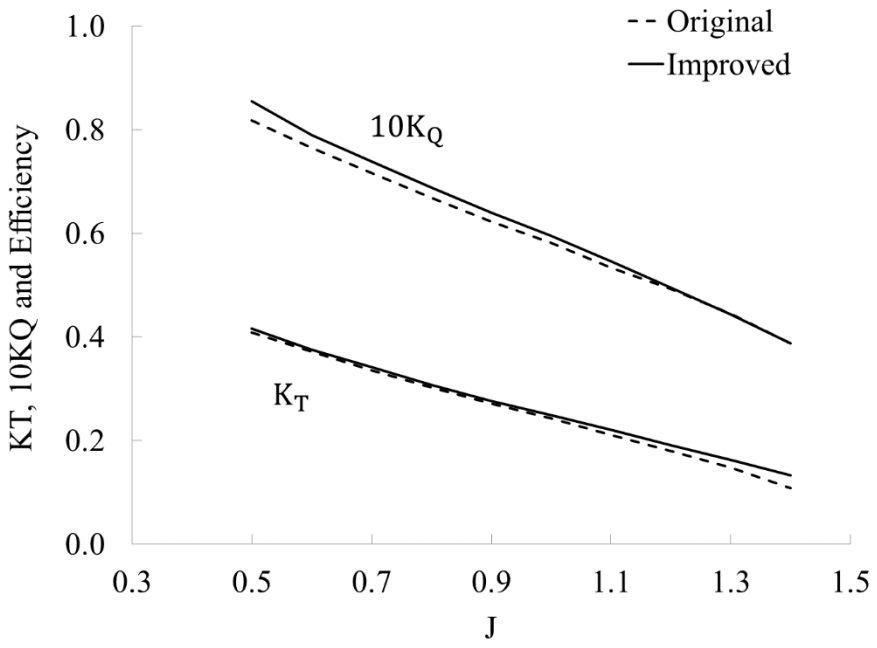

Fig. 4.16 Comparison of thrust and torque coefficient in experiment

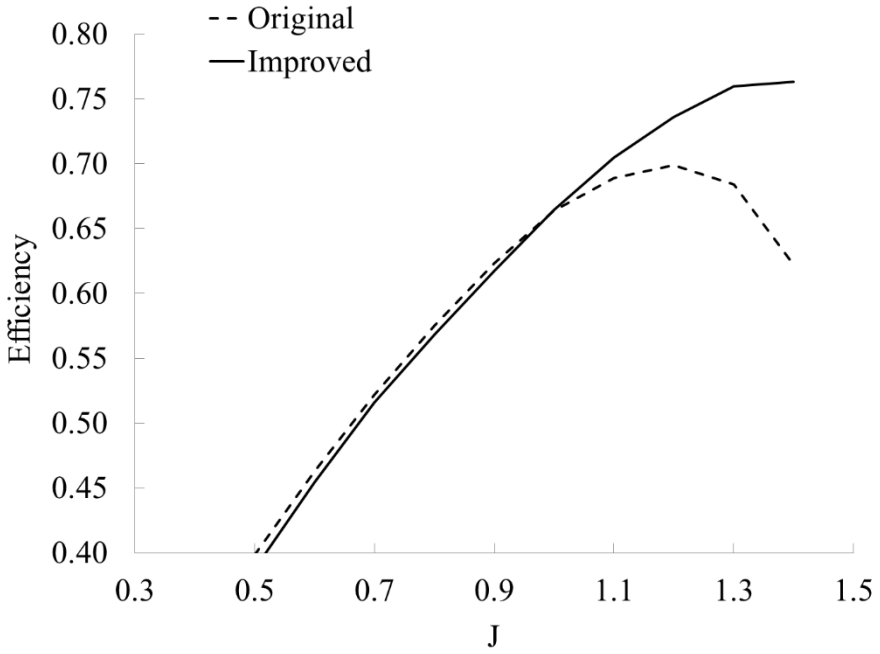

Fig. 4.17 Comparison of propeller efficiency in experiment

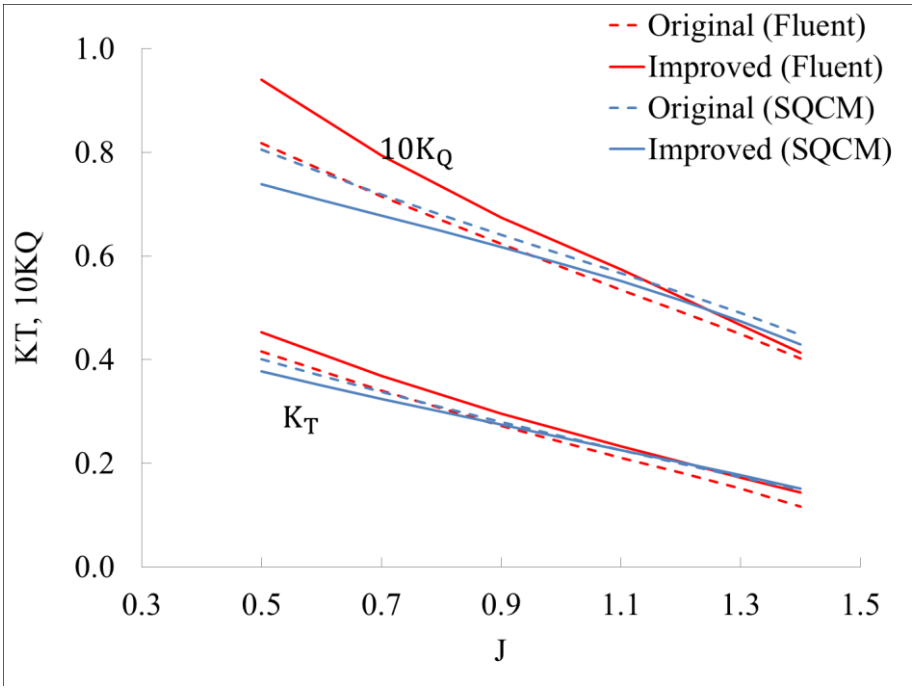

Fig. 4.18 Comparison of thrust and torque coefficient in calculation

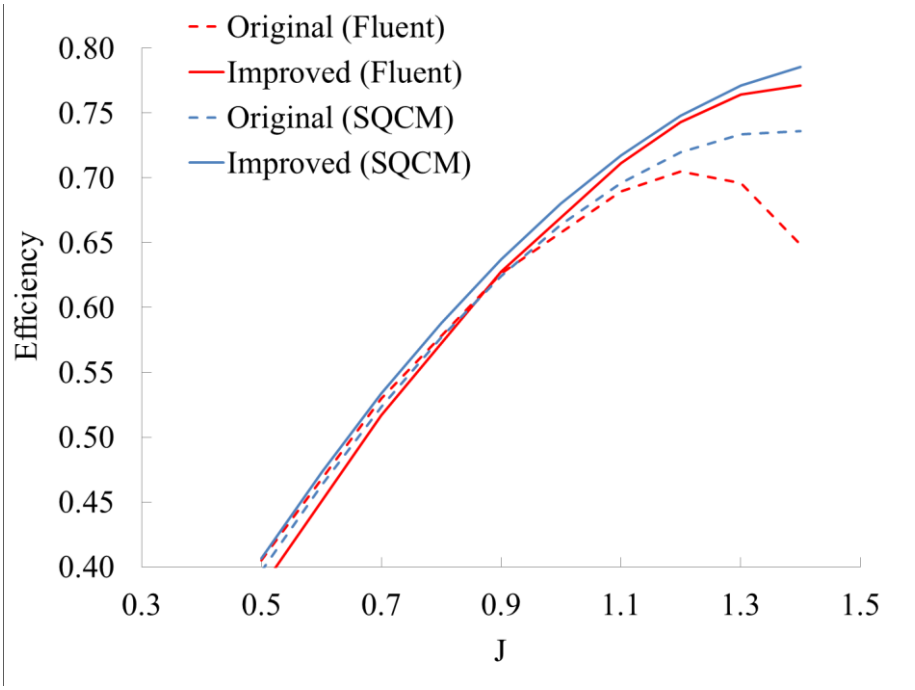

Fig. 4.19 Comparison of propeller efficiency in calculation

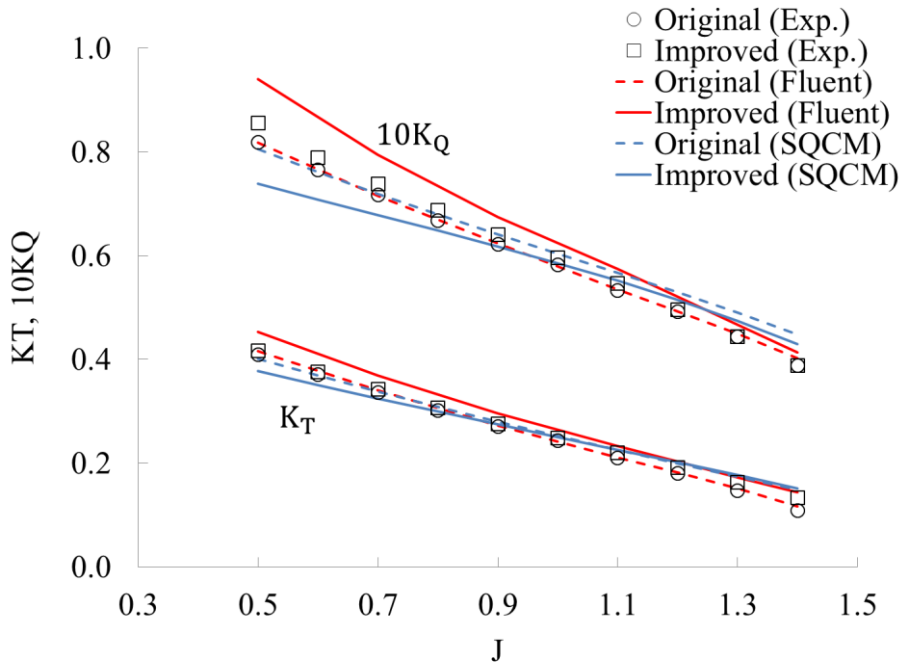

Fig. 4.20 Comparison of thrust and torque coefficient in experiment and calculation

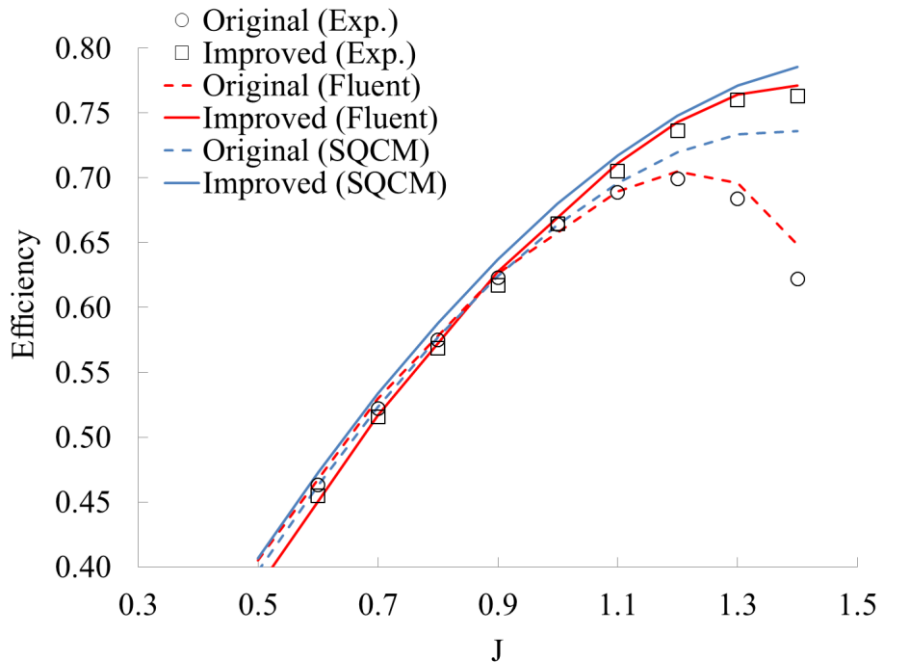

Fig. 4.21 Comparison of propeller efficiency in experiment and calculation

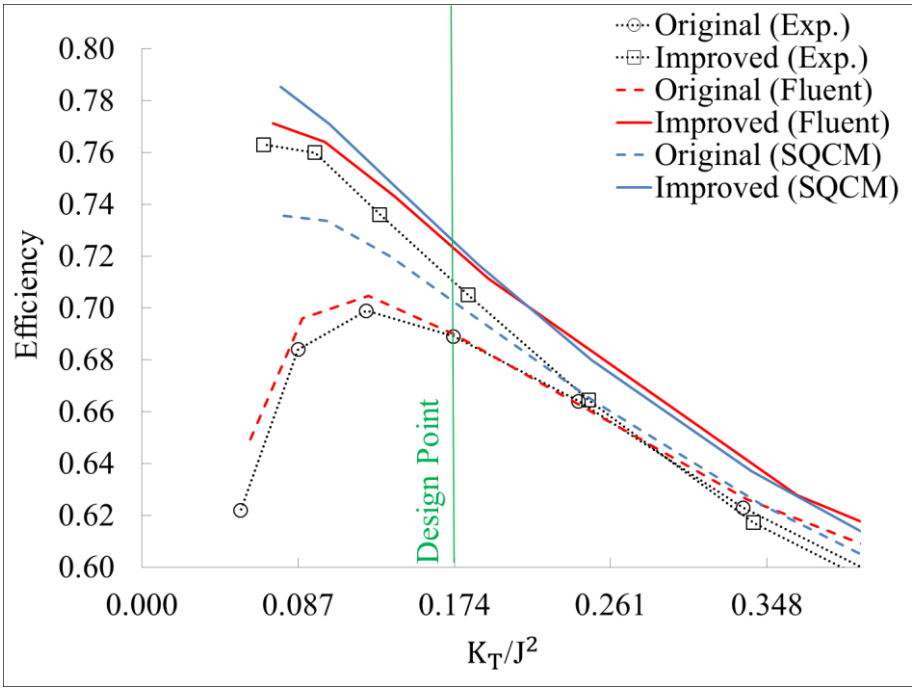

Fig. 4.22 Comparison of propeller efficiency versus K_T/J^2 in experiment and calculation

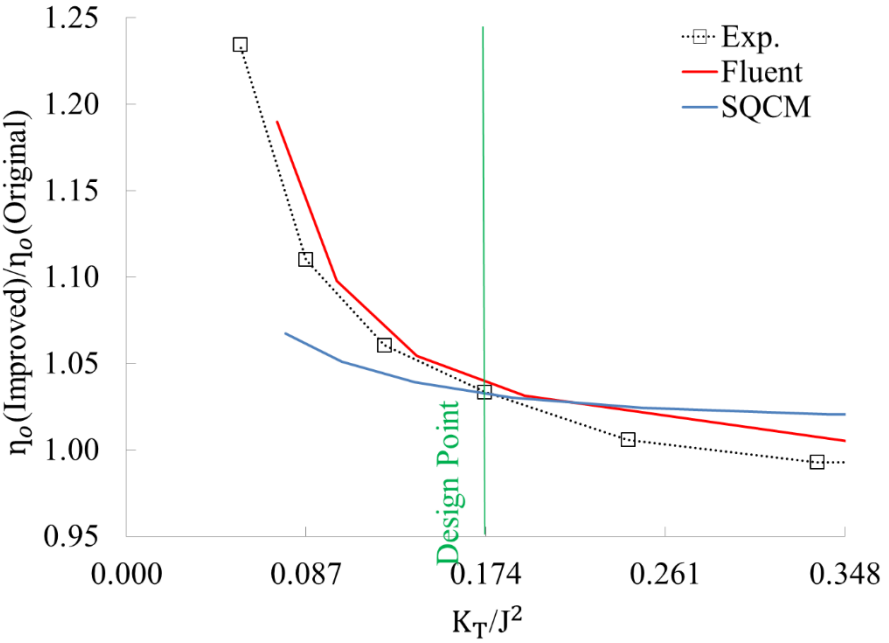

Fig. 4.23 Comparison of increasing propeller efficiency ratio versus K_T/J^2 in experiment and calculation

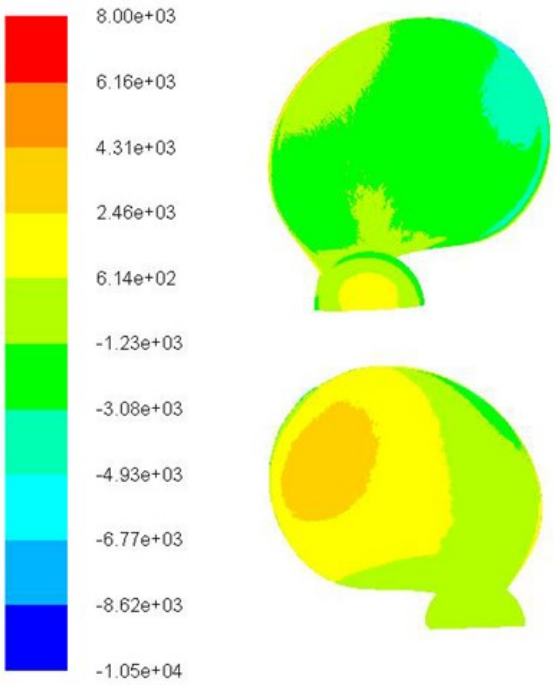

Fig. 4.24 Pressure distributions of improved LTBP on suction side (upper) and pressure side (lower)

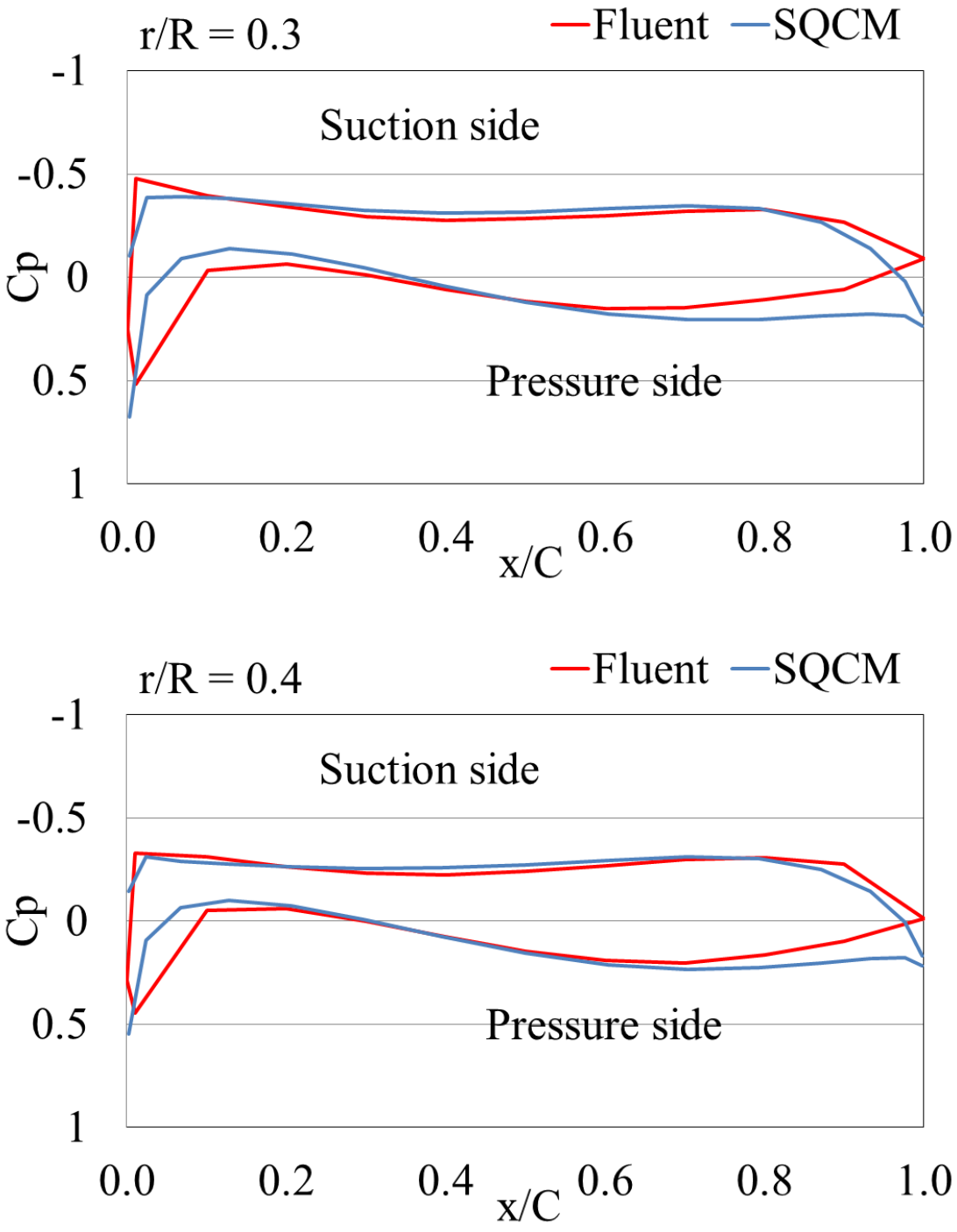

Fig. 4.25 Comparisons of pressure distributions between Fluent and SQCM (Improved LTBP, r/R=0.3 and 0.4, J=1.1)

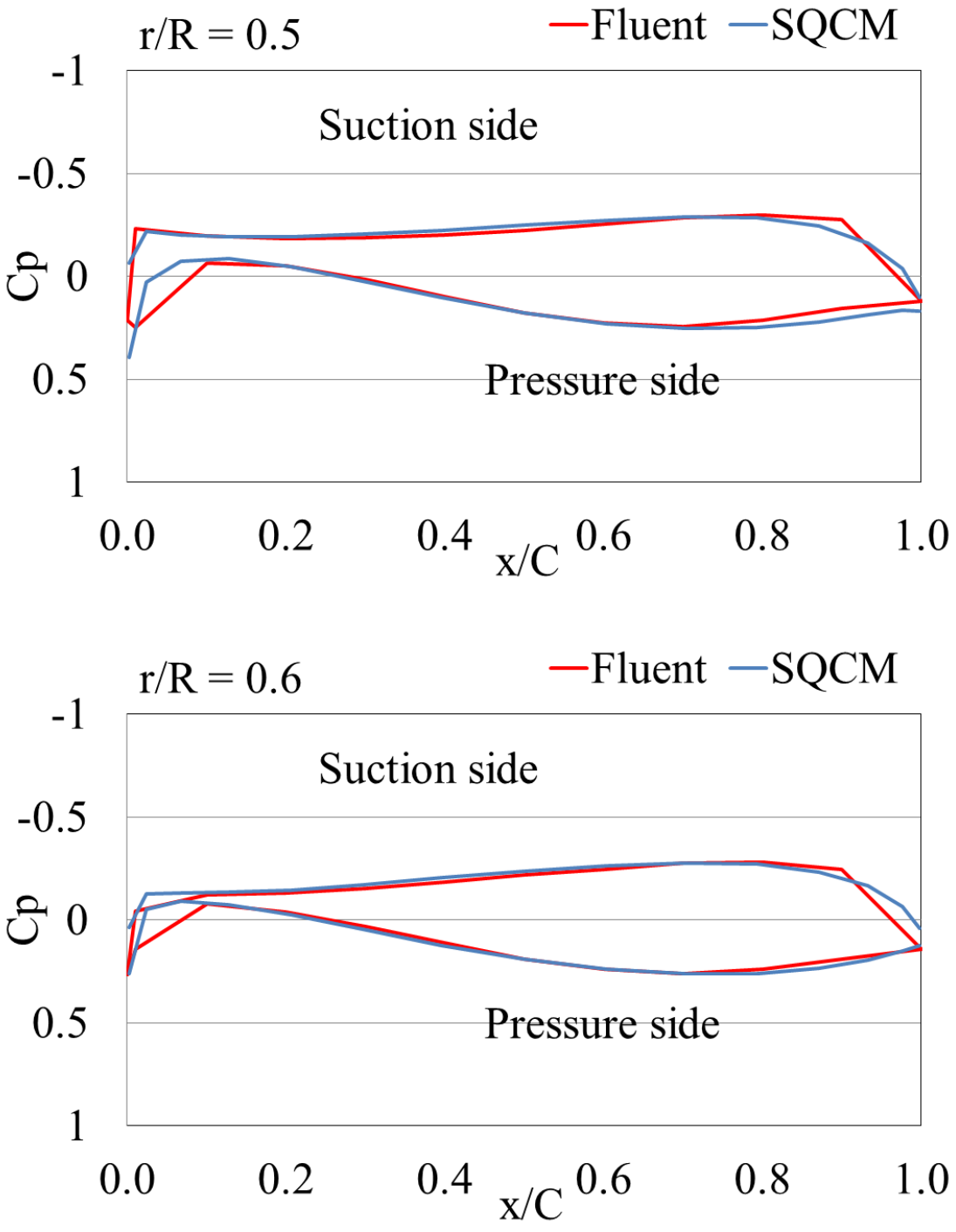

Fig. 4.26 Comparisons of pressure distributions between Fluent and SQCM (Improved LTBP, r/R=0.5 and 0.6, J=1.1)

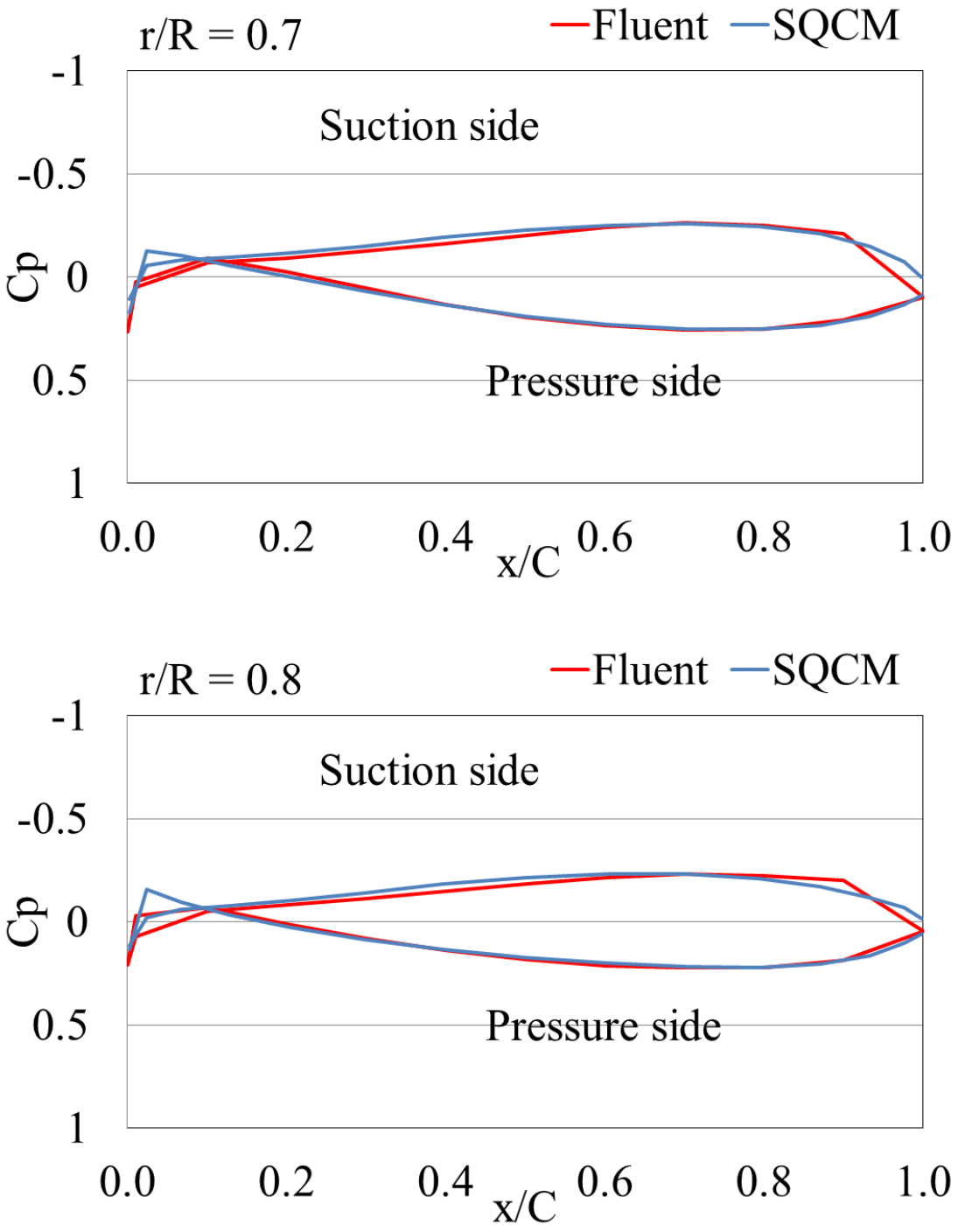

Fig. 4.27 Comparisons of pressure distributions between Fluent and SQCM (Improved LTBP, r/R=0.7 and 0.8, J=1.1)

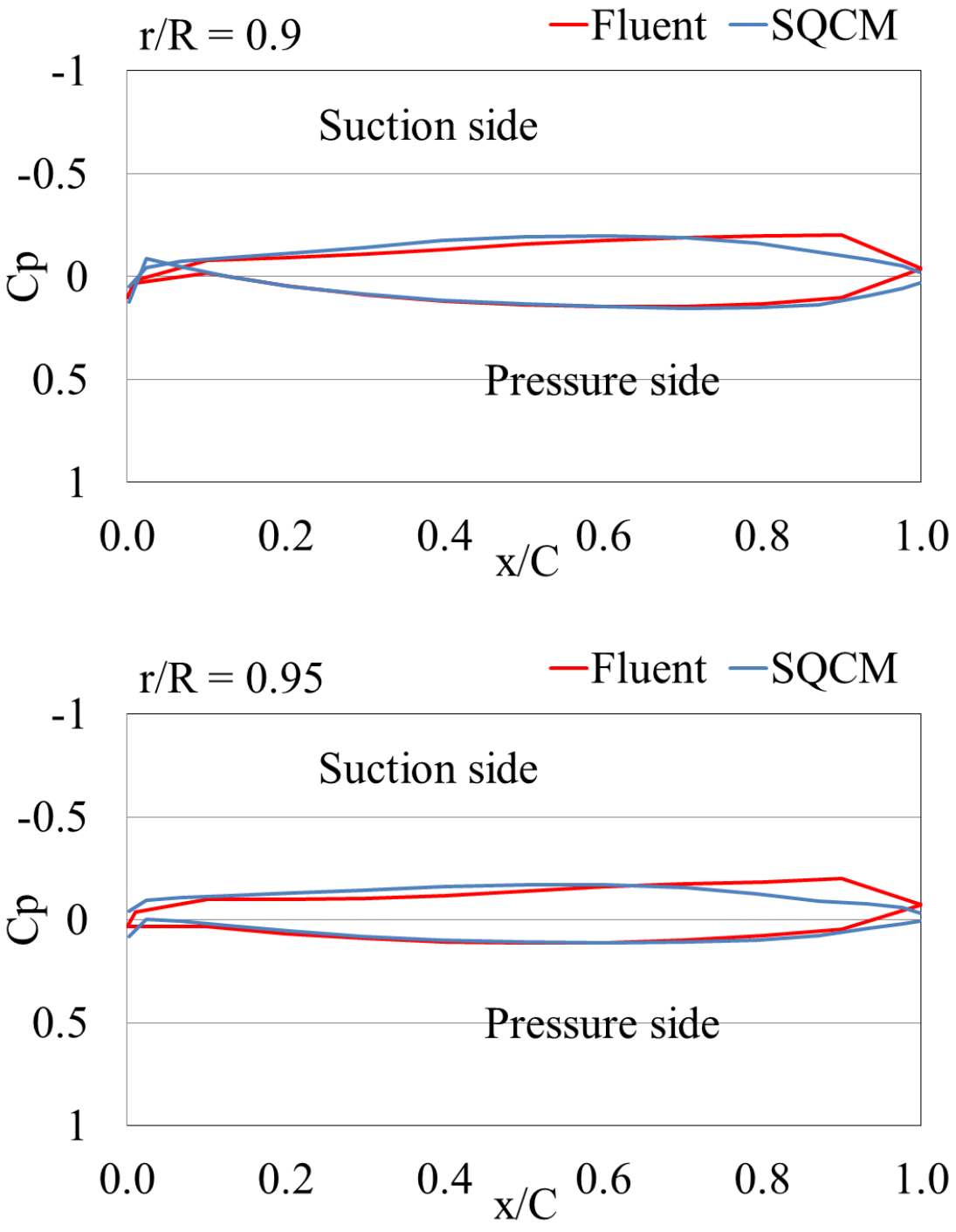

Fig. 4.28 Comparisons of pressure distributions between Fluent and SQCM (Improved LTBP, r/R=0.9 and 0.95, J=1.1)

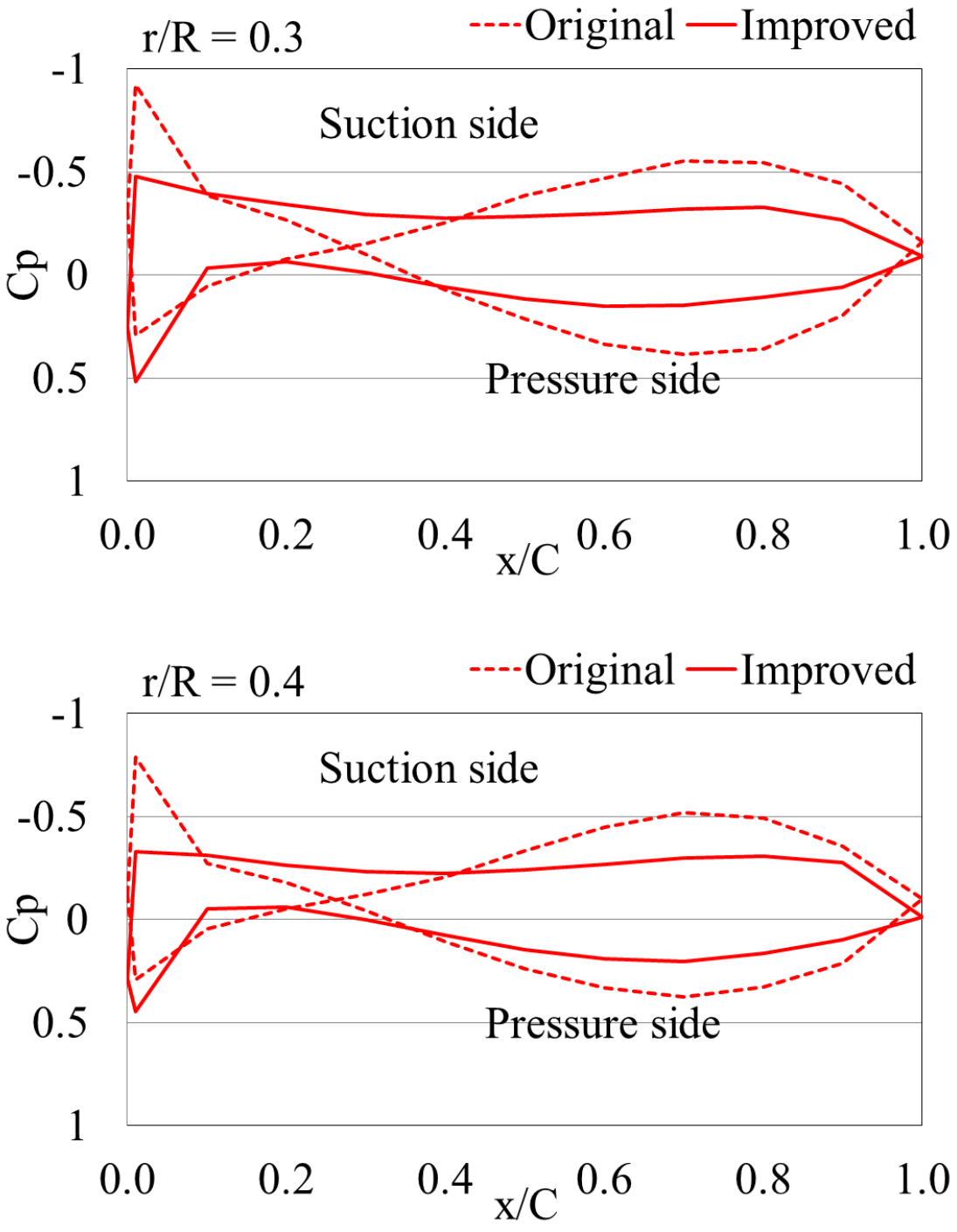

Fig. 4.29 Comparisons of pressure distributions between original and improved LTBPs obtained by Fluent (r/R=0.3 and 0.4, J=1.1)

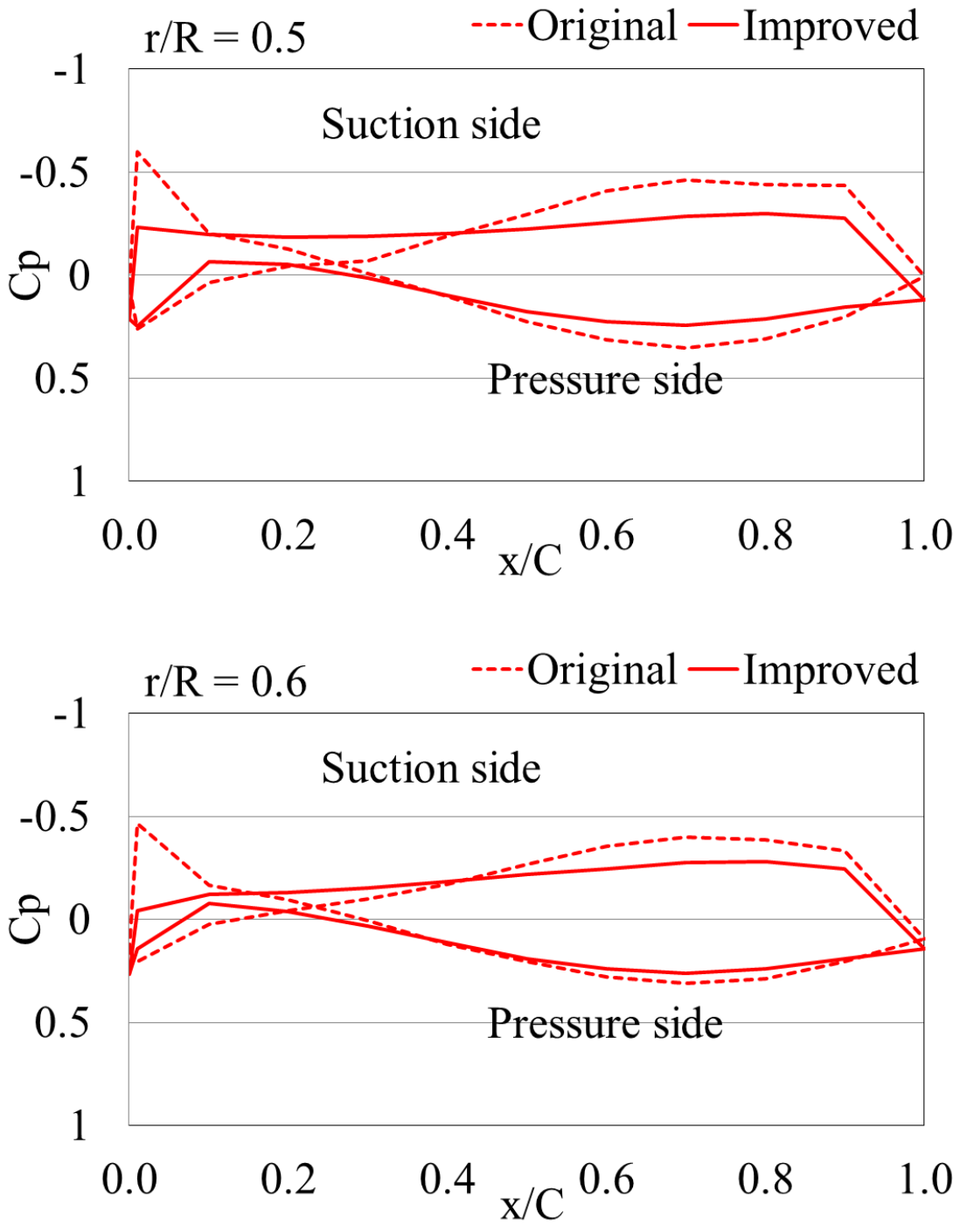

Fig. 4.30 Comparisons of pressure distributions between original and improved LTBPs obtained by Fluent (r/R=0.5 and 0.6, J=1.1)

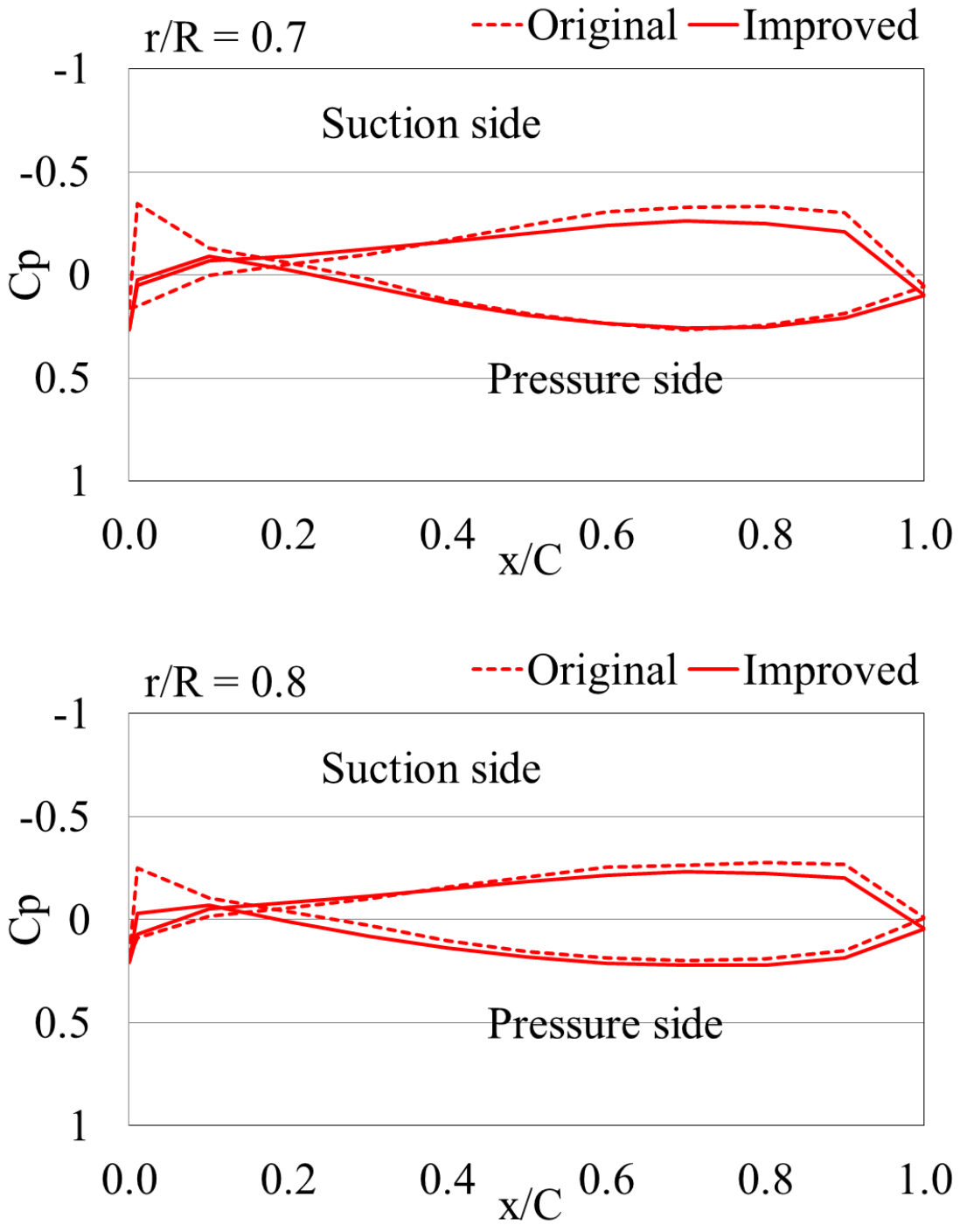

Fig. 4.31 Comparisons of pressure distributions between original and improved LTBPs obtained by Fluent (r/R=0.7 and 0.8, J=1.1)

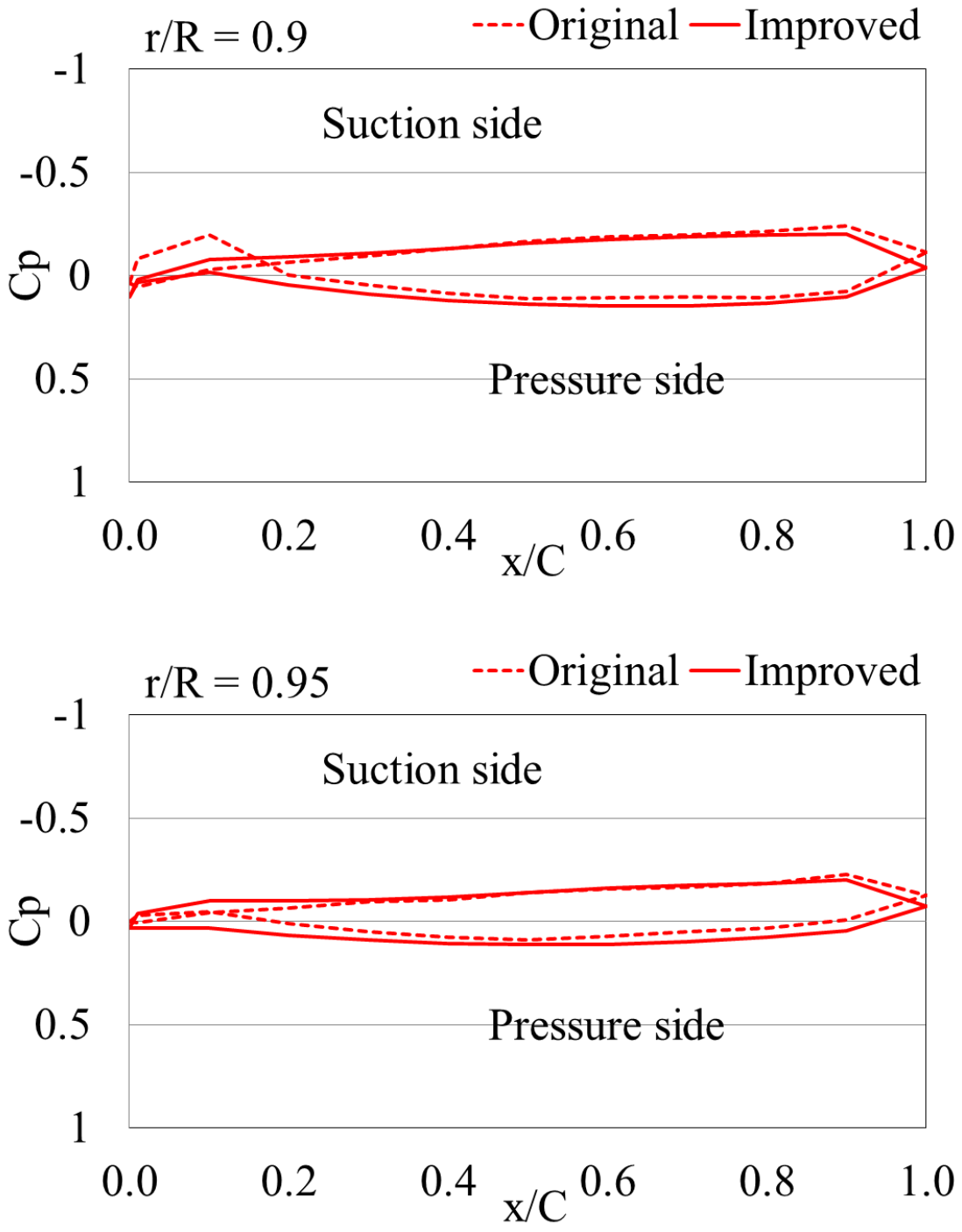

Fig. 4.32 Comparisons of pressure distributions between original and improved LTBPs obtained by Fluent (r/R=0.9 and 0.95, J=1.1)

4.4 Evaluation of Long-Tail Boat Propeller Characteristics in Inclined Shaft Condition

The previous section described the CFD prediction for improved model of Long-Tail Boat Propeller (LTBP) assuming steady-state flow with straight shaft propeller. This section describes the propeller performances of LTBP with inclined shaft propeller arrangement by using CFD. The inclined shaft angle of calculation is determined as same as the actual Long Tail Boat.

4.4.1 Computational Domain and Meshing

In the steady-state simulation with straight shaft propeller only the single blade domain is defined with periodic boundary condition in previous section. However, a single blade passage is insufficient to simulate the inclined shaft propeller arrangement because the flow around the propeller is not symmetric. Therefore, the whole domains with oblique flow should be considered.

The computational domain considering full blade propellers is shown in Fig. 4.33. It was split into two regions which are the rotating and fixed parts. The rotating part is called "Rotating" and the fixed part called "Stationary". The inflows V_{in} are decomposed into velocity components defined as: $V_x = V_{in} \cos \psi$ and $V_z = V_{in} \sin \psi$. The inclined shaft angle ψ is 12° in this study. Inflow velocity is imposed at the inlet and static pressure is set to constant which is equal to zero at the outlet. The propeller shaft length of computation has been resized into same ratio of propeller scale from actual shaft. The same computational domain sizes were imposed for the original and improved propellers which are shown in Table 4.1 where D is diameter of propeller.

The moving reference systems are employed to simulate the flow around a rotating with inclined shaft propeller. Turbulence intensity and turbulence viscosity at inlet boundary were prescribed to 3%. No-slip boundary condition was imposed for solid surfaces (blade and hub). Free-slip boundary condition was set for outer surface.

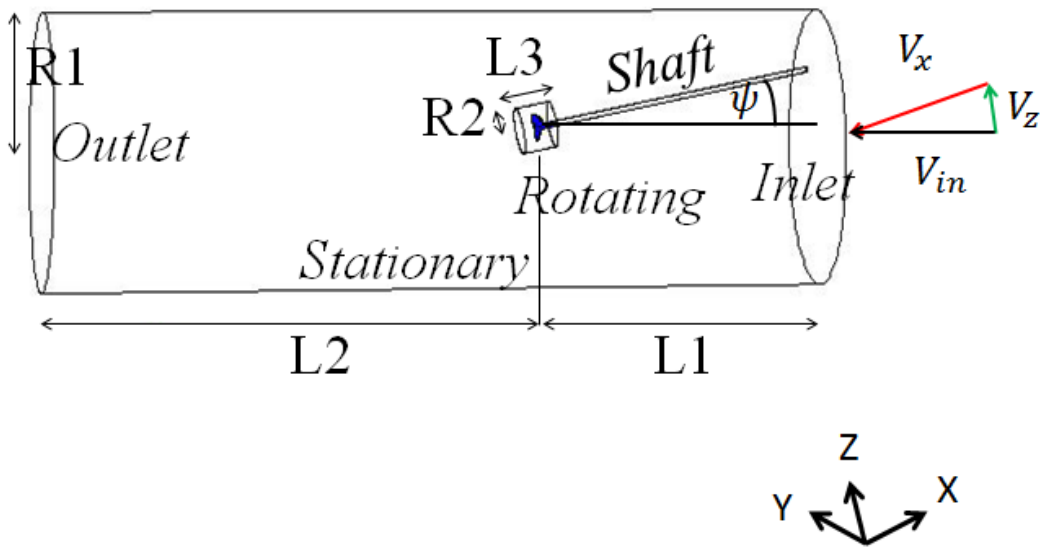

Fig. 4.33 Computational domains of LTBP with inclined shaft propeller arrangement

Table 4.1 Computational domain sizes for LTBP models with inclined shaft propeller arrangement

	Rotating	Stationary
L1		10.43D
L2		16.63D
L3	1.17D	
R1		4.41D
R2	0.73D	

The computational domains are discretized by hybrid-unstructured control volume mesh as shown in Fig. 4.34. Fig. 4.35 and Fig. 4.36 show the surface mesh at beside the propeller blade for original and improved propeller respectively. The grid quality of both propellers are similar, the grid independence was met with about 3.5 million cells for total grids which are divided to rotating part and stationary part containing about 2.4 million and 1.1 million cells respectively. The prismatic layers were imposed around blade and hub. The average values of y^+ on the solid surfaces (blade and hub) were used 30.

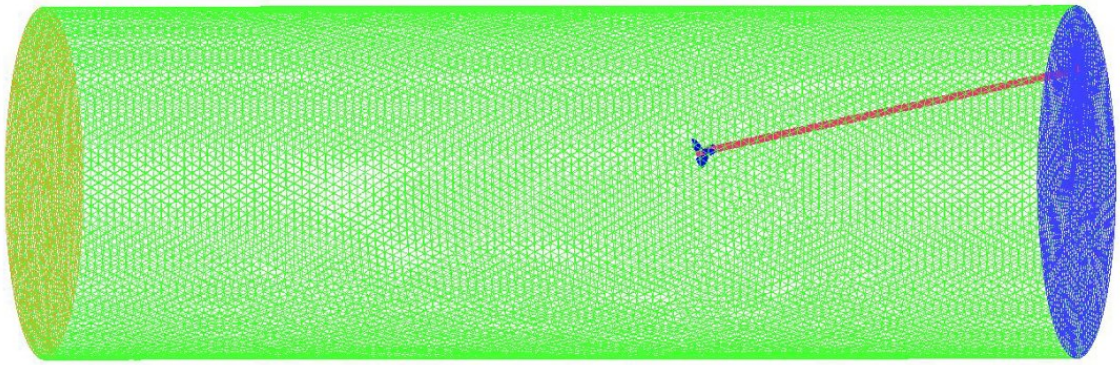

Fig. 4.34 Computational domain mesh of LTBP with inclined shaft propeller arrangement

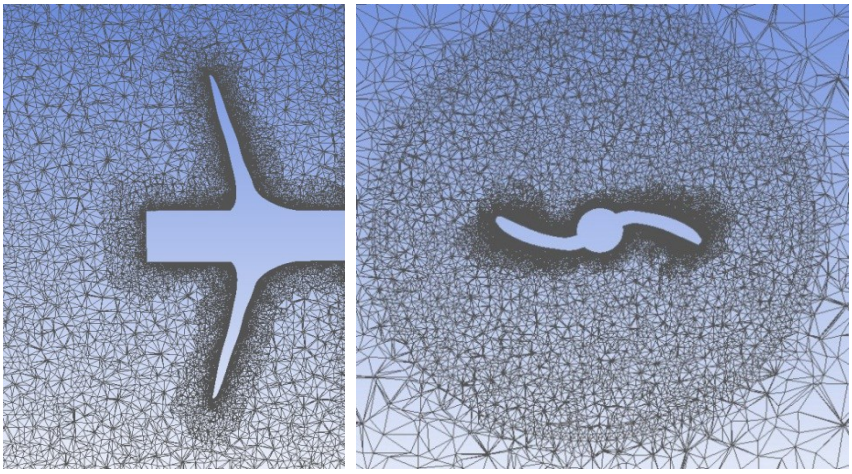

Fig. 4.35 Mesh at beside blade and hub of original LTBP with inclined shaft propeller for side view (left) and top view (right)

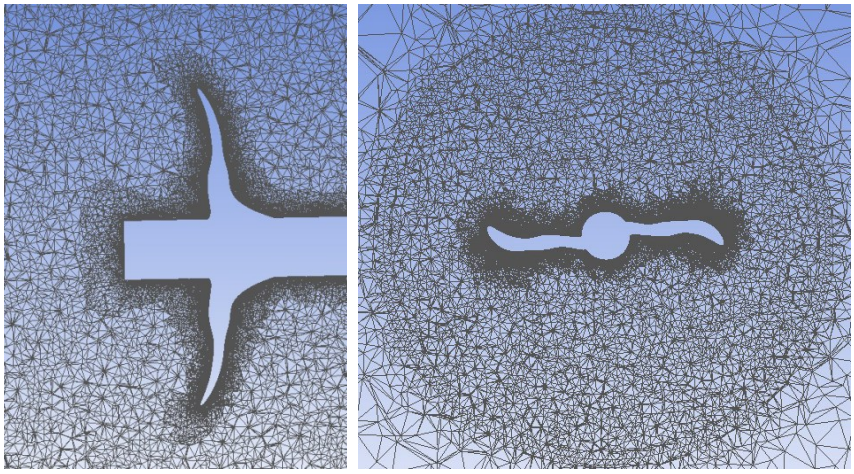

Fig. 4.36 Mesh at beside blade and hub of improved LTBP with inclined shaft propeller for side view (left) and top view (right)

4.4.2 Calculated Results

The calculation with inclined shaft propeller is conducted to oblique flow angle with 12° which is the same as actual value of inclined shaft angle of Long-Tai Boat. The propeller rotational speed was fixed 10 rps which was the same as steady-state simulation with straight shaft propeller in previous section. Unfortunately, results of this calculation are not compared to the measured data because experimental apparatus have limited capability.

The propeller performances of LTBP original model are compared between inclined shaft and straight shaft propellers in Fig. 4.37. It is found that the thrust and torque coefficients of both conditions were seen equally at J=0.5-1.1 but the thrust and torque coefficients of inclined shaft were seen slightly increased at advance coefficients more than J=1.1. The propeller efficiency at J=0.5-1.0 are seen to be the same for both condition but at advance coefficient more than J=1.0, the propeller efficiency with inclined shaft is better than that with straight shaft. At J=1.1 (design point), the propeller efficiency in inclined shaft condition is increased approximately 2.8 %.

The propeller performances of improved LTBP model are compared between inclined shaft and straight shaft propeller as shown in Fig. 4.38. It is demonstrated that the tendency of thrust, torque coefficients and propeller efficiency in the inclined shaft condition were similar to Fig. 4.37. At J=1.1 (design point), the propeller efficiency of inclined shaft is increased approximately 3.5 %.

The calculated results of propeller performances with inclined shaft propeller were compared between original and improved model as shown in Fig. 4.39. It is illustrated that the thrust and torque coefficients of improved model are slightly increased from original model in ranges of advance coefficient. The propeller efficiency of improved model are increased at advance coefficients more than J=1.0. At J=1.1 (design point), the propeller efficiency of improved model is increased approximately 3.6 %. Fig. 4.40 shows comparison of propeller efficiency versus K_T/J^2 between original and improved propellers in inclined shaft condition. It is found that the propeller efficiency of improved model at design point is increased approximately 7.0 %.

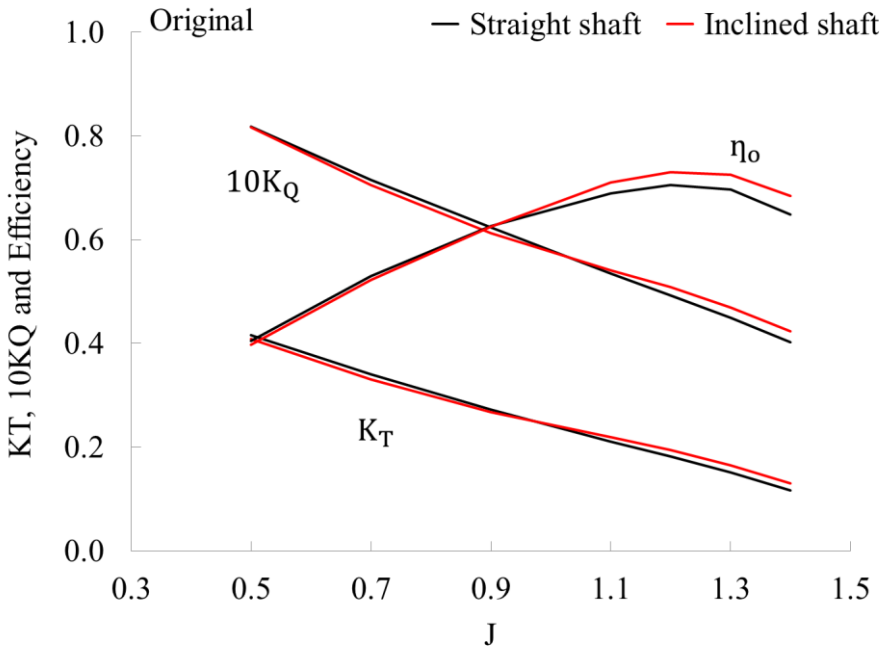

Fig. 4.37 Comparison of calculated propeller characteristics of original LTBP in straight and inclined shaft conditions

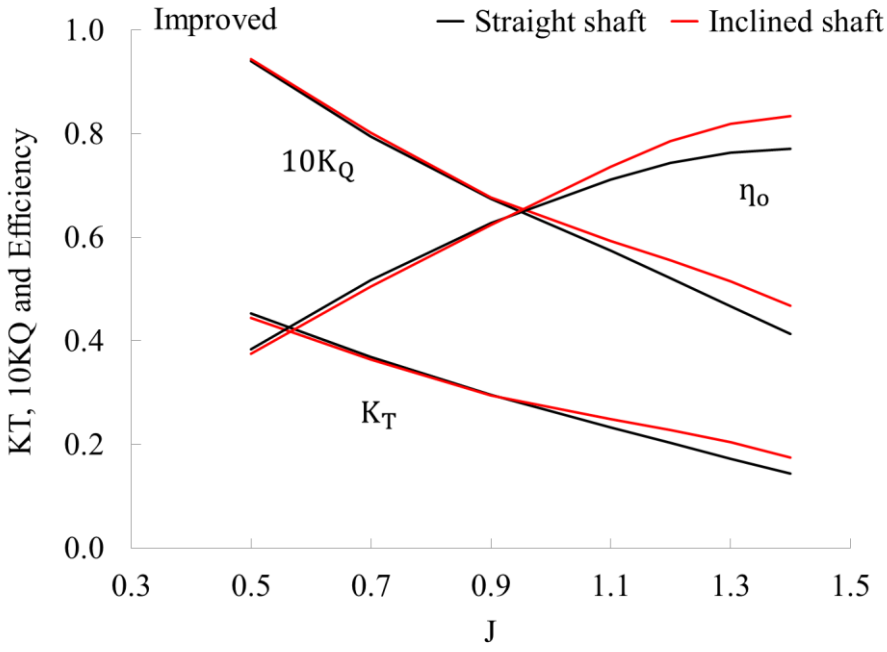

Fig. 4.38 Comparison of calculated propeller characteristics of improved LTBP in straight and inclined shaft conditions

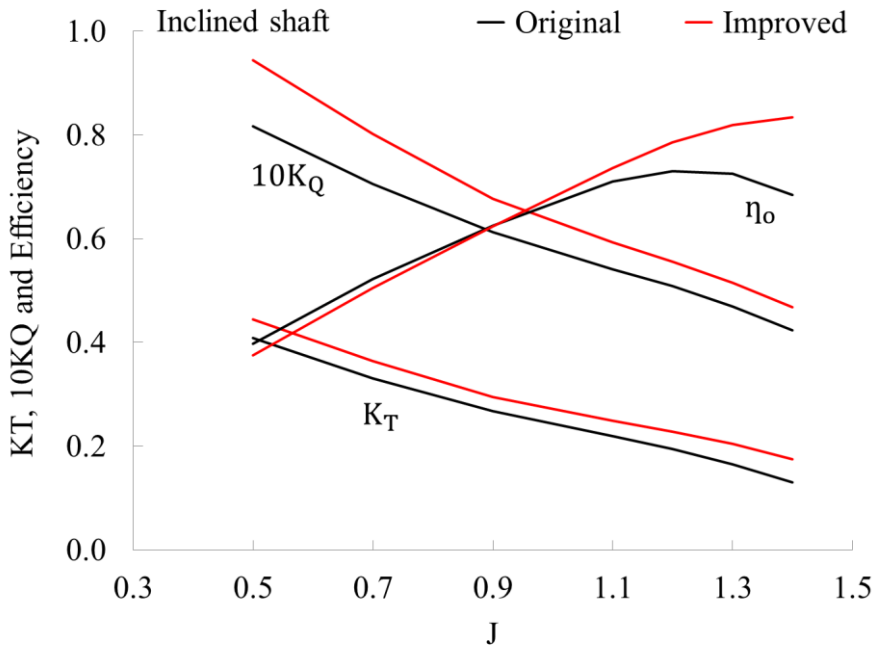

Fig. 4.39 Comparison of calculated propeller characteristics of original and improved LTBPs in inclined shaft condition

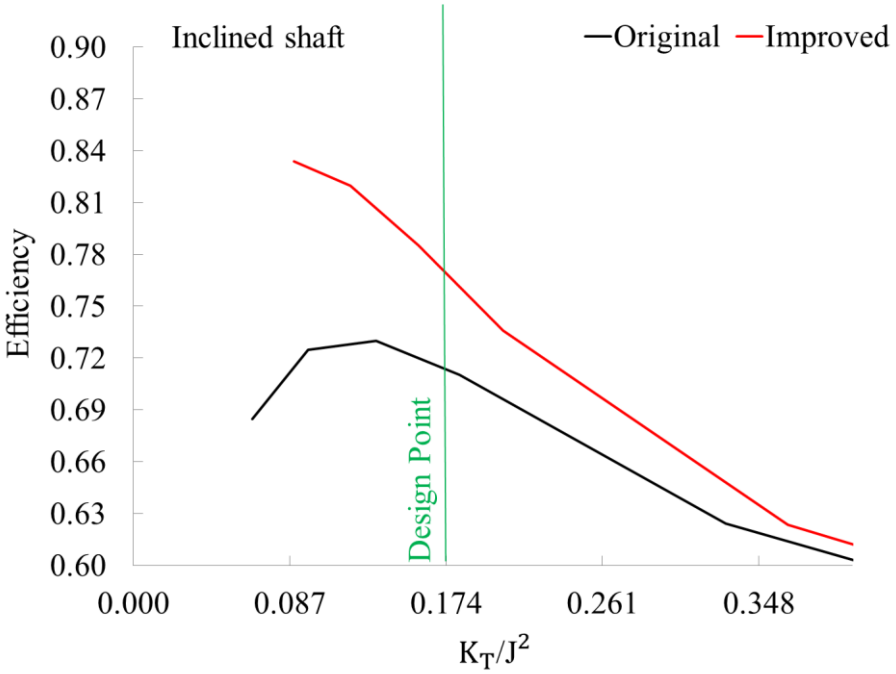

Fig. 4.40 Comparison of calculated propeller efficiency versus K_T/J^2 of original and improved LTBP in inclined shaft condition

4.5 Conclusion

In this chapter, the optimization method of propeller blade shape using real-coded genetic algorithm was described. The model test of the improved propeller obtained by the present optimization method was conducted in straight shaft condition using the high speed circulating water channel at Kyushu University. The characteristics of the original and improved propellers in inclined shaft condition were evaluated by the present CFD analysis system. As a result, the following are confirmed.

(1) Though the optimization was conducted keeping the same thrust to the original value at the design point, the thrust of the improved propeller was slightly increased in the experiment. Consequently the propeller efficiency of the improved propeller in straight shaft condition was increased approximately 3.3% in the experiment.

(2) Calculated thrust, torque and propeller efficiency in inclined shaft condition were increased from those in straight shaft condition for the both original and improved propellers. In inclined shaft condition the thrust and the torque of the improved propeller were increased in all advance coefficient range. The propeller efficiency was better than the original propeller in high advance coefficient range including design point.

Chapter 5
Conclusions

The propulsion systems of Long-Tail Boat propeller have never been studied with theoretical methods. Therefore, the evaluation the propeller performance of standard propeller of Long-Tail Boat in Thailand by model test and optimization of propeller blade shapes were done in this study. The summary of this thesis is as follows.

In Chapter 1, the background literature review and purpose of this study were presented.

In Chapter 2, CFD analysis system based on the ANSYS Fluent for evaluation of propeller performance in straight and inclined shaft conditions was introduced. Validation on the present method was conducted referring the experimental data of two well-known propellers. More detailed results are as follows.

(1) In the experiment of N4990 propeller, the propeller characteristics (thrust, torque and propeller efficiency) are changed by inclined shaft angle. Especially the propeller efficiency in inclined shaft condition is higher than that in straight shaft condition by approximately 1-7 %. The tendency of the calculated results is nearly the same to the experimental data.

(2) The calculated mean pressure distribution, first harmonic amplitude and first harmonic phase angle were compared with experimental data of P4679 propeller. The calculated results agree well with the experimental data.

In Chapter 3, model test of the standard propeller of Long-Tail Boat from Bangkok in Thailand was conducted in straight shaft condition using the high speed circulating water channel at Kyushu University. The calculated characteristics by the presented CFD analysis system agree well with the experimental data in wide advance coefficient range. The propeller efficiency obtained by SQCM also agree well with the experimental data nearly design point.

In Chapter 4, the optimization method of propeller blade shape using real-coded genetic algorithm was described. The model test of the improved propeller obtained by the present optimization method was conducted in straight shaft condition using the high speed circulating water channel at Kyushu University. The characteristics of the original and improved propellers in inclined shaft condition were evaluated by the present CFD analysis system. More detailed results are as follows.

(1) Though the optimization was conducted keeping the same thrust to the original value at the design point, the thrust of the improved propeller was slightly increased in the experiment. Consequently the propeller efficiency of the improved propeller in straight shaft condition was increased approximately 3.3% in the experiment.

(2) Calculated thrust, torque and propeller efficiency in inclined shaft condition were increased from those in straight shaft condition to the both original and improved propellers. In inclined shaft condition thrust and torque of the improved propeller were increased in all advance coefficient range. The propeller efficiency was better than the original propeller in high advance coefficient range including design point.

The future works for numerical calculation of propeller performances are suggested as follows:

- CFD calculated results of original propeller are very good with compared the experiment including at design point but calculated results of improved propeller are slightly overestimated. Further research is needed to investigate the reasons of difference between calculated and experimental results

- High speed propeller such as Long-Tail Boat propeller should consider cavitation in design stage. Further work is necessary to study cavitation effect.

Acknowledgments

I am most indebted to Professor Jun Ando of Department of Marine Systems Engineering of Faculty of Engineering in Kyushu University who is supervisor. He helped me for continuous support, guidance, inspiration, and sharing expertise and wisdom regarding research.

I am grateful to Professor Yoshitaka Furukawa of Department of Marine Systems Engineering of Faculty of Engineering in Kyushu University and Professor Satoshi Watanabe of Department of Mechanical Engineering of Faculty of Engineering in Kyushu University, for helping me in writing this thesis through their valuable suggestions and comments.

I would like to thank Assistant Professor Akira Yoshitake who helped me for support information in experimental data and other. I would also like to thank Assistant Professor Takashi Kanemaru who suggested me about knowledge of propeller and numerical methods and other.

I thank friend, faculty member who have helped me in this research. They made my graduate school have enjoyed.

Finally, special thanks to my parents for all their love and encouragement. Without them, this study would not have been completed.

References

[1] Matichon Public Co., Ltd, June, 2013.

[2] Marine Department, Ministry of Transport, Thailand, 2014.

[3] Boswell, R. J. : "Design Cavitation Performance and Open-Water Performance of a Series of Research Skewed Propeller", Naval Ship Research and Development Center, Report 3339, 1971.

[4] Ukon, Y., Kurobe, Y. and Kudo, T. : "Measurement of Pressure Distribution on a Conventional and a Highly Skewed Propeller Model under Non-Cavitating Condition", Journal of Society of Naval Architects of Japan, Vol. 165, pp.83-94, 1989.

[5] Ukon, Y., Kudo, T., Kurobe, Y., Kamiirisa, H., Yuasa, H., Kubo, H. and Itadami, Y. : "Measurement of Pressure Distribution on a Full Scale Propeller Measurment on a Conventional Propeller", Journal of Society of Naval Architects of Japan, Vol.168, pp.65-75, 1990.

[6] Ukon, Y., Kudo, T., Kurobe, Y., Yuasa, H., Kamiirisa, H. and Kubo, H. : "Measurement of Pressure Distribution on a Full Scale Propeller Measurement on a Highly Skewed Propeller", Journal of Society of Naval Architects of Japan, Vol.170, pp.111-123, 1991.

[7] Stella, A., Guj, G., Di Felice, F. and Elefante, M. : "Propeller Wake Evolution Analysis by LDV", Proceedings of the 22nd Symposium on Naval Hydrodynamics, pp.171–180, Washington, DC, USA, 1998.

[8] Chesnaks, C. and Jessup, S. : "Experimental Characterisation of Propeller Tip Flow", Proceedings of 22nd Symposium on Naval Hydro-dynamics, pp.156–169, Washington, DC, USA, 1998.

[9] Calcagno, G., Di Felice, F., Felli, M. and Pereira, F. : "Propeller Wake Analysis Behind a Ship by Stereo PIV", Proceedings of 24th Symposium on Naval Hydrodynamics, pp.112–127, Fukuoka, Japan, 2002.

[10] Lee, S. J., Paik, B.G. and Lee, C.M. : "Phase-Averaged PTV Measurements of Propeller Wake", Journal of Ship Research 49(1), pp.43–54, 2004.

[11] Bertetta, D., Brizzolara,S., Canepa, E., Gaggero,S. and Viviani, M. : "EFD and CFD Characterization of a CLT Propeller", International Journal of Rotating Machinery Vol.2012.

[12] Hess, J. L. and Valarezo, W. O. : "Calculation of Steady Flow about Propeller by Mean of Surface Panel Method", Proceedings Research and Technology Douglas Aircraft Company, Long Beach, CA. 1985.

[13] Kerwin, J. E., Kinnas, Spyros, A., Lee, Jin-Tae, Shih and Wei-Zen. : "A Surface Panel Method for the Hydrodynamic Analysis of Ducted Propeller", Transactions of Society of Naval Architects and Marine Engineer 95, pp.93-122, 1987.

[14] Ando, J., Maita, S. and Nakatake, K. : "A Simple Panel Method to Predict Steady Marine Propeller Performance", Journal of Society of Naval Architects of Japan, Vol.178, pp.61-69, 1995.

[15] Abdel-Maksoud, M., Menter, F. and Wuttke, H. : “Viscous Flow Simulation for Conventional and High-Skew Marine Propellers”, Journal of Ship Technology, 1998.
[16] Chen, B. and Stern, F. : “Computational Fluid Dynamics of Four-Quadrant Marine-Propulsor Flow”, Journal of Ship Research, 43(4), pp.208-228, 1999.
[17] Watanabe, T., Kawamura, T., Takekoshi, Y., Maeda, M. and Rhee, S. : “Simulation of Steady and Unsteady cavitation on Marine Propeller using RANS CFD code”, In Fifth International Symposium on Cavitation, CAV, Osaka, Japan, 2003.
[18] Rhee, S.H. and Joshi, S. : “Computational Validation for Flow around Marine Propeller using Unstructured Mesh based Navier-Stokes Solver”, The Japan Society of Mechanical Engineers, International Journal, Series B, 48(3), pp.5620-570, 2005.
[19] Kawamura, T., Takekoshi, Y., Yamaguchi, H., Minowa, T., Maeda, M., Fujii, A., Kimura, K. and Taketani, T. : “Simulation od Unsteady Cavitation Flow around Marine Propeller using RANS CFD code”, In Sixth International Symposium on Cavitation, CAV, Wageningen, The Netherlands, 2006.
[20] Morgut, M. and Nobile, E. : “Comparison of Hexa-structured and Hybrid-Unstructured Meshing Approaches for Numerical Prediction of the Flow around Marine Propeller”, First International Symposium on Marine Propellers, Trondheim, Norway, 2009.
[21] Kaewkhiaw, P., Yodchai, T., Dechauophai, P. and Juntasaro, V. : “Simulation of Cavitation on Marine Propeller using CFD”, Master thesis of Engineering, Graduate School, Kasetsart University, Thailand, 2010.
[22] Bertetta, D., Brizzolara, S., Canepa, E., Gaggero, S. and Viviani, M. : “EFD and CFD Characterization of a CLT Propeller”, International Journal of Ratating Machinery, 2012.
[23] Baek. D. G., Jung, J.H. and Yoon, H.S. : “ Effects of The Advance Ratio on the Evolution of Propeller Wake”, Proceeding of the International Conference on Environment, Energy, Ecosystems and Development, 2013.
[24] Molland, A. F, Turnock, S. R. and Hudson, D. A. : “Ship Resistance and Propulsion”, First Published, 2011.
[25] Taniguchi, K., Tanibayashi, H. and Chiba, N. : “Investigation into the propeller cavitation in oblique flow”, The Society of Naval Architects of Japan, 1967.
[26] Boswell, R., Jessup, S. and Kim, K-H. : “Periodic single blade loads on propeller is tangential and longitudinal wakes”, Society of Naval Architects and Marine Engineers(SNAME) Propeller Symposium, Virginia Beach, USA, 1981.
[27] Boswell, R., Jessup, S., Kim, K-H. and Dahmer, D. : “Single Blade Loads on Propeller in Inclined and Axial Flows”, Technical Report, DTNSRDC-84/084, DTNSRDC, November, 1984.
[28] Jessup, S. D. : “Measurements of the Pressure Distribution on the Two Model Propeller”, David Taylor Naval Research and Development Center report, DTNSRDC-82/035, 1982.
[29] Jessup, S. D. : “Measurement of Multiple Blade Rate Unsteady Propeller Forces”, Technical Report, DTRC-90/015, May, 1990.

[30] Gindroz, B., Hoshino. T and Pylkkanen, J. : "Proceeding of 22nd ITTC Propulsion Committee Propeller RANS/Panel Method Workshop", Grenoble, France, 1998.
[31] Ukon, Y., Kudo., T., Yuasa., H. and Kamiirisa, H. : "Measurements of Pressure Distribution on Full Scale Propeller", Proceedings of Society of Naval Architects and Marine Engineers(SNAME) Propeller/shafting Symposium, Virginia Beach, USA, 1991.
[32] Raestad, M. : "Experimental Data Provided for the Norwegian Propeller Forum", Courtesy by DNV, 2007.
[33] Kerwin, J. and Lee, C.S. : "Prediction of Steady and Unsteady Marine Propeller Performance by Numerical Lifting Surface Theory", Transactions of Society of Naval Architects and Marine Engineers, 1978.
[34] Liu, P. and Bose, N. : "An Unsteady Panel Method for Highly Skewed Propellers in Non-Uniform Inflow", 22nd ITTC Propulsion committee propeller RANS/Panel method workshop, Grenoble, France, 1998.
[35] Hoshino, T. : " Comparative calculations of propeller performance in steady and unsteady flows using a surface panel method", 22nd ITTC Propulsion committee propeller RANS/Panel method workshop, Grenoble, France,1999.
[36] Hsin, C. Y. : "Development and Analysis of Panel Method for Propeller in Unsteady Flow", Ph.D.Thesis, Massachusetts Institute of Technology, USA, 1990.
[37] Gaggero, S., Villa, D. and Brizzolara, S. : "RANS and Panel Method for Unsteady Flow Propeller Analysis", 9th International Conference on Hydrodynamics, October, 2010, Shanghai, China, 2010.
[38] Politis, G.K. : "Simulation of Unsteady Motion of a Propeller in a Fluid Including Free Wake Modeling", Engineering Analysis with Boundary Elements, Vol. 28, pp.633-653, 2004.
[39] Krasilnikov, V., Zhang, Z. and Hong, F. : "Analysis of Unsteady Propeller Blade Forces by RANS", First International Symposium on Marine Propulsors (SMP'09), Trondheim, Norway, 2009.
[40] Schroeder, S.D. and Dai, C.M. : "Numerical Simulation of a Marine Propeller in a Cross Flow", 5th European Conference on Computational Fluid Dynamics, Portugal, 2010.
[41] Schroeder, S.D. and Dai, C.M. : "Numerical Simulation of Propeller Performance with an Inclined Shaft Arrangement", Technical report of Naval Surface Warfare Center Carderock Division, 2010.
[42] Dubbioso, G., Muscari, R. and Mascio, A.D. : "CFD Analysis of Propeller Performance in Oblique Flow", Third International Symposium on Marine Propulsor (SMP'13), Launceston, Tasmania, Australia, 2013.
[43] Kaewkhiaw, P. and Ando, J. : "Numerical Simulation for Unsteady Propeller Performance with Inclined Propeller Arrangement using CFD", 11th International Conference on Hydrodynamics, October, Singapore, 2014.
[44] Dai, C., Hambric, S., Mulvihill, L, Tong, S. S. and Powell, D. : "A Prototype Marine Propulsion Design Tool using Artificial Intelligence and Numerical Optimization Techniques", Transactions of Society of Naval Architects and Marine Engineers, Vol.102, pp.57-69, 1994.

[45] Mishima, S. and Kinnas, S.A. : “Application of Numerical Optimization Technique to the Design Cavitating Propellers in Non Uniform Flow”, Journal of ship research, Vol.41, pp.93-107, 1997.
[46] Jang, T.S., Kinoshita, T. and Yamaguchi, T. : “A New Functional Optimization Method Applied to Pitch Distribution of Marine Propeller”, Journal of Marine Science and Technology, 2001.
[47] Takekoshi, Y., Kawamura, T., Yamakuchi, H., Maeda, M., Ishii, N., Kimura, K., Taketani, T. and Fujii, A. : “Study on the Design of Propeller Blade Sections using the Optimization algorithm”, The Journal of Marine Science and Technilogy, 2005.
[48] Karim, M. M., Ikehata, M., Suzuki, K. and Kai, H. : “Application of Micro-Genetic Algorithm (μGA) to the Optimal Design of Lifting Bodies”, Journal of the Kansai Society of Naval Architects, Japan, No.235, pp.1-8, 2001.
[49] Ando, J., Kataoka, S. and Ryu, T. : “A Method to Improve Propeller Performance Using Real-coded Genetic Algorithm”, Proceedings of International Propulsion Symposium IPS’10, pp. 32-37, 2010.
[50] ANSYS Fluent 14.0 Theory Guide, Fluent Inc, November, 2011.
[51] Launder, B.E. and Spalding, D. B. : “Lectures in Mathematical Models of Turbulence”, Academic Press, London, England, 1972.
[52] Menter, F.R. : “Two-Equation Eddy-Viscosity Turbulence Models for Engineering Applications”, AIAA Journal, pp.1598–1605, August, 1994.
[53] Wilcox, D.C. : “Turbulence Modeling for CFD. DCW Industries”, Inc. La Canada, California, 1998.
[54] Kaewkhiaw, P., Yodchai, T., Dechauophai, P. and Juntasaro, V. : “Simulation of Cavitation on Marine Propeller using CFD”, Master thesis of Engineering, Graduate School, Kasetsart University, Thailand, 2010.
[55] Patankar, S. V. and Spalding, D.B. : “A calculation procedure for heat, mass and momentum transfer in three-dimensional parabolic flows”, International Journal of Heat and Mass Transfer, Volume 15, Issue 10, October, 1972.
[56] Krasilnikov, V., Zhang, Z. and Hong, F. : “Analysis of Unsteady Propeller Blade Forces by RANS”, First International Symposium on Marine Propulsors, Trondheim, Norway, June, 2009.
[57] Ono, I., Satoh, H. and Kobayashi, S. : “A real-coded genetic algorithm for function optimization using the unimodal normal distribution crossover”, Journal of Japanese Society for Artificial Intelligence, Vol.14, No.6, pp.1146-1155, 1999.
[58] Ono, I., Kobayashi, S. and Yoshida, K. : “Optimal lens design by real-coded genetic algorithms using UNDX”, Computer Methods in Applied Mechanics and Engineering, Vol.186, pp.483-497, 2000.
[59] Satoh, H., Ono, I. and Kobayashi, S. : “A new generation alternation method of genetic algorithms and its assessment”, Journal of Japanese Society for Artificial Intelligence, Vol.12, No.5, pp.734-744, 1997.

Appendix A

Turbulence Model

(1) Standard *k*-ε Model

The standard *k*-ε model is a model based on model transport equation for the turbulence kinetic energy *k* and dissipation rate ε. The model transport equation for *k* is derived from the exact equation while the model transports equation for ε is obtained using physical reasoning and little resemblance to its mathematically exact counterpart ε. In the derivation of the *k*-ε model, the assumption is that the flow is fully turbulent and the effects of molecular viscosity are negligible. Therefore, the standard *k*-ε model is valid only for fully turbulent flows.

The standard *k*-ε model proposed by Launder and Spalding [51], the turbulent velocity and the turbulent length scale are defined by means of the turbulent kinetic energy *k* and dissipation rate ε as follows:

$$V_t = \sqrt{k} \qquad L_t = \frac{k^{3/2}}{\varepsilon} \tag{A.1}$$

And the turbulent dynamic viscosity is defined as follows:

$$\mu_t = C\rho V_t L_t = \rho C_\mu \frac{k^2}{\varepsilon} \tag{A.2}$$

The turbulent kinetic energy and dissipation rate are evaluated by the following transport equations:

$$\frac{\partial}{\partial t}(\rho k) + \frac{\partial}{\partial x_i}(\rho k u_i) = \frac{\partial}{\partial x_j}\left[\left(\mu + \frac{\mu_t}{\sigma_k}\right)\frac{\partial k}{\partial x_j}\right] + G_k + G_b - \rho\varepsilon - Y_M \tag{A.3}$$

$$\frac{\partial}{\partial t}(\rho\varepsilon) + \frac{\partial}{\partial x_j}(\rho\varepsilon u_j) = \frac{\partial}{\partial x_j}\left[\left(\mu + \frac{\mu_t}{\sigma_\varepsilon}\right)\frac{\partial \varepsilon}{\partial x_j}\right] + C_{1\varepsilon}\frac{\varepsilon}{k}(G_k C_{3\varepsilon} G_b) - C_{2\varepsilon}\rho\frac{\varepsilon^2}{k} \tag{A.4}$$

In these equations, G_k represents the generation of turbulence kinetic energy due to the mean velocity gradients. G_b is the generation of turbulence kinetic energy due to buoyancy. Y_M represents the contribution of the fluctuating dilatation in compressible

turbulence to the overall dissipation rate. $C_{1\varepsilon}$, $C_{2\varepsilon}$, and $C_{3\varepsilon}$ are constants. σ_k and σ_ε are the turbulent Prandtl numbers for k and ε respectively.

The model constants $C_{1\varepsilon}$, $C_{2\varepsilon}$, C_μ, σ_k and σ_ε have the following default values: $C_{1\varepsilon}$ = 1.44, $C_{2\varepsilon}$ = 1.92, C_μ= 0.09, σ_k= 1.0, σ_ε = 1.3

The term G_k representing the production of turbulence kinetic energy, the exact equation for the transport of k, this term may be defined as:

$$G_k = -\rho\overline{u_i' u_j'}\frac{\partial u_j}{\partial x_i} \tag{A.5}$$

To evaluate G_k in a manner consistent with the Boussinesq hypothesis is defined as:

$$G_k = \mu_t S^2 \tag{A.6}$$

Where S is the modulus of the mean rate of strain tensor is defined as:

$$S \equiv \sqrt{2S_{ij}S_{ij}} \tag{A.7}$$

$$G_b = \beta g_i \frac{\mu_t \partial T}{Pr_t \partial x_i} \tag{A.8}$$

Where Pr_t is the turbulent Prandtl number for energy and g_i is the component of the gravitational vector in the i direction. The standard k-ε model, the default value of $Pr_t$is 0.85. The coefficient of thermal expansion β is defined as:

$$\beta = \frac{-1}{\rho}\left(\frac{\partial \rho}{\partial T}\right)_p \tag{A.9}$$

More information can be found in the ANSYS Fluent 14.0 Theory Guide [50].

(2) Standard *k-ω* Model

The standard and shear-stress transport (SST) models have similar forms with transport equations for k and ω. The major ways in the SST model different from the standard model are as follows:

- The gradual change from the standard *k-ω* model in the inner region of the boundary layer to a high Reynolds number version of the *k-ε* model in the outer part of the boundary layer.
- Modified turbulent viscosity formulation to account for the transport effects of the principal turbulent shear stress.
- The transport equations methods of calculating turbulent viscosity and methods of calculating model constants and other terms are presented separately for each model.

Low Reynolds number modifications have been proposed by Wilcox [53] for the *k-ω*. It is important to note that all *k-ω* models can be integrated through the viscous sub-layer without these terms. The terms were mainly added to reproduce the peak in the turbulence kinetic energy observed in DNS data very close to the wall. In addition, these terms affect the laminar-turbulent transition process. The low Reynolds number terms can produce a delayed onset of the turbulent wall boundary layer and constitute therefore a very simple model for laminar-turbulent transition. In general, the using of the low Reynolds number terms in the *k-ω* models is not introduced. It is advised to use the more sophisticated and more widely calibrated models for laminar-turbulent transition instead.

The standard *k-ω* model in Fluent is based on the Wilcox [53] *k-ω* model which incorporates modifications for low Reynolds number effects, compressibility, and shear flow spreading. One of the weak points of the Wilcox model is the sensitivity of the solutions to values for k and ω outside the shear layer (free stream sensitivity). The new formulation implemented in Fluent has reduced this dependency. It can still have a significant effect on the solution especially for free shear flows.

The standard *k-ω* model is an empirical model based on model transport equations for the turbulence kinetic energy k and the specific dissipation rate ω which can also

be thought of as the ratio of ε to k. The k-ω model has been modified over the years. The production terms have been added to both the k and ω equations which have improved the accuracy of the model for predicting free shear flows.

The turbulence kinetic energy k and the specific dissipation rate ω are obtained from the following transport equations:

$$\frac{\partial}{\partial t}(\rho k) + \frac{\partial}{\partial x_i}(\rho k u_i) = \frac{\partial}{\partial x_j}\left(\Gamma_k \frac{\partial k}{\partial x_j}\right) + G_k - Y_k \tag{A.10}$$

$$\frac{\partial}{\partial t}(\rho \omega) + \frac{\partial}{\partial x_j}(\rho \omega u_j) = \frac{\partial}{\partial x_j}\left(\Gamma_\omega \frac{\partial \omega}{\partial x_j}\right) + G_\omega - Y_\omega \tag{A.11}$$

In these equations, G_k represents the generation of turbulence kinetic energy due to mean velocity gradients. G_ω represent the generation of ω. Γ_k and Γ_ω represent the effective diffusivities of k and ω respectively. Y_k and Y_ω represent the dissipations of k and ω due to turbulence. All of the above terms are calculated as described below.

The effective diffusivities for the k-ω model are given as follows:

$$\Gamma_k = \mu + \frac{\mu_t}{\sigma_k} \tag{A.12}$$

$$\Gamma_k = \mu + \frac{\mu_t}{\sigma_\omega} \tag{A.13}$$

Where σ_k and σ_ω are the turbulent Prandtl numbers for k and ω respectively. The turbulent viscosity, μ_t is computed by combining k and ω as follow:

$$\mu_t = a^* \frac{\rho k}{\omega} \tag{A.14}$$

For Low-Reynolds Number Correction, the coefficient a^* damps the turbulent viscosity causing a low Reynolds number correction. It is given as follows:

$$a^* = a^*_\infty \left(\frac{a^*_0 + Re_t/R_k}{1 + Re_t/R_k}\right) \tag{A.15}$$

Where

$$Re_t = \frac{\rho k}{\mu \omega}$$

$$R_k = 6$$

$$a_0^* = \frac{\beta_i}{3}$$

$$\beta_i = 0.072$$

The high-Reynolds number form of the *k*-ω model, $a^* = a_\infty^* = 1$

The term G_k represents the production of turbulence kinetic energy. From the exact equation for the transport of (k), this term may be defined as follow:

$$G_k = -\rho\overline{\mu_i'\mu_j'}\frac{\partial u_j}{\partial x_i} \quad \text{(A.16)}$$

To evaluate G_k in a manner consistent with the Boussinesq hypothesis is defined as follow:

$$G_k = \mu_t S^2 \quad \text{(A.17)}$$

Where S is the modulus of the mean rate of strain tensor. It defined in the same way as for the *k*-ε model.

The production of ω is given by:

$$G_\omega = a\frac{\omega}{k}G_k \quad \text{(A.18)}$$

The coefficient a is given by

$$a = \frac{a_\infty}{a^*}\left(\frac{a_0 + Re_t/R_\omega}{1+Re_t/R_\omega}\right) \quad \text{(A.19)}$$

The high-Reynolds number form of the *k*-ω model, $a_\infty = a = 1$

The dissipation of k is given as follows:

$$Y_k = \rho\beta^* f_{\beta^*} k\omega \quad \text{(A.20)}$$

Where

$$f_{\beta^*} = \begin{cases} 1\,; & X_k \leq 0 \\ \frac{1+680X_k^2}{1+400X_k^2} & ; \quad X_k > 0 \end{cases} \tag{A.21}$$

Where

$$X_k \equiv \frac{1}{\omega^3}\frac{\partial k}{\partial x_j}\frac{\partial \omega}{\partial x_j} \tag{A.22}$$

And

$$\beta^* = \beta_i^*[1 + \zeta^* F(M_t)] \tag{A.23}$$

$$\beta_i^* = \beta_\infty^* \left[\frac{\frac{4}{15}+(Re_t/R_\beta)^4}{1+(Re_t/R_\beta)^4}\right] \tag{A.24}$$

$$\zeta^* = 1.5$$

$$R_\beta = 8$$

$$\beta_\infty^* = 0.09$$

The dissipation of ω is given as follows:

$$Y_\omega = \rho\beta f_\beta \omega^2 \tag{A.25}$$

Where

$$f_\beta = \frac{1+70X_\omega}{1+80X_\omega} \tag{A.26}$$

$$X_\omega = \left|\frac{Q_{ij}Q_{jk}S_{ki}}{(\beta_\infty^*\omega)^3}\right| \tag{A.27}$$

$$Q_{ij} = \frac{1}{2}\left(\frac{\partial u_i}{\partial x_j} - \frac{\partial u_j}{\partial x_i}\right) \tag{A.28}$$

$$\beta = \beta_i\left[1 - \frac{\beta_i^*}{\beta_i}\zeta^* F(M_t)\right] \tag{A.29}$$

The compressibility function, $F(M_t)$ is given as follows:

$$F(M_t) = \begin{cases} 0\ ;\ M_t \le M_{t0} \\ M_t^2 - M_{t0}^2\ ;\ M_t > M_{t0} \end{cases} \quad \text{(A.30)}$$

Where

$$M_t^2 \equiv \frac{2k}{a^2} \quad \text{(A.31)}$$

$$M_{t0} = 0.25 \quad \text{(A.32)}$$

$$a = \sqrt{\gamma RT} \quad \text{(A.33)}$$

The high Reynolds number form of the *k-ω* model, $\beta_i^* = \beta_\infty^*$. In the incompressible form, $\beta^* = \beta_i^*$

The compressibility correction has been calibrated for a very limited number of free shear flow experiments and it is not recommended for general using.

The model constants are given as below:

$a_\infty^* = 1, a_\infty = 0.52, a_0 = \frac{1}{9}, \beta_\infty^* = 0.09, \beta_i = 0.072, R_\infty = 8,$

$R_k = 6, R_\omega = 2.95, \zeta^* = 1.95, M_{to} = 0.25, \sigma_k = 2, \sigma_\omega = 2$

More information can be found in the ANSYS Fluent 14.0 Theory Guide [50].

Appendix B

A Simple Surface Panel Method "SQCM"

Steady SQCM [14]

SQCM (Source and QCM) uses source distributions [B-1] on the propeller blade surface and discrete vortex distributions arranged on the mean camber surface according to QCM (**Q**uasi-**C**ontinuous vortex lattice Method) [B-2]. These singularities should satisfy the boundary condition that the normal velocity is zero on the propeller blade and the mean camber surfaces.

Consider a *K*-bladed propeller rotating with a constant angular velocity Ω (=$2\pi n$, *n*: number of propeller revolutions) in inviscid, irrotational and incompressible fluid. The space coordinate system *O-XYZ* and the propeller coordinate system *o-xyz* are introduced as shown in Fig. B.1. The cylindrical coordinate system *o-xr*θ is also introduced for convenience. Then the following relation transforms the cylindrical coordinate system *o-xr*θ into the propeller coordinate system *o-xyz*.

$$x = x,\ y = -r\sin\theta,\ z = r\cos\theta \tag{B.1}$$

Where

$$r = \sqrt{y^2 + z^2},\ \theta = \tan^{-1}(-\frac{y}{z})$$

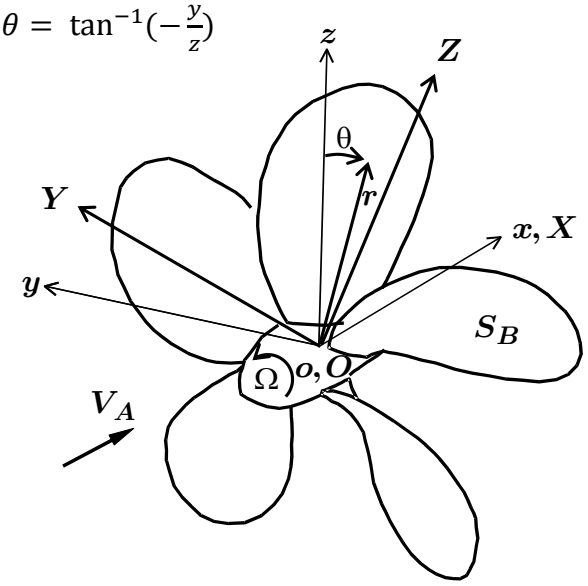

Fig. B.1 Coordinate systems of propeller

Further, the geometry at the propeller blade section is defined. Fig. B.2 shows the section at a radius *r* with pitch *2πa(r)*. The ξ-axis is measured chord-wise from leading edge to trailing edge through the generator line in order to define the intersection point as the origin. The η-axis is measured normal to the ξ-axis from face to back side. Then, the propeller coordinate system *o-xyz* can be expressed as the following equation.

$$\begin{aligned} x &= [\alpha(r)\xi - r\eta]/\sqrt{a(r)^2 + r^2} + x_R(r) \\ y &= -r\sin[\theta_0(r,\xi,\eta) + \theta_R] \\ z &= r\cos[\theta_0(r,\xi,\eta) + \theta_R] \end{aligned} \tag{B.2}$$

Where

$$\theta_0(r,\xi,\eta) = [\xi + a(r)\eta/r]\sqrt{a(r)^2 + r^2}$$

$$\theta_R = \frac{2\pi(k-1)}{K}, k = 1,2,\dots,K$$

$x_R(r)$ is the rake on the blade section at the radius *r*. Also the chord-length *c(r)* is expressed using the leading edge position $\xi_L(r)$ and the trailing edge position $\xi_T(r)$ on the ξ-axis.

$$c(r) = \xi_T(r) - \xi_L(r) \tag{B.3}$$

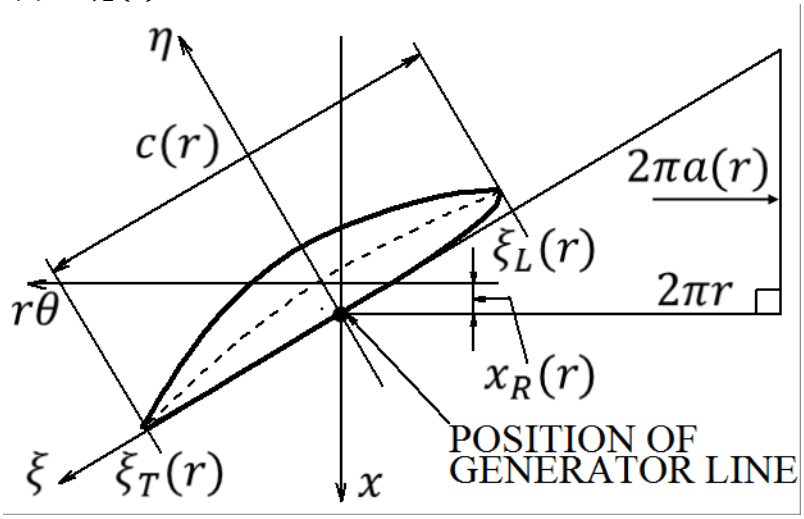

Fig. B.2 Blade section of propeller

The propeller blade S_B is divided into *M* panels in the span-wise direction. The face and back surfaces of the blade section are divided into *N* panels in the chord-wise direction, respectively. Therefore the total number of source panels becomes *(M×2N)×K* and constant source *m* is distributed in each panel. The velocity vector $\vec{V}_m$ due to the source distributions on the blade surface is expressed by using velocity potential Φ_m as

$$\vec{V}_m = \nabla\Phi_m \tag{B.4}$$

Where

$$\Phi_{\boldsymbol{m}} = -\frac{1}{4\pi}\iint_{S_B}\frac{m(x',y',z')}{\sqrt{(x-x')^2+(y-y')^2+(z-z')^2}}dS$$

Next the mean camber surface is divided into *M* segments in the span-wise direction corresponding to the division of the source panels and divided into N_γ in the chordwise direction. Here ξ axis whose origin locates at the leading edge is introduced. And it is extended to the trailing vortex surface along the mean camber surface. The position of the bound vortex $\xi_{\mu v}^{LP}$ and control point $\xi_{\mu v}^{CP}$ on the mean camber surface are expressed by the following equations according to the QCM theory.

$$\begin{aligned}\xi_{\mu v}^{LP} &= \xi_L(r_\mu) + \frac{\xi_T(r_\mu)-\xi_L(r_\mu)}{2}\left(1-\cos\frac{2v-1}{2N_\gamma}\pi\right)\\ \xi_{\mu v}^{CP} &= \xi_L(\bar{r}_\mu) + \frac{\xi_T(\bar{r}_\mu)-\xi_L(\bar{r}_\mu)}{2}\left(1-\cos\frac{v}{N_\gamma}\pi\right)\end{aligned} \tag{B.5}$$

Where

$$\bar{r}_\mu = \frac{1}{2}(r_\mu + r_{\mu+1})$$

μ and *v* are numbers in the span-wise and chord-wise directions. $\xi_L(r_\mu)$ and $\xi_T(r_\mu)$ are the positions of the leading edge (L.E.) and trailing edge (T.E.), respectively. And total *(M×N$_\gamma$)×K* horse shoe vortices are located on the mean camber surface according to Eq. (B.5) as illustrated in Fig. B.3. A horseshoe vortex consists of a bound vortex, two free vortices and two stream-wise trailing vortices. Here stream-wise trailing vortices leave the trailing edge in the direction tangential to the mean camber

surfaces and the pitch of trailing vortices reaches an ultimate value, which is the mean of the geometrical pitch distribution of the propeller blade, within a half revolution. The induced velocity vector due to a horseshoe vortex of unit strength is defined as follows:

$$\vec{v}^{\gamma}_{k\mu v} = \vec{v}^{B}_{k\mu v} + \sum_{v'=v}^{N_\gamma}\left(\vec{v}^{F}_{k\ \mu+1v'} - \vec{v}^{F}_{k\mu v'}\right) + \sum_{l=1}^{N_w}\left(\vec{v}^{T}_{k\ \mu+1l} - \vec{v}^{T}_{k\mu l}\right) \quad \text{(B.6)}$$

Where

$\vec{v}^{B}_{k\mu v}$ = Induced velocity vector due to the bound vortex of unit strength on the mean camber surface.

$\vec{v}^{F}_{k\mu v}$ = Induced velocity vector due to the free vortex of unit strength on the mean camber surface.

$\vec{v}^{T}_{k\mu l}$ = Induced velocity vector due to the stream-wise trailing vortex of unit strength on the wake surface.

The induced velocity vector due to each line segment of vortex is calculated by the Biot-Savart law.

If the strengths of the horseshoe vortex on the mean camber surface is defined, the induced velocity vector due to the vortex model of the QCM theory is given by the following equation.

$$\vec{V}_{\gamma} = \sum_{k=1}^{K}\sum_{\mu=1}^{M}\sum_{v=1}^{N_\gamma}\gamma_{k\mu v}\vec{v}^{\gamma}_{k\mu v}\Delta\xi_{\mu v} \quad \text{(B.7)}$$

Where

$\Delta\xi_{\mu v} = \frac{\pi c(\bar{r}_\mu)}{2N_\gamma}\sin\frac{2v-1}{2N_\gamma}\pi$

$c(\bar{r}_\mu)$ = chord length of μ section

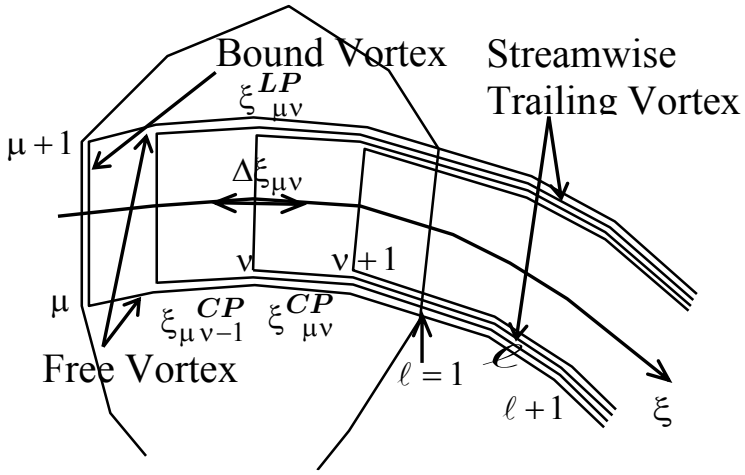

Fig. B.3 Arrangement of vortex systems

In this way, the velocity vector $\vec{V}$ around a propeller in the propeller coordinate system is expressed as

$$\vec{V} = \vec{V}_I + \vec{V}_\gamma + \vec{V}_m \tag{B.8}$$

Where $\vec{V}_I$, $\vec{V}_\gamma$ and $\vec{V}_m$ are inflow, induced velocity vectors due to vortex and source distributions, respectively.

The boundary conditions at the control points on the blade and mean camber surfaces are that there is no flow across the surfaces. Therefore the equation of the boundary condition is given as follows:

$$\vec{V} \cdot \vec{n} = 0 \tag{B.9}$$

Where $\vec{n}$ is the normal vector on the blade and mean camber surface.

The pressure distribution on the propeller blade is calculated by the Bernoulli equation expressed as

$$p - p_0 = -\frac{1}{2}\rho\left(\left|\vec{V}\right|^2 - \left|\vec{V}_I\right|^2\right) \tag{B.10}$$

Where

p_0 = The static pressure in the undisturbed inflow

ρ = The density of the fluid

The pressure of the propeller blade is expressed as the following pressure coefficient C_{pn} in order to compare the calculated results with experimental data.

$$C_{pn} = \frac{p - p_0}{\frac{1}{2}\rho n^2 D^2} \tag{B.11}$$

Where D is the diameter of the propeller

The thrust T and the torque Q of the propeller are calculated by pressure integration. Denoting the x-, y- and z- components of the normal vector on the blade surface by n_x, n_y and n_z respectively, the thrust and the torque are expressed by

$$T = \iint_{S_B} (p - p_0) n_x dS$$

$$Q = \iint_{S_B} (p - p_0)\left(n_y Z - n_z Y\right) dS \tag{B.12}$$

Finally the advanced coefficient J, the thrust and the torque coefficients K_T, K_Q are expressed as follow:

$$J = \frac{V_A}{nD},\ K_T = \frac{T}{\rho n^2 D^4},\ K_Q = \frac{Q}{\rho n^2 D^5} \tag{B.13}$$

References

[B-1] Hess, J.L. and Smith, A.M.O. : "Calculation of Nonlifting Potential Flow about Arbitrary Three Dimensional Bodies", Journal of Ship Research, Vol.8, No.2, pp.22-44, 1964.

[B-2] Lan, C.E. : "A Quasi-Vortex-Lattice Method in Thin Wing Theory", Journal of Aircraft, Vol.11, No.9, pp.518-527, 1974.

List of Tables

List of Figures